

OPTICAL LITHOGRAPHY AND ATOM LOCALIZATION BEYOND THE
DIFFRACTION LIMIT VIA RABI GRADIENT

A Dissertation

by

ZEYANG LIAO

Submitted to the Office of Graduate and Professional Studies of
Texas A&M University
in partial fulfillment of the requirements for the degree of

DOCTOR OF PHILOSOPHY

Chair of Committee, M. Suhail Zubairy
Committee Members, Marlan O. Scully
Alexei Sokolov
Goong Chen
Head of Department, George R. Welch

August 2014

Major Subject: Physics

Copyright 2014 Zeyang Liao

ABSTRACT

The resolution of traditional optical microscope and optical lithography is limited by about half wavelength of the light source, which is well known as the diffraction limit or Abbe limit. The resolution limit is due to the missing of high spatial frequency components in the far-field. One way to achieve high resolution is to move the detector into the near-field region where the evanescent wave can be collected. However, these methods are surface-bound and usually very slow which have limited applications. It has long been an interesting and important question about how to overcome the diffraction limit in the far-field.

For optical lithography, a number of methods have been proposed to overcome the diffraction limit such as multi-photon scanning, quantum entanglement, quantum inspired process (e.g., dopperlon), and quantum dark state. However, these methods either require multi-photon absorber, quantum entanglement, or multi-energy levels, which restrict them from extending to higher resolution in practice. In this thesis, we showed that sub-diffraction-limited resolution can be generated by the coherent Rabi gradient. This method does not require multi-photon absorber or quantum entanglement but just quantum coherence of the medium. Extension from lower resolution to higher resolution is very straightforward where we just need to increase the pulse intensity or pulse duration. We also proposed two atom lithography experiments based on the Rabi gradient. The first one uses Rubidium Rydberg atom and microwave where we showed that sub-micrometer line spacing is possible. The second one uses Chromium atom and optical field where we showed that sub-10nm line spacing is possible while the wavelength of the light is about 400nm.

For optical imaging, a number of methods have also been proposed to achieve

super-resolution such as multi-photon microscope, stimulated-emission-depletion, structured illumination microscopy, centroid-based techniques and metamaterial-based lens. Here, we will show a new method to achieve resolution beyond the diffraction limit which we called it resonance fluorescence microscopy. Resonance fluorescence has been proposed to localize a single atom with resolution beyond the diffraction limit. The separation between two atoms can also be extracted from the resonance fluorescence spectrum. To develop it as microscopy, we need to evaluate the resonance fluorescence spectrum of multiple-atom system. We analytically solved the general feature of the spectrum when the Rabi frequency is much larger than the dipole-dipole interaction and showed how to extract the spatial information of the atoms with resolution far beyond the diffraction limit. This method is entirely based on far-field techniques and it does not require point-by-point scanning.

DEDICATION

To my wife Xiaoqin Chen and my parents, Caimei Lin and Liujin Liao for their love and support.

ACKNOWLEDGEMENTS

First of all, I would like to thank my advisor, Dr. M. Suhail Zubairy, for giving me the opportunity to learn from him. He is erudite, patient, and full of ingenious ideas. Without his careful instruction, I could not finish this thesis. I also want to thank Dr. Marlan O. Scully who led such a great institution and invited me to the Wyoming summer school and PQE, where I learned a lot of physics from him and some other world famous physicists. Thanks also to my colleagues Dr. M. Al-Amri, Dr. Philip R. Hemmer, Dr. Wolfgang P. Schleich, Dr. Thomas Becker, and Fahad S. Alghannam for their wonderful collaborations. Their help was essential in many of my projects. It has been a great pleasure to discuss and learn from them. I also want to thank Dr. Alexei Sokolov from whom I learned a lot about ultrafast and nonlinear optics. I also want to extend my gratitude to the department faculty who taught me physics and the staff who helped me prepare my forms for the defense.

Last but not least, I thank my friends Qingqing Sun, Shuai Yang, Wenchao Ge, Jabir Hakami, Ligang Wang, Xiaodong Zeng, Zhenghong Li, Dawei Wang, Kai Wang, Dong Sun, Dongxia Ma, Zhou chen, Fuxiang Li, Luqi Yuan, Ziyun Di, Zhenhuan Yi, Xia Hua and many more for their help in my life and research. Thanks to my mother and father for their support and encouragement. Finally, I would also thank my wife Xiaoqin Chen for her love and the two best gifts in my life, my son and my daughter who gave me so many laughs during my Ph. D study.

TABLE OF CONTENTS

	Page
ABSTRACT	ii
DEDICATION	iv
ACKNOWLEDGEMENTS	v
TABLE OF CONTENTS	vi
LIST OF FIGURES	viii
1. INTRODUCTION	1
2. DIFFRACTION LIMIT AND PREVIOUS METHODS TO OVERCOME THE DIFFRACTION LIMIT	5
2.1 Optical imaging and optical lithography system	5
2.1.1 Optical imaging and the diffraction limit	5
2.1.2 Optical lithography	6
2.2 Why diffraction limit	6
2.3 Sub-diffraction-limited optical imaging	10
2.3.1 Reducing the effective PSF	10
2.3.2 Recovering the evanescent wave	15
2.4 Optical lithography beyond the diffraction limit	19
2.4.1 Multi-photon lithography	19
2.4.2 Quantum NOON state	21
2.4.3 Quantum inspired technique: dopperlon	23
2.4.4 Coherent population trapping	26
3. OPTICAL LITHOGRAPHY BEYOND THE DIFFRACTION LIMIT VIA SPATIAL RABI OSCILLATIONS	30
3.1 Coherent Rabi oscillations between two atomic levels	30
3.1.1 Rabi oscillations without dissipation	30
3.1.2 Rabi oscillations with dissipation	32
3.2 Optical lithography beyond the diffraction limit via coherent Rabi gradient	33
3.2.1 Achieving the sub-wavelength pattern	34
3.2.2 Arbitrary sub-wavelength patterns in a macroscopic area . . .	38
3.2.3 Potential realizations	43

3.3	Sub-diffraction-limit pattern generation in molecular system via coherent Rabi oscillations	46
3.3.1	Theoretical model	46
3.3.2	Numerical simulation	48
3.3.3	Pulse techniques to improve visibility	53
4.	ATOM LITHOGRAPHY BEYOND THE DIFFRACTION LIMIT VIA COHERENT RABI OSCILLATIONS	58
4.1	Atom lithography	58
4.2	Atom lithography with sub-wavelength line spacing using microwave	60
4.2.1	Basic principle	61
4.2.2	Proposed experimental setup	63
4.2.3	Numerical simulation	66
4.3	Atom lithography with nanometer line spacing using visible light	71
4.3.1	Proposed experimental setup	71
4.3.2	Theory and numerical method	73
4.3.3	Numerical results	79
5.	RESONANCE FLUORESCENCE LOCALIZATION MICROSCOPY BEYOND THE DIFFRACTION LIMIT	85
5.1	Resonance fluorescence	85
5.1.1	Mollow triplet	86
5.2	General feature of the N-atom resonance fluorescence	89
5.3	Three-atoms example	95
5.4	Numerical calculation of the N-atom resonance fluorescence	99
5.5	Extension to larger area and higher dimensions	103
6.	SUMMARY AND OUTLOOK	106
	REFERENCES	109
	APPENDIX A. PULSE AREA THEOREM	120
	APPENDIX B. QUANTUM REGRESSION THEOREM	122

LIST OF FIGURES

FIGURE	Page
2.1 (a) Typical optical imaging system. (b) The PSF of a common oil immersion objective with NA = 1.40, showing the focal spot of 550 nm light in a medium with refractive index n = 1.515. By courtesy of (Huang et al., 2009). Copyright 2009 by the Annual Reviews.	7
2.2 (a) Typical setup for mask-based photolithography. (b) Etching on positive and negative photoresist. Figure reprinted with permission from (Al-amri et al., 2012). Copyright 2012 by the Elsevier.	8
2.3 The origin of the optical diffraction limit can be viewed as the generation of standing wave interference patterns by nearly counter-propagating beams. Figure reprinted with permission from (Hemmer et al., 2012). Copyright 2012 by the IOP Publishing. Reproduced by permission of IOP Publishing. All rights reserved.	9
2.4 (a) Two-photon excitation microscopy. (b) PSF of single-photon excitation and two-photon excitation.	12
2.5 The principle of STED microscopy. (a) The process of stimulated emission. (b) Schematic setup of a STED microscope. The excitation laser and STED laser are combined and focused into the sample through the objective. A phase mask is placed in the light path of the STED laser to create a donut pattern at the objective focal point. (c) A donut-shaped STED laser is applied with the zero point overlapped with the maximum of the excitation laser focus. With saturated depletion, fluorescence from regions except the region around the zero point is suppressed, leading to a decreased size of the effective PSF. By courtesy of (Huang et al., 2009). Copyright 2009 by the Annual Reviews.	13
2.6 Principle of PALM and Storm.	14

2.7	Principle of SIM. (a-c) Moiré fringe. (d) The region within the circle is observable in the far field. (e) The observable region can be extended by frequency mixing. (f) Two dimensional imaging with resolution beyond the diffraction limit can be achieved by repeating the same procedure in different direction. By courtesy of (Gustafsson, 2005). Copyright(2005) National Academy of Science, U.S.A.	16
2.8	(a) Hyperlens made by cylindrical multilayer metamaterial. (b) Wave propagation along the radial direction gradually compresses its tangential wave-vectors, resulting in a magnified image at the outer boundary. The magnified image, once larger than the diffraction limit, will be resolved in the far field.. (c) Experimental demonstration of hyperlens where sub-diffraction-limited pattern can be magnified and detected in the far field. Figure (a) and (b) reprinted by permission from Macmillan Publishers Ltd: [Nature Communications] ([29]), copyright (2012). Figure (c) reprinted with permission from (Liu et al., 2007). Copyright 2007 by the AAAS.	18
2.9	The fringe pattern produced by two-photon excitation of a photoresist, in which the incident rays on opposite sides of the lens are separated into distinct frequency grouping. Figure reprinted with permission from (Yablonovitch and Vrijen, 1999). Copyright 1999 by SPIE.	20
2.10	Interferometric lithography setup where two photon beams hitting a beam splitter at ports A and B, and then get reflected by two mirrors. The two photon beams get interfere on the substrate. Figure reprinted with permission from (Boto et al., 2000). Copyright 2000 by American Physical Society.	22
2.11	(a) Subwavelength interference with classical light. Two counter-propagating plane waves consisting of signal frequencies ν_{\pm} interfere on a photosensitive substrate. The drive fields ω_{\pm} assist a directional resonance for pairs of signal photons. (b) Left: The scheme of interferometric lithography. Two bunches of signal fields counterpropagate ($\theta = \pi/2$) and the drive field incidents normally. Right: The level structure of the substrate atom. Either bunch of fields together with the drive field satisfies the multiphoton resonance. $\Delta_{n\pm}$ is the detuning of intermediate level c_n . Figure reprinted with permission from (Hemmer et al., 2006 and Sun et al., 2007). Copyright 2006, 2007 by the American Physical Society.	25

2.12 Considered level schemes of the substrate. The ground states $ b_n\rangle$ and $ b_{n+1}\rangle$ are resonantly coupled to the excited state $ a_n\rangle$ via Rabi frequencies Ω_{R_n} and Ω_{S_n} , respectively. Each excited state $ a_n\rangle$ decays to the ground states $ b_n\rangle$ and $ b_{n+1}\rangle$ by spontaneous emission. (a) Single Λ system. In (b), a sequence of two Λ systems is displayed. (c) General level scheme with N excited and $N + 1$ ground states as a sequence of N Λ -type systems. Figure reprinted with permission from (Kiffner et al., 2008). Copyright 2008 by the American Physical Society.	28
3.1 Rabi oscillations for (a) square pulse: Blue dashed line is the pulse shape, red solid line is the probability in the excited state in the resonant case, while the black dotted line is the probability in the excited state when $\Delta = \Omega_R$. (b) Gaussian pulse: Blue dashed line is the pulse shape, red solid line is the probability in the excited state in the resonant case.	31
3.2 Rabi oscillations with decay (a) and with dephasing (b).	33
3.3 Comparison between the traditional optical lithography (a) and our lithography scheme (b).	33
3.4 Subwavelength patterns generated by fields of different $\Omega_R T$. (a) $\Omega_R T = \pi$; (b) $\Omega_R T = 2\pi$; (c) $\Omega_R T = 3\pi$; (d) $\Omega_R T = 4\pi$. The solid line is when the decay is not included whereas the blue dashed line shows the results with $\gamma = \omega_{ab}/1000$.	35
3.5 (a) The Gaussian pulse. The red dash line is the amplitude profile and the thick dark line is the intensity profile; (b) The pattern produced by the Gaussian pulse when $\sqrt{\frac{\pi}{2\ln 2}}\Omega_0 t_{FWHM} = 2\pi$; (c) The pattern produced by the Gaussian pulse when $\sqrt{\frac{\pi}{2\ln 2}}\Omega_0 t_{FWHM} = 4\pi$. The solid line is the result without the decoherence while the green dashed line shows the results with $t_{FWHM} = \tau/2$.	39
3.6 A proposed scheme to print a sine pattern in an arbitrary large region.	41
3.7 A 2D pattern "TAMU-KACST" printed within one wavelength using the present method. Parameters are $M = N = 15$, $\theta = 80^\circ$.	44
3.8 The schematics for the state energy diagram for molecular organic photochemistry.	44

3.9	Typical energy potential surface of a molecule. The first pulse is used to inducing coherent Rabi oscillations between two energy potential surfaces, while the second pulse is used to dissociate the molecules in the excited state.	46
3.10	Dynamics of the population in the excited state as a function of time when the molecule is excited by a ultrashort pulse. The solid line is the result when $\Omega_0 = 20, t_p = 1$. The dotted line is the result when $\Omega_0 = 50, t_p = 0.4$. (a) $\alpha = 0$; (b) $\alpha = 1$; (c) $\alpha = 5$	49
3.11	Subdiffraction-limited pattern generation when the molecule is excited by a diffraction-limited beam. The dashed line is the intensity profile of the diffraction-limited excitation beam. The solid line is the pattern generated by the pulse with $\Omega_0 = 20, t_p = 1$. The dotted line is the result when $\Omega_0 = 50, t_p = 0.4$. (a) $\alpha = 0$; (b) $\alpha = 1$; (c) $\alpha = 5$	52
3.12	(a) Electric field envelopes for one, two, and four-pulse train. (b) Wave packet dynamics excited by one, two, and four-pulse train. (c) Subdiffraction-limited pattern generated by one, two, and four-pulse train excitation. The solid line is for one pulse case with $\Omega_0 = 50$ and $t_p = 0.4$. The dotted line is for two-pulse train with $\Omega_0 = 50, t'_p = 0.2$, and $\tau = 0.4$. The dashed line is for four-pulse train with $\Omega_0 = 50, t'_p = 0.1, \tau_1 = 0.2, \tau_2 = 0.4$, and $\tau_3 = 0.6$	54
3.13	(a) Example of a linearly chirped pulse. (b) Dynamics of the population in the excited state as a function of time when the molecule is excited by an unchirped and chirped pulse. (b) Subdiffraction-limited pattern generated by an unchirped and chirped pulse. The solid line is the result for unchirped pulse while the dotted line is the result for chirped pulse. Parameters: $\alpha = 5, \Omega_0 = 50, t_p = 0.4$	56
4.1	(a) Typical setup of atom lithography. (b) Optical dipole potentials for different laser intensity where $\eta = I_{max}/I_0$. (c) A pattern written by the atom lithography. Figure (a) reprinted with permission from (te Sligte et al., 20033). Copyright 20033 by Elsevier. Figure (c) reprinted with permission from (McClelland et al., 1993). Copyright 1993 by AAAS.	59
4.2	(a) Proposed experimental setup for the sub-wavelength atom lithography using position-dependent Rabi oscillations of Rydberg atoms (unit for the dimension is cm). P1 is photoresist used for neutral atom lithography while P2 is the photoresist used for ionized atom lithography. (b) Energy diagram of the Rb-85 atom.	63

4.3	Simulation of neutral atom lithography with sub-wavelength resolution due to a position-dependent Rabi frequency represented by the spatial distribution of the $61D_{3/2}$ ($ b\rangle$) state for different Rabi frequencies Ω_0 . (a) $\Omega_0 = 2\pi \times 500\text{KHz}$; (b) $\Omega_0 = 2\pi \times 1.0\text{MHz}$; (c) $\Omega_0 = 2\pi \times 5\text{MHz}$; (d) $\Omega(x) = 2\pi \times 10\text{MHz}$. The transverse velocity uncertainty is $0.1m/s$ for (a) and (b), while is $0.01m/s$ for (c) and (d). The longitudinal uncertainty is fixed to be $1.48m/s$.	68
4.4	Simulation of ionized atom lithography with sub-wavelength resolution due to a position-dependent Rabi frequency represented by the spatial distribution of the $63P_{3/2}$ ($ a\rangle$) state for different Rabi frequencies Ω_0 . (a) $\Omega_0 = 2\pi \times 500\text{KHz}$; (b) $\Omega_0 = 2\pi \times 1.0\text{MHz}$; (c) $\Omega_0 = 2\pi \times 5\text{MHz}$; (d) $\Omega(x) = 2\pi \times 10\text{MHz}$. The transverse velocity uncertainty is $0.1m/s$ for (a) and (b), while is $0.01m/s$ for (c) and (d). The longitudinal uncertainty is fixed to be $1.48cm/s$.	69
4.5	Proposed experimental setup for the sub-wavelength atom lithography using position-dependent Rabi oscillations. BS: beam splitter; AOM: acoustic optical modulator; LP: linear polarizer; $\lambda/4$: quarter wave plate.	73
4.6	a) Sub-wavelength structure in the Raman-Nath approximation. Dashed line is the normalized electric field strength of the standing wave, and the solid curve is the probability of the atom in the excited state. b) Optical Stern-Gerlach effect. The $ +\rangle$ state and $ -\rangle$ state see different optical potentials and an incoming atomic wavepacket splits into two wavepackets.	74
4.7	Spatial distribution of the atom (dotted line) and the atom in the exited state (solid line) after the standing wave for different peak rabi frequencies and different transverse velocity collimation. Peak Rabi frequencies: (a-c) $\Omega_0 = 0.4\text{GHz}$ while $\Omega_0 = 2\text{GHz}$ for (d-f). Transverse velocity collimation: (a,d) $\Delta v_\perp = 100v_r$; (b,e) $\Delta v_\perp = 10v_r$; (c,f) $\Delta v_\perp = v_r$.	81
4.8	Spatial distribution of the atom (a,c) and the atom in the exited state (b,d). The brighter the higher probability. Peak Rabi frequencies: $\Omega_0 = 2\text{GHz}$.	84
5.1	(a) Pictorial presentation of resonant light scattering. (b) Mollow triplet shown in resonance fluorescence spectrum.	86
5.2	Scheme for resonance fluorescence microscopy. x_i is the position of the i th atom.	90

5.3	Principle of atom localization from resonance fluorescence spectrum.	95
5.4	Dressed state picture for three interacting atoms. $ \pm\pm\pm n\rangle = (bn_1\rangle \pm an_1-1\rangle) \otimes (bn_2\rangle \pm an_2-1\rangle) \otimes (bn_3\rangle \pm an_3-1\rangle)$ where $n_1+n_2+n_3 = n$.	96
5.5	Example for three-atom resonance fluorescence microscopy.	98
5.6	Numerical examples of three-atom resonance fluorescence spectrum. (a) $x_1 = 0.3\lambda, x_2 = 0.5\lambda, x_3 = 0.7\lambda, \Omega(x) = 100\Gamma x/\lambda$. (b) $x_1 = 0.45\lambda, x_2 = 0.5\lambda, x_3 = 0.6\lambda, \Omega(x) = 100\Gamma x/\lambda$. (c-d) Same as (b) but $\Omega(x) = 2000\Gamma x/\lambda$. (e) Spectrum shifts when Rabi frequency changes (Red: $\Omega(x) = 1500\Gamma x/\lambda$; Blue: $\Omega(x) = 2000\Gamma x/\lambda$). (f) The result when $\theta = \cos^{-1}(1/\sqrt{3})$ and $\Omega(x) = 200\Gamma x/\lambda$	101
5.7	(a) Schematic setup for imaging atoms in an extended region based on our resonance fluorescence localization microscopy. (b) 2D resonance fluorescence localization microscopy.	104

1. INTRODUCTION

Optical microscope is one of the most important inventions in the development of the biology. It is widely used to study the micro-structures of the biological systems. The advantages of optical microscope are its highly parallel and low damaging. However, according to the Abbe's diffraction limit [1, 2], the resolution of optical microscope is limited by about half wavelength of the light source. For example, if the light source has a wavelength of about 500nm, the lateral resolution is about 200nm. The features below 200nm can not be resolved.

In the past few decades, a number of schemes have been developed to improve the resolution of the microscopy. To get a better resolution, people have to switch to shorter wavelength (e.g., electron microscope and X-ray lithography [3, 4, 5] which is usually invasive to the system. While confocal microscopy introduced optical sectioning and can get a better resolution than the conventional ones, it did not overcome the diffraction limit [6]. Near-field scanning microscopy can obtain optical imaging with subdiffraction resolution [7, 8, 9, 10, 11]. These techniques are however surface bound and are thus limited in terms of applications. Two-photon fluorescence microscopy was first developed to achieve a higher resolution than classical one-photon fluorescence microscopy [12, 13, 14, 15, 16]. Stimulated-emission-depletion fluorescence microscopy (STEP) was then developed by Stefan W. Hell and Jan Wichmann in 1994 [14] and the related concepts such as ground-state depletion (GSD) are then developed [17, 18]. A number of experiments have also been carried out [19, 20, 21, 22]. Some other techniques such as Spatially Structured Illumination Microscopy (SSIM) [23, 24], Photoactivated Localization Microscopy (PALM) [25], and Stochastic Optical Reconstruction Microscopy (STORM) [26] are also invented

to achieve super resolution. Metamaterial-based lens can collect the high spatial frequency information and obtain a super-resolution image in the far field [27, 28, 29]. Coherent population trapping or Dark state has also been proposed to achieve super-resolution [30, 31, 32, 33]. Resonance fluorescence has been proposed to localize a single atom with resolution far-beyond the diffraction limit [34], and it has been proposed to measure the separation between two atoms [35, 36, 37, 38]. In 2012, we calculated the resonance fluorescence spectrum of multiple atoms system and showed that the spatial information of the atoms can be extracted from the spectrum with resolution far beyond the diffraction limit. This method can become a new type of super-resolution microscopy which is entirely based on far-field and does not require point-by-point scanning [39].

The diffraction limit not only affects the optical microscope, but also plays an important role in the optical lithography system. Optical lithography has been one of the most important driving forces for the development of computer chips [40, 41, 42, 43, 44]. The performance of the computer chips has increased dramatically over the past few decades, and meanwhile the size of the integrated circuits reduced roughly following the famous Moore's law. In fact, almost any electronic equipment that uses processors or memory to work, such as cellular phone, digital photo cameras or automobiles, is the beneficiary of the optical lithography.

About 20 years ago, the smallest features printed with optical lithography were twice the wavelength used to print them. Today the industry is pressing toward the need for much smaller resolution. However, there is a diffraction limit that restricts the smallest patterns we can print to about half of the wavelength of light source [1, 2, 45]. Therefore, to make the chip smaller, we should switch to shorter working wavelength [46]. Nowadays, the working laser can operate in deep ultra-violet (DUV 190-250nm) [47, 48, 49]. Using the immersion lithography technology, the half-pitch

nodes currently obtained with 193nm light are 45nm and 32nm [50]. New tricks such as double exposure lithography (DEL) or double patterning lithography (DPL) are possible to extend the resolution by a factor of 2 [51]. However, these technologies are not possible without the development of new material with nonlinear response to the exposure dose. While we switch to shorter wavelength, two major problem arise [52]: First, the traditional lens and the air absorb the light significantly. We need to invent new materials for the lens which is hard to come, and the system should work in a vacuum system that can be very expensive. Second, the bandgap of SiO_2 is about 9ev. When the wavelength of the light is close to or smaller than 138nm, it will cause adverse charging in the SiO_2 layer and destroy the substrate. This motivates us to go beyond the Rayleigh limit and study ways to overcome the diffraction limit.

In the past two decades, a number of schemes have been proposed to overcome the diffraction limit in optical lithography. Two-photon excitation in laser scanning photolithography can allow exposure of patterns not possible with conventional one-photon direct writing [53]. Unfortunately, this scheme is based on point-by-point scanning which has limited applications. In fact the ordinary two-photon absorption can only achieve a sharper peak but not improve the spatial resolution in terms of line spacing. In 1999, E. Yablonovitch and R. B. Vrijen illustrated how to suppress the normal resolution term and get a supper resolution image based on two-photon absorption [54]. The visibility of this scheme is reduced due to a constant background. Quantum NOON state is then shown to be able to eliminate the normal resolution term without a constant background [55]. After that several quantum inspired techniques are shown to achieve super-resolution without quantum entanglement [56, 57, 58]. In 2008, M. Kiffner *et al* came out with a novel idea that subwavelength resolution can be achieved by preparing the system in a position de-

pendent trapping state [32]. In 2010, we proposed that coherent Rabi gradient can lead to sub-wavelength resolution [59, 60], which does not require quantum entanglement or multi-photon absorber but just quantum coherence of the medium. We also proposed two atom lithography experiments based on Rabi gradient. One is using Rubidium Rydberg atoms and microwave where we numerically showed that micrometer resolution is possible [61]. The other is using Chromium atoms and optical field and we showed that sub-10nm may be achieved without significant optical Stern-Gerlach effect [62].

This thesis is organized as follows. In Chapter 2, we begin by introducing the diffraction limit in an optical system and briefly introduce some previous methods to overcome the diffraction limit in both optical imaging and optical lithography. In Chapter 3, we explain our method to overcome the diffraction limit via coherent Rabi oscillations. In chapter 4, we illustrate two atom lithography schemes to achieve sub-diffraction-limited resolution. One is using Rydberg Rubidium atom and the microwave. The other is using Chromium atom and the optical field. In Chapter 5, we calculated the resonance fluorescent spectrum of multiple atoms and showed that spatial information of the atoms can be extracted from the resonance fluorescence spectrum with resolution well below the diffraction limit. Finally we present the summary and the outlook.

2. DIFFRACTION LIMIT AND PREVIOUS METHODS TO OVERCOME THE DIFFRACTION LIMIT

Optical imaging system is widely used in both the microscopy and the modern optical lithography. However, there is a resolution limit for traditional optical imaging system, which is well known as diffraction limit. In this chapter, I will first briefly introduce the traditional optical imaging and optical lithography system. Then I will explain why there is a resolution limit. In the last two sections I will briefly introduce some previous methods to overcome the diffraction limit in the optical imaging and the optical lithography system.

2.1 Optical imaging and optical lithography system

2.1.1 *Optical imaging and the diffraction limit*

A typical optical imaging system is shown in Fig. 2.1(a) [63]. The light source is focused onto the sample by a condenser lens. The scattering light or fluorescence from the sample is collected by an objective lens and observed either by the eye or a detector in the far field. This kind of microscope has been widely used in many areas such as the biological or medical imaging.

According to the Rayleigh criterion, the minimum feature size that an optical imaging system can resolve is approximately given by [1, 2, 45]:

$$\Delta r = \frac{\lambda}{2n \sin \theta} \quad (2.1)$$

where λ is the wavelength of the illumination light and $n \sin \theta$ is the numerical aperture of the lens as seen from the sample (n is the refractive index of the medium between the sample and the objective lens, θ is the half-angle of the maximum cone

of light that can enter the objective lens). Use oil as a medium with refractive index about 1.5, the numerical aperture can be about 1.4. The focal spot of 550nm light is shown in Fig. 2.1(b). We can see that the image is not a perfect point but blurred into a finite-sized spot [64]. The lateral resolution is about 220nm while the vertical resolution is about 520nm. The intensity distribution of the image of a point object is called the point spread function (PSF). The size of PSF determines the resolution of the microscope. Two points closer than the full width at half-maximum (FWHM) of PSF is difficult to resolve because their images overlap substantially.

2.1.2 Optical lithography

Mask-based photolithography is commonly used to print the circuit image onto the substrate in the industry nowadays [65, 66]. The typical setup is shown in Fig. 2.2(a). The light projects the image of the pattern on the mask onto the photoresist. Some places are bright while others are dark in the photoresist. The photoresist changes its solubility at the place where it is shined by the light. There are two types of photoresist: positive and negative (see Fig. 2.2(b)). In a positive-tone photoresist, areas of the material that are exposed to light are removed after development. While in a negative-tone photoresist, the areas exposed by the light remain behind. After development, the pattern is printed onto the photoresist. The SiO₂ layer is then etched at the place without the protection of the photoresist. The smallest feature we can print is also bounded by the diffraction limit.

2.2 Why diffraction limit

The diffraction limit can be explained as the generation of standing wave interference patterns by the nearly counter-propagating beams (Fig. 2.3) [67]. The lens can be divided into many sub-apertures and each sub-aperture pair of the lens can produce a standing wave pattern with different spatial frequencies. The interference

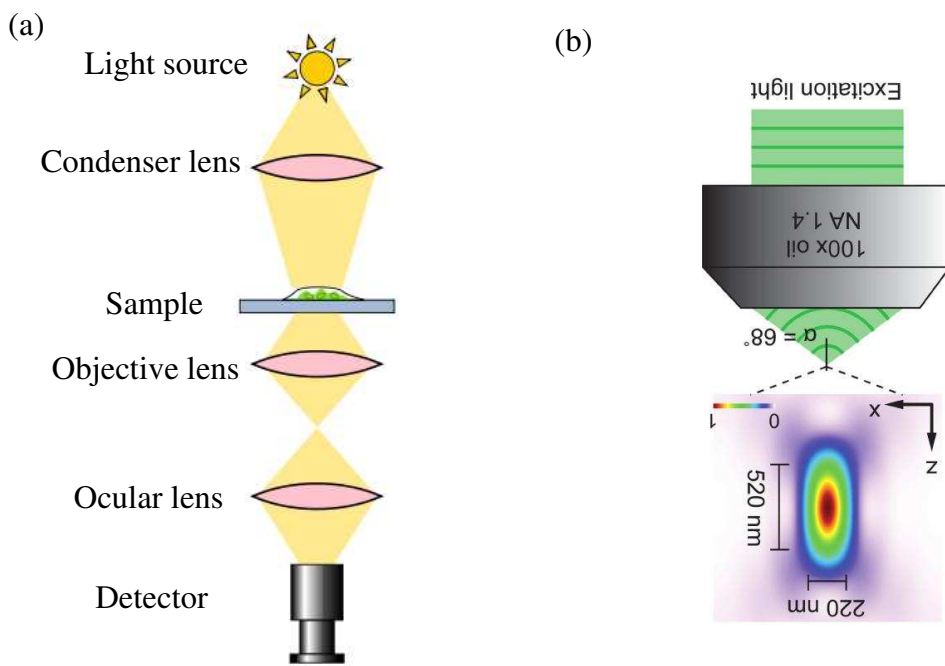


Figure 2.1: (a) Typical optical imaging system. (b) The PSF of a common oil immersion objective with $\text{NA} = 1.40$, showing the focal spot of 550 nm light in a medium with refractive index $n = 1.515$. By courtesy of (Huang et al., 2009). Copyright 2009 by the Annual Reviews.

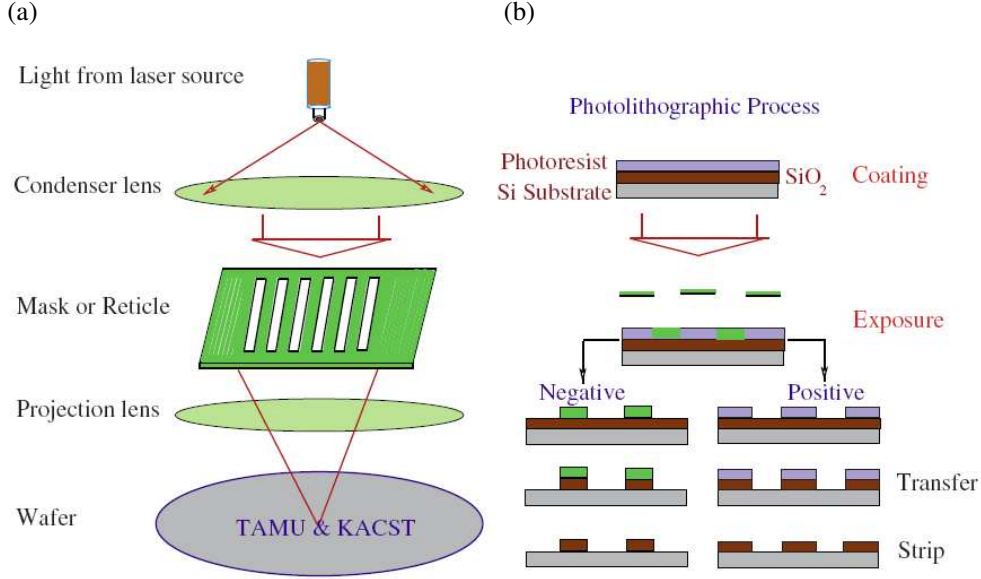


Figure 2.2: (a) Typical setup for mask-based photolithography. (b) Etching on positive and negative photoresist. Figure reprinted with permission from (Al-amri et al., 2012). Copyright 2012 by the Elsevier.

pattern between these standing wave is the image. The image of a point source is shown in Fig. 2.3(e) which is a Airy disk. The size of the Airy disk is determined by the largest spatial frequency component which is the standing wave comes from the outermost sub-aperture pair. The period of that standing wave intensity pattern is $\lambda_0/2n \sin \theta$ which gives the diffraction limit.

The diffraction limit can also be explained by loss of the high spatial frequencies which is the evanescent wave [68, 65, 69]. According to the Fourier optics, the electric field on the imaging plane is the summation of varies frequencies components emitted from the object plane:

$$\varepsilon(x, y, z) = \sum_{\sigma} \int_{k_x} \int_{k_y} \varepsilon_{\sigma}(k_x, k_y) e^{ik_x x + ik_y y + ik_z z} dk_x dk_y \quad (2.2)$$

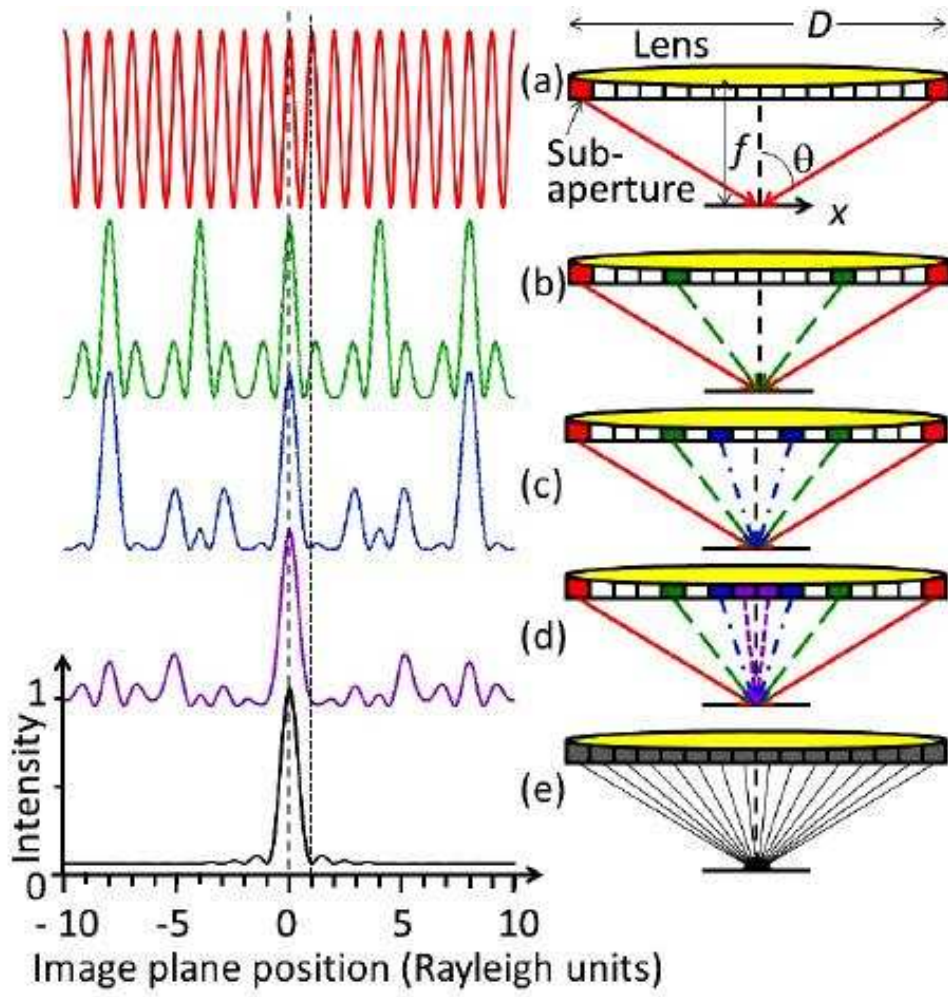


Figure 2.3: The origin of the optical diffraction limit can be viewed as the generation of standing wave interference patterns by nearly counter-propagating beams. Figure reprinted with permission from (Hemmer et al., 2012). Copyright 2012 by the IOP Publishing. Reproduced by permission of IOP Publishing. All rights reserved.

where σ is the polarization, z is the propagation direction and $k_x^2 + k_y^2 + k_z^2 = n^2\omega^2/c^2$ (n is the refractive index of the medium, ω is the angular frequency of the light and c is the speed of the light). For the high spatial frequency such that $k_x^2 + k_y^2 > n^2\omega^2/c^2$, k_z is pure imaginary which means that this component decays in the propagation direction. This corresponds to the evanescent wave and such waves can not reach the imaging plane in the far field. The highest spatial frequency that can reach the imaging plane is $k_{||} = \sqrt{k_x^2 + k_y^2} = n\omega/c$, which corresponds to a resolution of $2\pi/k_{||} = 2\pi c/n\omega$ [70]. This corresponds to the maximal resolution for the field to be equal to λ/n . The corresponding maximal resolution for the intensity is therefore equal to $\lambda/2n$. Considering the aperture of the lens, the maximal transverse wavevector that can reach the image plane is $k_{||} = k \sin \theta = n\omega \sin \theta/c$, and thus the maximum resolution is $\lambda/2n \sin \theta$ which is the diffraction limit.

In the following two sections, I will introduce some proposed methods to overcome the diffraction limit in the optical imaging system and the optical lithography system.

2.3 Sub-diffraction-limited optical imaging

In this section, I will briefly introduce two classes of methods to overcome the diffraction limit in optical microscopy. The first class is trying to reduce the effective PSF, while the other class is trying to recover the high spatial frequency evanescent wave in the far field.

2.3.1 Reducing the effective PSF

The light intensity distribution $I(x, y)$ in the image plane can be mathematically described as the product of the light intensity distribution $O(u, v)$ in the object plane and the PSF [71]:

$$I(x, y) = \int \int O(u, v) PSF(u - x/M, v - y/M) dudv \quad (2.3)$$

where M is the magnification. In diffraction-limited lens system, PSF is an Airy disk function which can be well approximated by a Gaussian function. If we can somehow reduce the effective PSF, we can in principle get an image with better resolution than the diffraction-limited image. In the following, I will briefly introduce several popular methods to reduce the effective PSF.

2.3.1.1 Two-photon and multi-photon microscopy

The first method to reduce the effective PSF is using multi-photon excitation, e.g., two-photon excitation (Fig. 2.4(a)). The concept of two-photon excitation was first described by Goeppert-Mayer in her doctoral dissertation [72], and first observed in cesium vapor using laser excitation by Abella [73]. Two-photon excitation is found to be able to improve the resolution in the fluorescence microscopy [12, 74] and increase the data capacity of the storage [16]. Such a process depends quadratically on the photon intensity I of the incident beam [72, 75], i.e., the excitation rate, or the number of photons being absorbed per unit time, $W = \sigma I^2$, where σ is the absorption cross section, typically of the order of $10^{-58} m^4 s/photon$. The quadratic dependence of the intensity can reduce the effective PSF (Fig. 2.4(b)) and thus improves the resolution.

However, the wavelength used for two-photon excitation is usually longer than one-photon excitation. The resolution of two-photon microscope does not improve a lot comparing with single-photon confocal microscope. One advantage of two-photon microscopy is that it can achieve good vertical resolution without pinhole and it can be used as optical sectioning as confocal microscope. The other advantage is that two-photon excitation can penetrate deeper than single-photon excitation [15].

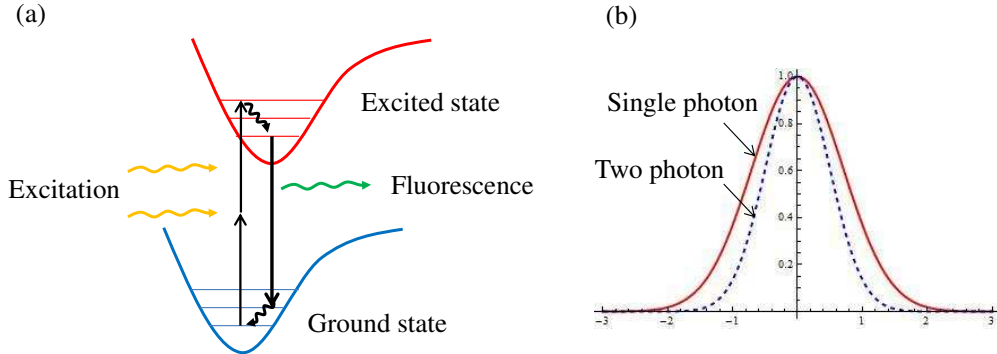


Figure 2.4: (a) Two-photon excitation microscopy. (b) PSF of single-photon excitation and two-photon excitation.

2.3.1.2 STED and related techniques

Stimulated emission depletion (STED) is proposed by Hell et. al to overcome the diffraction limit [14]. The STED method is shown in Fig. 2.5[14, 64]. All the molecules are first pumped into the excited state. Another laser beam with donut shape is then applied to deplete all the molecule from the excited state to the ground state except the molecules around the center where the laser intensity is very weak. In this way, we can largely reduce the effective PSF (Fig. 2.5(c)) and achieve super-resolution.

STED has been experimentally demonstrated to achieve super-resolution [21, 19, 22]. The resolution is given by [17]

$$\Delta r \approx \frac{\lambda}{2n \sin \theta \sqrt{1 + I_{max}/I_s}} \quad (2.4)$$

where I_{max} is the maximum intensity of the donut beam and I_s is the saturation intensity. We can see that the resolution is enhanced by a factor of $\sqrt{1 + I_{max}/I_s}$. If we increase the intensity of the depletion beam, we can get resolution much better

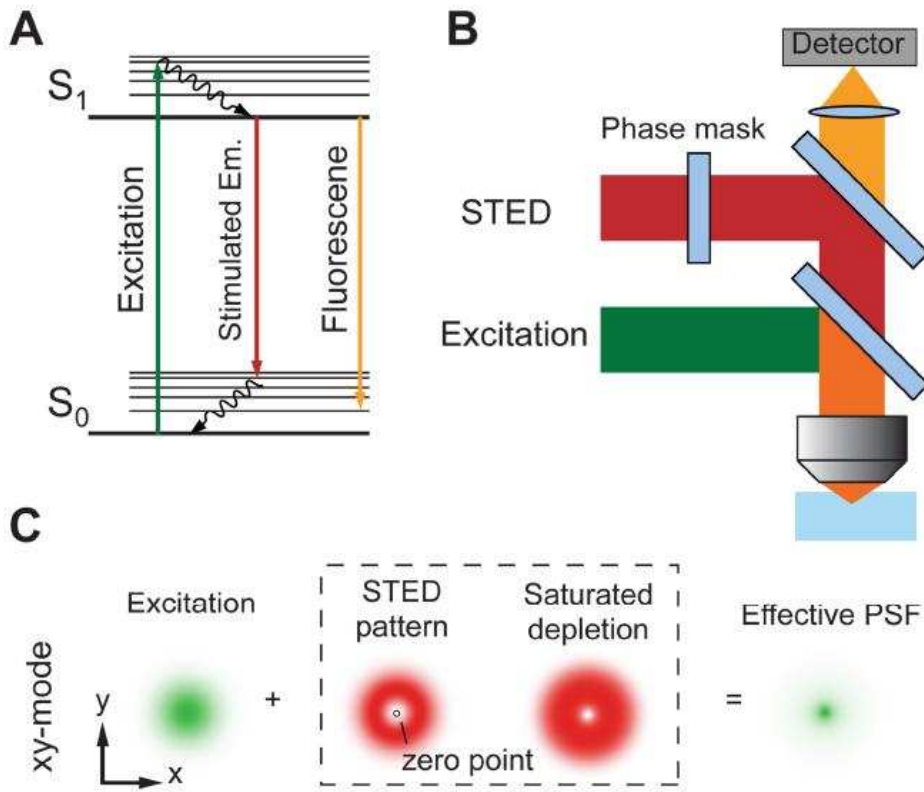


Figure 2.5: The principle of STED microscopy. (a) The process of stimulated emission. (b) Schematic setup of a STED microscope. The excitation laser and STED laser are combined and focused into the sample through the objective. A phase mask is placed in the light path of the STED laser to create a donut pattern at the objective focal point. (c) A donut-shaped STED laser is applied with the zero point overlapped with the maximum of the excitation laser focus. With saturated depletion, fluorescence from regions except the region around the zero point is suppressed, leading to a decreased size of the effective PSF. By courtesy of (Huang et al., 2009). Copyright 2009 by the Annual Reviews.

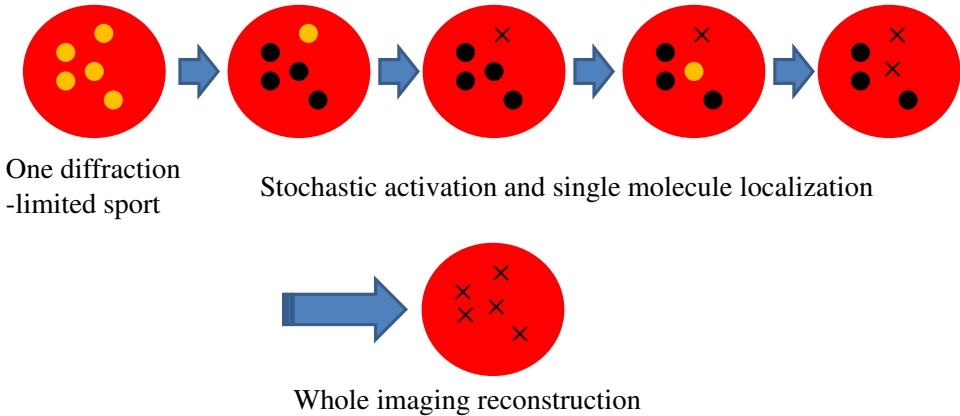


Figure 2.6: Principle of PALM and STORM.

than the diffraction limit. However, this method is based on point-by-point scanning which is very slow.

2.3.1.3 Centroid-based techniques

The center of the PSF is the most probable position of the molecule and the precision is given by [64]

$$\Delta r \approx \frac{\Delta}{\sqrt{N}} \quad (2.5)$$

where Δ is the full width at half-maximum of the PSF and N is the number of photons detected. The larger the number of photon we detect, the higher the precision of the localization. However, if there are more than one molecule within a diffraction-limited spot, their images merger together and we can not identify them individually.

Several methods have been proposed to solve this problem such as PALM [25] and STORM [26]. These methods separate the molecules within one diffraction-limited spot in the time domain. They proposed to use some kind of photoactivatable or photoswitchable molecules to mark the target molecules. PALM and STORM share

very similar principle and I will briefly explain how PALM achieves super-resolution (Fig. 2.6) [25]. Initially all the molecules are in the inactive state. First, a weak laser with special frequency is applied to randomly activate a subset of molecules into the active state. Since the excitation laser is sparse and weak, the probability that more than one molecule in a diffraction-limited spot are activated is very small. We can safely assume that only one molecule within one diffraction-limited spot is in the active state. Then another color of laser is applied to probe the molecules in the active state through the fluorescence of these molecules. Since we have only one molecule in one diffraction-limited spot, we can localize the position of the molecule by fitting the center of the PSF and its precision depends on the number of photon we detect. Usually, hundreds of photons are detected because the resolution increases very slow when N is large. After localizing the activated molecules, we need to bleach the molecules by continuously shine the excitation laser. Repeating the above procedures and summing the images up we can obtain a whole super-resolution image.

This kind of stochastic method does not require point-by-point scanning and the intensity required is also not too strong. However, it does not speed up too much comparing with point-by-point scanning because hundreds of photons needs to be detected to determine the positions of the molecules and bleaching the molecule also takes some times.

2.3.2 Recovering the evanescent wave

Another class of method to achieve super-resolution is to recover the evanescent wave in the far field. In the following, I will briefly introduce two ways to rescue the evanescent wave. One is called structured illumination microscopy (SIM) [23], the other is called metamaterial-based lens [27, 28, 29].

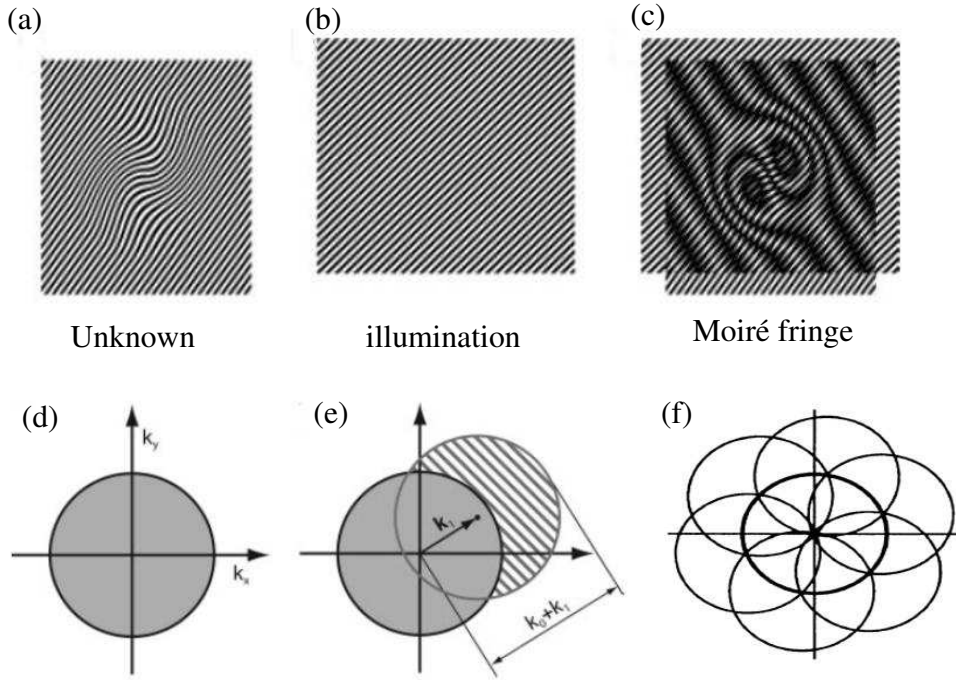


Figure 2.7: Principle of SIM. (a-c) Moiré fringe. (d) The region within the circle is observable in the far field. (e) The observable region can be extended by frequency mixing. (f) Two dimensional imaging with resolution beyond the diffraction limit can be achieved by repeating the same procedure in different direction. By courtesy of (Gustafsson, 2005). Copyright(2005) National Academy of Science, U.S.A.

2.3.2.1 Structured illumination microscopy

The idea of SIM comes from the well-known Moiré fringe (Fig. 2.7 (a-c)). The Moiré fringe are produced by frequency mixing whenever two signals are multiplied. The coarser structure in the Moiré fringe which consists of the information of high spatial frequency component can be detected in the far field. For example, Fig. 2.7(a) is the unknown structure we would like to image. We can illuminate a laser standing wave with known spatial frequency to detect the structure. Due to the frequency mixing, the observable spatial frequency in the far-field can be extended

to $k_0 + k_i$ where k_0 is the largest wave vector observable in the diffraction-limited system and k_i is the wave vector corresponding to the illumination pattern (Fig. 2.7(d,e)). In principle, k_i can reach k_0 in the linear regime and the observable region in the momentum space can be expanded by a factor of 2. In the real space, the resolution can be half of the resolution limit. To reconstruct full two dimensional pattern, we need to repeat this procedure from different directions Fig. 2.7(f).

To achieve better resolution, higher order harmonic frequencies should be excited. One way to excite higher order harmonic frequency is to increase the illumination intensity and saturate the excitation. When the excitation is saturated, the absorption rate nonlinearly depends on the illumination intensity and the observable region in the momentum space can be extended beyond a factor of 2. This method is called saturated structured illumination microscopy (SSIM) [24].

The advantage of this method is that it is essentially a parallel method and it does not require point-by-point scanning. However, it also requires a larger number of measurements to determine a two dimensional pattern and the intensity required for SSIM is very high which is not suitable for living cells.

2.3.2.2 Matematerial-based lens

From the maxwell equations, we can see that if both the permittivity and the permeability are negative, the refractive index of the material can be negative which is called negative refractive material or matematerial [27]. For negative refractive material, strange phenomena can happen. For example, the refracted beam is at the same side of the normal plane as the incident beam and the evanescent wave can propagate without decay in the matematerial. Due to the first property, a flat slab of matematerial can become a lens which is called superlens [27, 70]. Comparing with the traditional lens, the flat matematerial lens have not spherical aberration.

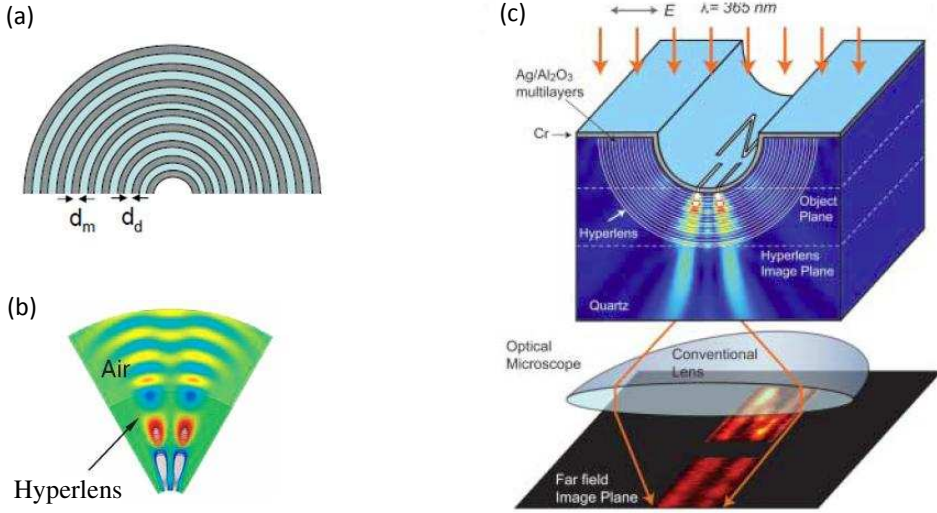


Figure 2.8: (a) Hyperlens made by cylindrical multilayer metamaterial. (b) Wave propagation along the radial direction gradually compresses its tangential wave-vectors, resulting in a magnified image at the outer boundary. The magnified image, once larger than the diffraction limit, will be resolved in the far field.. (c) Experimental demonstration of hyperlens where sub-diffraction-limited pattern can be magnified and detected in the far field. Figure (a) and (b) reprinted by permission from Macmillan Publishers Ltd: [Nature Communications] ([29]), copyright (2012). Figure (c) reprinted with permission from (Liu et al., 2007). Copyright 2007 by the AAAS.

However, this kind of lens can only achieve high resolution in the near field and it can not magnify the image which can be seen in the far field.

In 2003, Pendry proposed to use cylindrical multilayer metamaterial as a lens (Fig. 2.8(a)) [76]. For this geometry, the dispersion relation is Hyperbolic which is given by

$$\frac{k_r^2}{\epsilon_\theta} + \frac{k_\theta^2}{\epsilon_r} = k_0^2 \quad (2.6)$$

where $\epsilon_\theta > 0$ and $\epsilon_r < 0$. This kind of lens is called hyperlens. In the hyperlens, the evanescent wave can only propagate along the longitudinal direction but not in the tangential direction. Thus the wave is compressed in the tangential direction and

we can separate the sub-diffraction-limited feature at the end of the hyperlens (Fig. 2.8(b)) [77]. The image at the end of the hyperlens has been magnified, which can be seen in the far field. Experimental demonstration of the hyperlens is shown in Fig. 2.8(c) [77, 28].

This method uses optical parallelism which is fast, but it is surface bounded and the hyperlens need to contact the sample which may contaminate or damage the sample.

2.4 Optical lithography beyond the diffraction limit

Optical lithography uses optical imaging system to print the circuit image. Some methods in super-resolution imaging can also be modified to improve the pattern resolution in the optical lithography. However, there are also some differences between them. I would like to briefly introduce several methods which have been proposed to overcome the diffraction limit in the optical lithography.

2.4.1 Multi-photon lithography

Multi-photon has been shown to be able to overcome the diffraction limit in the optical imaging. Similar idea has also been proposed to improve the resolution in photolithography [53, 78]. By scanning the focal volume in a programmed 3D pattern through a thick positive photoresist, it is possible to produce patterns with high aspect ratio trenches and multilayered undercut. However, the point-by-point scanning is time-consuming which limits its applications.

Can we print a super-resolution image by two-photon absorption in one step? To see the answer, let us look at the two-photon process induced by a standing wave. The excitation rate is proportional to square of the standing wave intensity which is given by

$$(1 + \cos 2\kappa x)^2 = \frac{3}{2} + 2 \cos 2\kappa x + \cos 4\kappa x \quad (2.7)$$

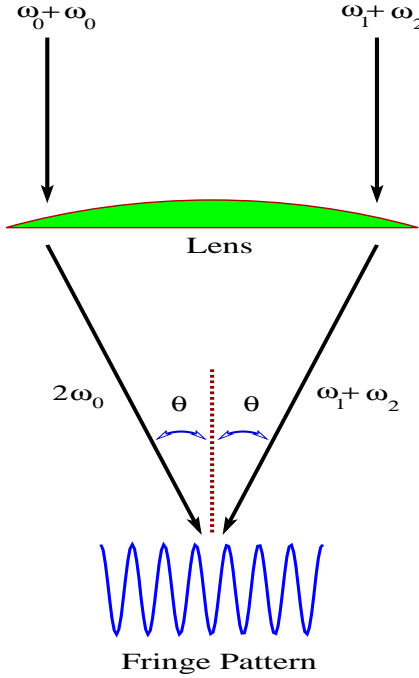


Figure 2.9: The fringe pattern produced by two-photon excitation of a photoresist, in which the incident rays on opposite sides of the lens are separated into distinct frequency grouping. Figure reprinted with permission from (Yablonovitch and Vrijen, 1999). Copyright 1999 by SPIE.

where $\kappa = k \cos \theta$ (k is the wavevector and θ is the incident angle). Comparing the fringe pattern with the one-photon process, we see that the pattern of the two-photon absorption is a mixture of a normal-resolution image represented by $\cos 2\kappa x$ term and a super-resolution image represented by $\cos 4\kappa x$. Indeed, $\cos 4\kappa x$, represents a doubling of the spatial resolution over the one photon process. However, the $\cos 2\kappa x$ term erases this super-resolution.

The second term in Eq. 2.7 comes from the absorption of photons from different paths, i.e, one photon from the left and the other photon from the right. If we can eliminate this term, we can obtain a super-resolution pattern. Yablonovitch and Vrijen (1999) showed that the normal resolution term can be suppressed, using a

classical frequency modulation scheme (Fig. 2.9), where simultaneous absorption of a pair of photons is accompanied by a twofold spatial-resolution enhancement [54]. The incident rays on one edge of the lens have frequency ω_0 , while rays on the other edge consist of two frequencies (i.e., $\omega_1 = \omega_0 + \delta, \omega_2 = \omega_0 - \delta$). Fringes resulting from the interference of rays from opposite edges oscillate rapidly at the different frequency δ and the normal-resolution image is washed away, forming a constant background.

The constant background may be eliminated provided that the atomic transition at $2\hbar\omega_0$ is sufficiently sharp. In this case, the background two-photon transitions of the frequency combinations $\omega_0 + \omega_1, \omega_0 + \omega_2, 2\omega_1$ and $2\omega_2$ do not occur. The background should vanish and leave only the double frequency component. However, multi-photon absorption here requires very high laser intensity which may cause sample damage and it is not easy to generalize to higher order multi-photon absorption.

2.4.2 Quantum NOON state

Quantum NOON state was proposed to effectively eliminate the normal resolution term and achieve sub-diffraction-limited pattern [55]. The system is schematically described in Fig. 2.10, where two photon beams are incident on a symmetric, loss-less beam splitter BS at ports A and B. The output beams get reflected off by a mirror pair into the substrate. The two beams get converged on the imaging plane. The photoresist consists of two-photon absorber.

The basic principle of this scheme can be explained as follows. When the input state is $|\Psi_{11}\rangle = |1_A 1_B\rangle$, i.e., one photon from the upper arm and the other from the lower arm (Fig. 2.10). Interference effect upon passage through a symmetric, lossless beam splitter can cause the product state $|1_A 1_B\rangle$ to become the quantum

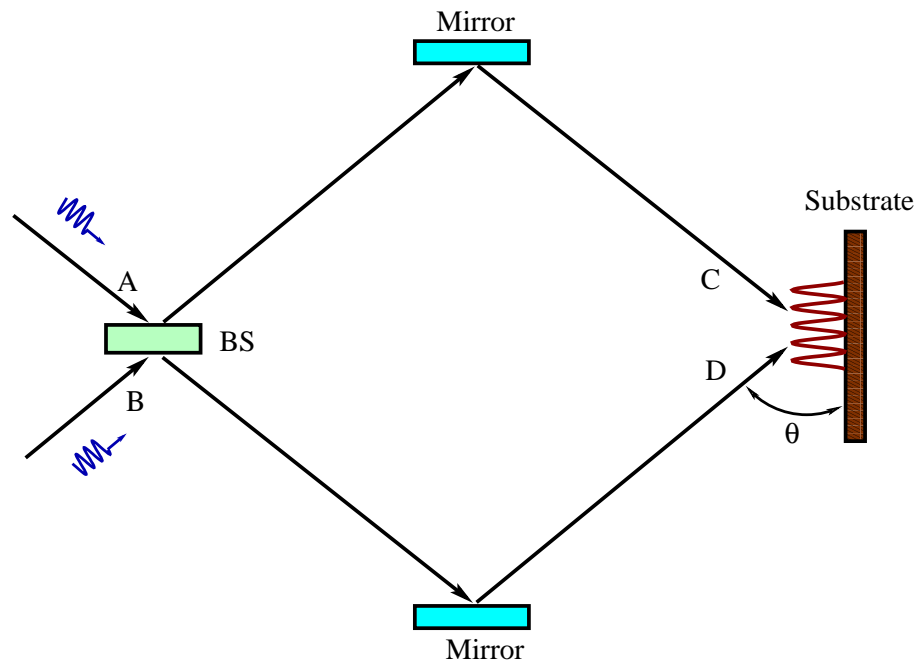


Figure 2.10: Interferometric lithography setup where two photon beams hitting a beam splitter at ports A and B, and then get reflected by two mirrors. The two photon beams get interfere on the substrate. Figure reprinted with permission from (Boto et al., 2000). Copyright 2000 by American Physical Society.

NOON state $(|2_C 0_D\rangle + |0_C 2_D\rangle)/\sqrt{2}$. Hence, the two photons emerge either both in the upper arm C or both in the lower arm D, but never one photon in each arm. Absorption of one photon from upper path and one photon from lower path never happens. The normal resolution term is therefore completely washed away and leaves only the super-resolution term. The photoresist absorbed the two photon together and the deposition rate is then proportional to

$$|e^{2ikx} + e^{-2ikx}|^2 = 2(1 + \cos 4kx) \quad (2.8)$$

which gives rise to a $\lambda/4$ resolution

This result can be generalized if we can somehow prepare the light source in the so-called NOON state, i.e., $|\Psi(N)\rangle = \frac{1}{\sqrt{2}}(|N\rangle_C |0\rangle_D + |0\rangle_C |N\rangle_D)$. The deposition rate on an N -photon absorbing substrate is then prportional to $\Delta_N = 1 + \cos 2Nkx$, with resolution $\lambda_0/2N$.

However, the generation of pure NOON state is very challenging. In addition, this method for subwavelength lithography suffers from some other serious problems as well [30]. On the one hand, one needs to produce weak light field to contain only two photons per mode, and at the same time, use this particular field to excite two-photon absorption which requires a strong field. When one photon is localized, the momentum of the other photon becomes completely delocalized, and thus this photon can end up anywhere [79]. Hence, the general usefulness of this method is quite limited.

2.4.3 Quantum inspired technique: dopperlon

While quantum entanglement can help to suppress the normal resolution term, people showed that this quantum effect can also be mimicked by the classical light. One example is Doppleron which is proposed by Hemmer et al. [57]. The basic idea of

this scheme is shown in Fig. 2.11(a). Two counter-propagating plane waves consisting of signal frequencies ν_{\pm} interfere on a photosensitive substrate. The driving fields ω_{\pm} assist a directional resonance for pairs of signal photons, i.e.,

$$\omega_{ab} = 2\nu_{\pm} - \omega_{\pm}. \quad (2.9)$$

If the atomic linewidth is narrow, the \pm channels will realize distinct resonances [80]. The atoms will either absorb two photons from the left beam or two photons from the right beam, but never one photon from each beam, which is similar to the path-number entanglement in the quantum field lithography. As a consequence, the one-photon interference term will be suppressed and keep only the pure two-photon interference term which has a resolution half of the diffraction limit.

This method can also be generalized to higher order multi-photon resonance. The schematics for the system are given in Fig. 2.11(b). Two bunches of signal fields counter-propagate along the substrate ($\theta = \pi/2$) and a driving field is incident normally. Either bunch of fields together with the driving field can excite the multiphoton transition from level $|b\rangle$ to $|a\rangle$. The photons from the signal fields of frequencies $\nu_{n\pm}$ are absorbed and the photons of the driving field with frequency ω_0 are emitted. The N signal photons satisfy a frequency summation resonance condition [57]

$$\sum_{n=1}^N \nu_{n\pm} = \omega_{ab} + (N-1)\omega_0 = N\nu_0, \quad (2.10)$$

such that the N -photon wavevector, $N\nu_0/c = 2\pi/(\lambda_0/N)$ is the same for both bunches. We further require that any interchange of photons between bunches, $\nu_{n+} \leftrightarrow \nu_{n'-}$, results in a loss of resonance. Therefore only two resonant processes make up the interference.

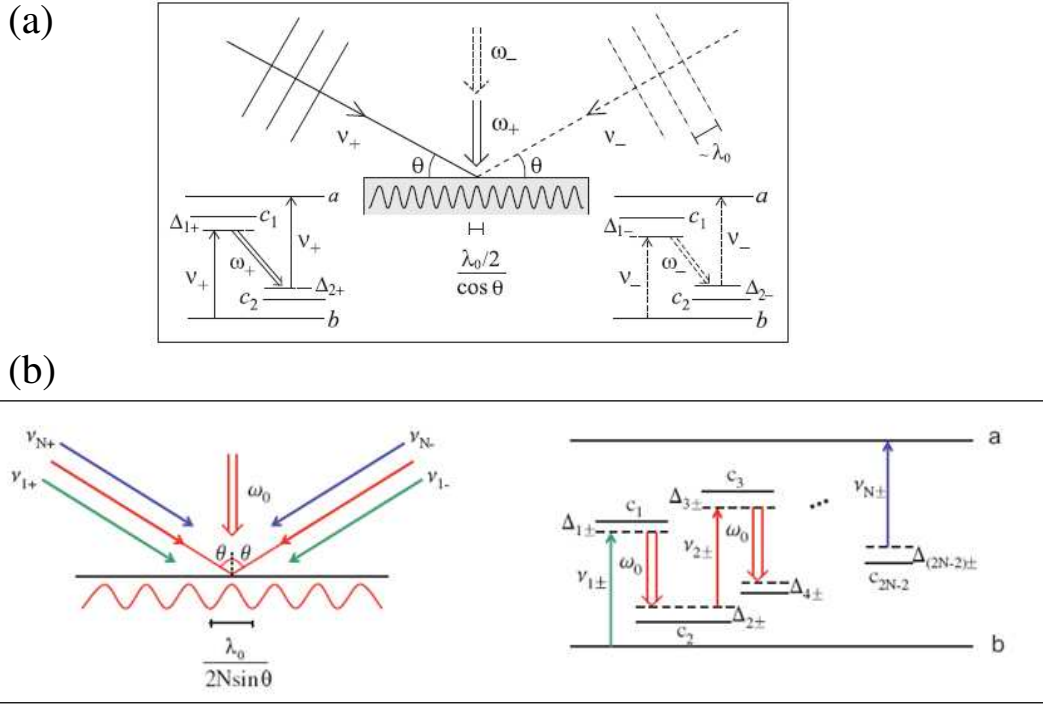


Figure 2.11: (a) Subwavelength interference with classical light. Two counter-propagating plane waves consisting of signal frequencies ν_{\pm} interfere on a photo-sensitive substrate. The drive fields ω_{\pm} assist a directional resonance for pairs of signal photons. (b) Left: The scheme of interferometric lithography. Two bunches of signal fields counterpropagate ($\theta = \pi/2$) and the drive field incidents normally. Right: The level structure of the substrate atom. Either bunch of fields together with the drive field satisfies the multiphoton resonance. $\Delta_{n\pm}$ is the detuning of intermediate level c_n . Figure reprinted with permission from (Hemmer et al., 2006 and Sun et al., 2007). Copyright 2006, 2007 by the American Physical Society.

Under the conditions of multiphoton resonance, the leading contribution to the multiphoton excitation rate comes from the two resonant processes, i.e.,

$$R^{(2N-1)}(x, t) \propto \frac{d}{dt} \left| e^{i\frac{N\nu_0 x}{c}} r_+^{(2N-1)}(t) + e^{-i\frac{N\nu_0 x}{c}} r_-^{(2N-1)}(t) \right|^2. \quad (2.11)$$

If the one-photon detunings are large and $\mathcal{E}_{S_{n\pm}}$ are suitably chosen, the excitation amplitudes $r_{\pm}(t)$ can be made approximately equal with a phase difference. Factoring them out we find that the remaining expression looks like the interference of single photon absorption with $k = N\nu_0/c$. So the exposure pattern are fringes with distance $\lambda_0/2N$.

This method can eliminate the normal resolution term without quantum entanglement. However, the visibility of this method is reduced and it is also not easy to generalize to higher resolution in practice due to the complicated process.

2.4.4 Coherent population trapping

In 2008, Kiffner et al. presented an alternative scheme for resonant subwavelength lithography without the requirement of an N -photon absorption process [32]. This scheme relied on the phenomenon of coherent population trapping (CPT) [81, 82]. Atoms are prepared in a position dependent state and the sub-wavelength spatial distribution comes from the phase shifted standing wave patterns in a multilevel resonant atom-field system.

It is known that CPT occurs in a three-level Λ type system as shown in Fig. 2.12(a). The two ground states are represented by $|b_1\rangle$ and $|b_2\rangle$, which are resonantly coupled to the excited state $|a_1\rangle$ by the laser fields with Rabi frequencies \mathcal{R}_1 and \mathcal{S}_1 , respectively. In such configuration, we can get the dark state once the system is optically pumped into a coherent superposition of the two ground states which is

then decoupled from the applied light fields. The dark state is given by

$$|D_\Lambda\rangle = (\mathcal{S}_1|b_1\rangle - \mathcal{R}_1|b_2\rangle)/\sqrt{|\mathcal{S}_1|^2 + |\mathcal{R}_1|^2}. \quad (2.12)$$

If the two laser fields are standing waves and they are phase shifted by $\pi/2$, i.e.,

$$\mathcal{R}_1 = \Omega_0 \cos(k_0 z), \quad \mathcal{S}_1 = \Omega_0 \sin(k_0 z). \quad (2.13)$$

The populations of $|b_1\rangle$ and $|b_2\rangle$ in $|D_\Lambda\rangle$ are then given by

$$|\langle b_1 | D_\Lambda \rangle|^2 = \frac{|\mathcal{S}_1|^2}{|\mathcal{R}_1|^2 + |\mathcal{S}_1|^2} = [1 - \cos(2k_0 z)]/2, \quad (2.14)$$

$$|\langle b_2 | D_\Lambda \rangle|^2 = \frac{|\mathcal{R}_1|^2}{|\mathcal{R}_1|^2 + |\mathcal{S}_1|^2} = [1 + \cos(2k_0 z)]/2. \quad (2.15)$$

The two ground states populations show the same spatial modulation as the intensity profiles of the standing waves corresponding to \mathcal{S}_1 and \mathcal{R}_1 , respectively. It is important to note that the populations do not depend on the maximal Rabi frequency $|\Omega_0|$, but rather on the ratio of the Rabi frequencies \mathcal{R}_1 and \mathcal{S}_1 . Here the atomic population in (say level $|b_1\rangle$) is modulated with spatial frequency $2k_0$ giving a resolution of $\lambda_0/2$ which gives the same result as the Reyleigh limit.

The above result for a single Λ type three-level system can be generalized to $2 \times \Lambda$ or so-called M system, see Fig. 2.12(b). The dark state of this system is given by [83]

$$|D_{2 \times \Lambda}\rangle = (\mathcal{S}_1 \mathcal{S}_2 |b_1\rangle - \mathcal{R}_1 \mathcal{S}_2 |b_2\rangle + \mathcal{R}_1 \mathcal{R}_2 |b_3\rangle)/\sqrt{C_2}, \quad (2.16)$$

where $\mathcal{S}_{1,2}$ and $\mathcal{R}_{1,2}$ are the driving fields, and C_2 is the normalization constant. The probability to find the system in state $|b_1\rangle$ is proportional to $|\mathcal{S}_1 \mathcal{S}_2|^2$. This involves the product of the fields \mathcal{S}_1 and \mathcal{S}_2 . If both \mathcal{S}_1 and \mathcal{S}_2 have a sinusoidal oscillation

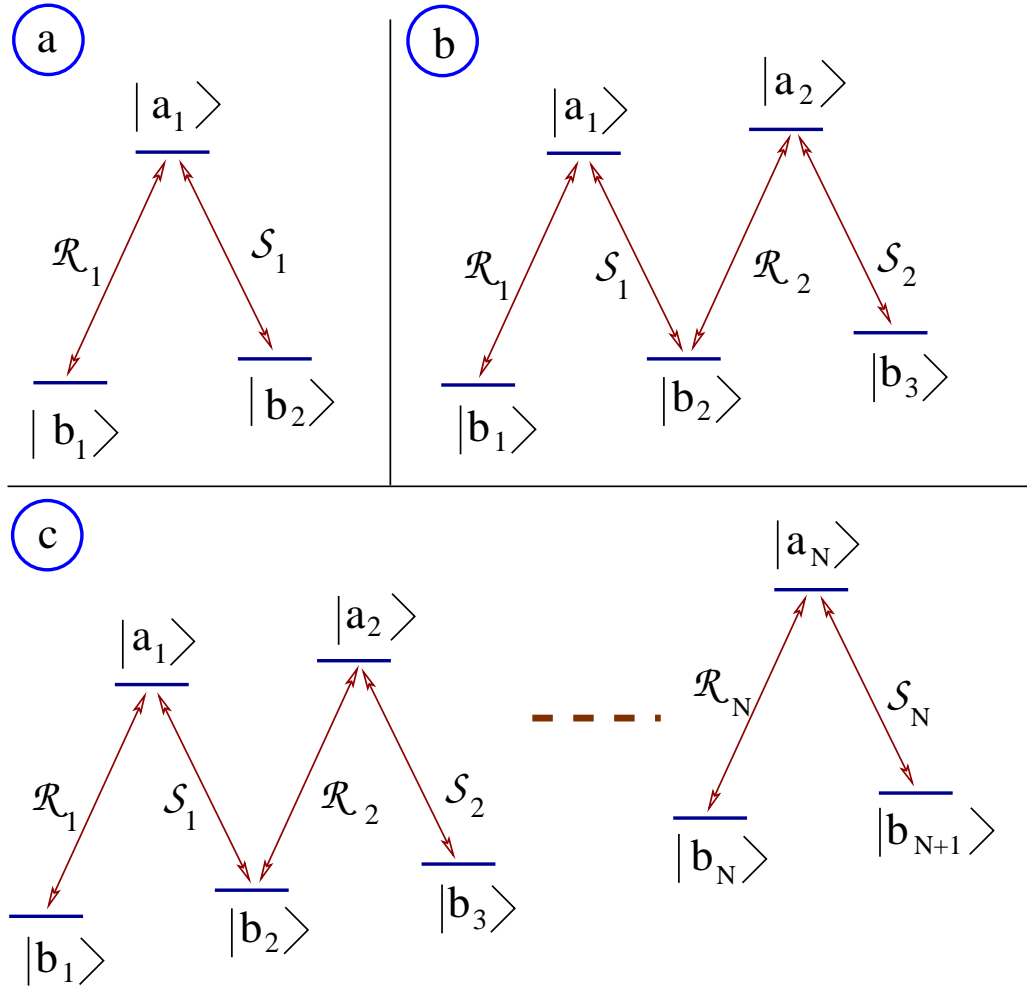


Figure 2.12: Considered level schemes of the substrate. The ground states $|b_n\rangle$ and $|b_{n+1}\rangle$ are resonantly coupled to the excited state $|a_n\rangle$ via Rabi frequencies Ω_{R_n} and Ω_{S_n} , respectively. Each excited state $|a_n\rangle$ decays to the ground states $|b_n\rangle$ and $|b_{n+1}\rangle$ by spontaneous emission. (a) Single Λ system. In (b), a sequence of two Λ systems is displayed. (c) General level scheme with N excited and $N + 1$ ground states as a sequence of N Λ -type systems. Figure reprinted with permission from (Kiffner et al., 2008). Copyright 2008 by the American Physical Society.

behavior with respect to position, i.e. $\mathcal{S}_1 \sim \sin(k_0 z)$ and $\mathcal{S}_2 \sim \sin(k_0 z + \phi)$, we obtain

$$|\mathcal{S}_1 \mathcal{S}_2|^2 \sim [\cos(\phi) - \cos(2k_0 z + \phi)]^2 \quad (2.17)$$

If we choose the relative phase shift of the two standing waves as $\phi = \pi/2$, we have:

$$|\mathcal{S}_1 \mathcal{S}_2|^2 \sim [1 - \cos(4k_0 z)]/2. \quad (2.18)$$

The population modulations with wave number $4k_0$ are obtained, while the contribution with wave number $2k_0$ has been canceled. The spatial resolution is half of the diffraction limit!

This scheme can be also generalized to an $N \times \Lambda$ structure (Fig. 2.12(c)), which can in principle give N times better resolution than the diffraction limit. For details, please refer to Ref. [32]. The advantage of this method is that it can work at lower laser intensities. There is no need for nonlinear transition amplitudes between different states but rather one exploits the nonlinear dependence of the ground state population probabilities on the Rabi frequencies, which only depends on relative field strengths. However, this scheme needs very complicated atomic structure and multiple beams, which is not easy to be realized in practice.

3. OPTICAL LITHOGRAPHY BEYOND THE DIFFRACTION LIMIT VIA SPATIAL RABI OSCILLATIONS*

In this chapter, I will present our method to achieve sub-diffraction-limited resolution in the optical lithography. Our method is close to the traditional optical lithography but adding a critical step before dissociating the chemical bound of the photoresist. The subwavelength pattern is achieved by inducing the coherent Rabi oscillations between the ground state and one intermediate state. The proposed method does not require multiphoton absorption and quantum entanglement of photons. Extension from lower resolution to higher resolution is very straightforward where we just need to increase the laser intensity or the pulse duration.

3.1 Coherent Rabi oscillations between two atomic levels

3.1.1 *Rabi oscillations without dissipation*

When a two-level atom or molecule interacts with a laser light, the Hamiltonian can be written as [82]

$$H = H_0 + H_I = \hbar\Delta|a\rangle\langle a| + \frac{\hbar\Omega_R(t)}{2}(|a\rangle\langle b| + |b\rangle\langle a|) \quad (3.1)$$

where Δ is the detuning between the two energy levels and frequency of the light, $\Omega_R(t) = \mu\mathcal{E}(t)/\hbar$ is the Rabi frequency.

According to the Schrödinger equation, the dynamics of the system are governed

*Reprinted with permission from Quantum Lithography beyond the Diffraction Limit via Rabi Oscillations by Z. Liao and M. Al-amri and M. S. Zubairy, 2010. Phys. Rev. Lett., vol. 105, pp. 183601, Copyright [2010] by the American Physical Society.

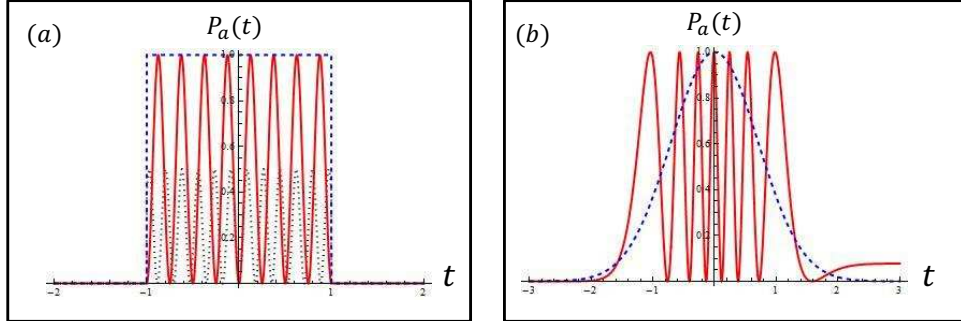


Figure 3.1: Rabi oscillations for (a) square pulse: Blue dashed line is the pulse shape, red solid line is the probability in the excited state in the resonant case, while the black dotted line is the probability in the excited state when $\Delta = \Omega_R$. (b) Gaussian pulse: Blue dashed line is the pulse shape, red solid line is the probability in the excited state in the resonant case.

by

$$i \frac{d}{dt} \begin{bmatrix} C_a(t) \\ C_b(t) \end{bmatrix} = \begin{bmatrix} \Delta & \Omega_R(t) \\ \Omega_R(t) & 0 \end{bmatrix} \begin{bmatrix} C_a(t) \\ C_b(t) \end{bmatrix}$$

where $C_a(t)$ ($C_b(t)$) is the probability amplitude in the excited (ground) state.

For the most general situation, there is not known analytical solution for the above coupled equations. However, there are special cases that we can analytical solve the coupled equations, e.g., the Rabi frequency Ω_R is independent of time or the resonant case $\Delta = 0$. For the first case, the solution is given by

$$C_a(t) = -i \frac{\Omega_R}{\Omega} \sin\left(\frac{\Omega t}{2}\right) \quad (3.2)$$

where $\Omega = \sqrt{\Omega_R^2 + \Delta^2}$ is the effective Rabi frequency. One example is shown in Fig. 3.1(a) where we can see the population in the excited state oscillates with time. When there is detuning, the period of the oscillations becomes smaller while the amplitude of the oscillations decreases. For the resonant case, the solution can be

obtained according to the pulse area theorem (Appendix A)

$$C_a(t) = \frac{1 - \cos \theta(t)}{2} \quad (3.3)$$

where we assume that initially the atom is in the ground state and $\theta(t) = \int_{-\infty}^t \Omega_R(t') dt'$ is the pulse area. One example is shown in Fig. 3.1(b).

3.1.2 Rabi oscillations with dissipation

For real system, dissipation can not be avoided. Here I will mainly discuss the effects of two kinds of dissipation, i.e., decay and dephasing. The dynamics of a dissipation system can be described by the Liouville master equation

$$\dot{\rho} = -\frac{i}{\hbar}[H, \rho] - \mathcal{L}\rho \quad (3.4)$$

where $\mathcal{L}\rho$ is the relaxation of the system which is given by

$$\mathcal{L}\rho = \begin{bmatrix} \frac{1}{T_1}\rho_{aa} & \frac{1}{T_2}\rho_{ab} \\ \frac{1}{T_2}\rho_{ba} & -\frac{1}{T_1}\rho_{aa} \end{bmatrix}$$

where T_1 is the population decay time while T_2 is the dephasing time.

To see the effects of the decay and dephasing process to the Rabi oscillations, we can numerically solve the dynamics of the system. For simplicity, let us assume that the driving field is continuous. The numerical results are shown in Fig. 3.2. The amplitude of the population oscillation decreases when the system has decay or dephasing (Fig. 3.2(a, b)). Thus, the decay time T_1 and dephasing time T_2 are both important for the coherent Rabi oscillation process.

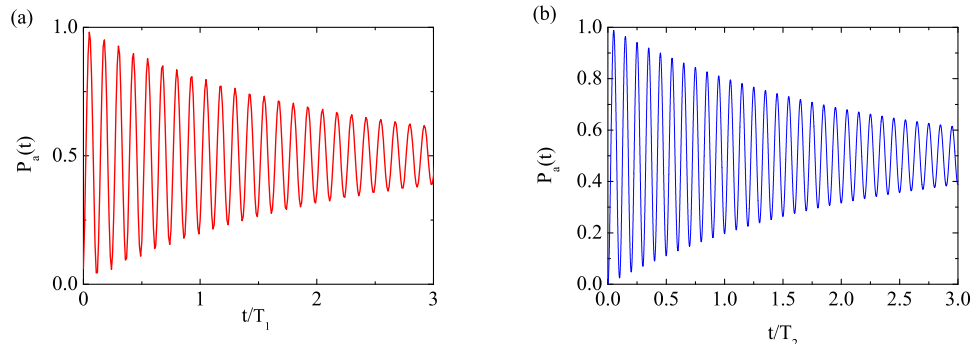


Figure 3.2: Rabi oscillations with decay (a) and with pure dephasing (b).

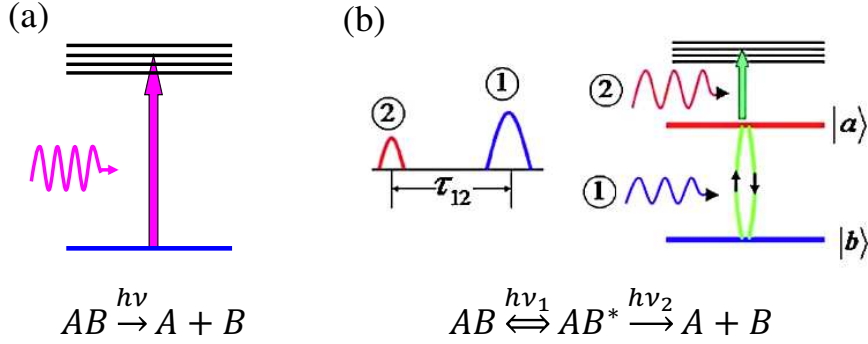


Figure 3.3: Comparison between the traditional optical lithography (a) and our lithography scheme (b).

3.2 Optical lithography beyond the diffraction limit via coherent Rabi gradient

In the traditional optical lithography, a laser beam is applied to dissociate the photoresist molecules directly (Fig. 3.3(a)). In our scheme, we sequentially turn on two laser pulse with two different frequencies instead of only one beam of laser and three energy levels are involved in this process (Fig. 3.3(b)) [59]. The first laser pulse with gradient field strength in the space is applied to induce multiple Rabi oscillations between the ground state $|b\rangle$ and one intermediate excited state $|a\rangle$. After that,

the second laser pulse is applied to dissociates the molecules in the excited states but not those in the ground state. The dissociation of the molecules cuts the chemical bond and changes the chemical properties of the photresist. We can then use photoresist developer to wash out the dissociated molecules or undissociated molecules [84, 85]. The resulting patterns of the photoresist should then depend on the spatial distribution of the excited state induced by the first laser pulse. If the spatial modulation of the probability to find the molecules at excited state has subwavelength pattern, then the resulting patterns of the photoresist is also subwavelength.

3.2.1 Achieving the sub-wavelength pattern

The first step is critical in order to achieve the sub-wavelength pattern. We illustrate it in more details and show how to prepare the molecules in a sub-wavelength position dependent state. Two beams of light from opposite directions are incident on the photoresist and they form a standing wave on the surface of the photoresist. The standing light field interacts with the molecules in the photoresist, for which we consider two kinds of light sources: Continuous wave and a Gaussian pulse.

3.2.1.1 Continuous wave analysis

For simplicity, we first consider the continuous wave with frequency resonant to the two atomic levels. The standing electric field on the surface is

$$\begin{aligned} E(\mathbf{r}, t) &= E_0 \cos(\nu_1 t) e^{i\mathbf{k}\cdot\mathbf{r}} + E_0 \cos(\nu_1 t) e^{-i(\mathbf{k}\cdot\mathbf{r}+2\phi)} \\ &= 2E_0 e^{-i\phi} \cos(kx \cos \theta + \phi) \cos(\nu_1 t) \end{aligned} \quad (3.5)$$

in which E_0 is the field amplitude, ν_1 is the frequency, θ is the angle between the incident light and the surface, and 2ϕ is the phase difference of the two beams. Considering the dipole interaction between the electric field and the atoms, and for

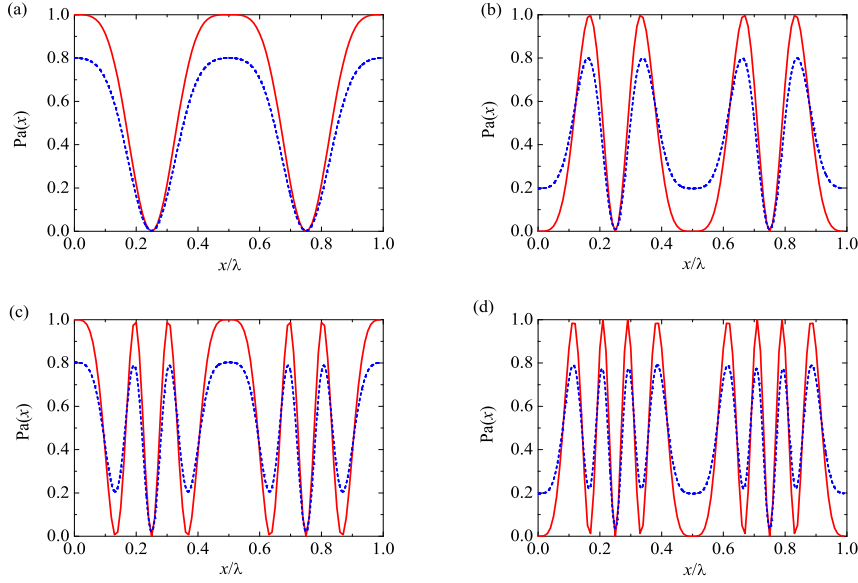


Figure 3.4: Subwavelength patterns generated by fields of different $\Omega_R T$. (a) $\Omega_R T = \pi$; (b) $\Omega_R T = 2\pi$; (c) $\Omega_R T = 3\pi$; (d) $\Omega_R T = 4\pi$. The solid line is when the decay is not included whereas the blue dashed line shows the results with $\gamma = \omega_{ab}/1000$.

the resonant case where $\nu_1 = \omega$, the probability for the atoms to be in the excited state $|a\rangle$ at time T is given by

$$P_a(x, T) = \frac{1 - \cos [\Omega_R T \cos(kx \cos \theta + \phi)]}{2}, \quad (3.6)$$

where we assume that the atoms are initially in the ground state, $\Omega_R = (2|\varphi_{ba}|E_0)/\hbar$ is the Rabi frequency at the peak electric intensity, and $|\varphi_{ba}|$ is the amplitude of the electric dipole moment. From this equation, we can see that the probability in the excited state is spatially dependent and the shape depends on the field area $\Omega_R T$.

We now look at the spatial pattern in more details. For simplicity, we choose $\theta = 0$ and $\phi = 0$ which does not change the overall properties. In this case, we have $P_a(x, T) = (1 - \cos[\Omega_R T \cos(kx)])/2$ which is a double cosine function and we can

calculate the positions of the valleys and the peaks. First, we note that the usual Rayleigh limit is obtained in the linear approximation corresponding to $\Omega_R T \ll 1$. In this region $P_a(x, T) \approx \alpha(1 + \cos(2kx))$ with $\alpha = (\Omega_R T)^2/8$ leading to a resolution of $\lambda/2$. Next we look at the situation where we are not restricted by the linear approximation and multiple Rabi oscillations are allowed during the interaction time T .

When $\cos(kx) = 2m\pi/\Omega_R T$, the probability $P_a(x, T)$ is 0 which corresponds to the valleys, and when $\cos(kx) = (2m + 1)\pi/\Omega_R T$, the probability is 1 which corresponds to the peaks, where $m = 0, \pm 1, \pm 2, \dots$. It is readily seen that when $\Omega_R T = \pi$, there are two valleys ($x = \lambda/4, 3\lambda/4$) and three peaks ($x = 0, \lambda/2, \lambda$) within one wavelength Fig. 3.4(a), which gives the same result as the classical interference lithography. However, when $\Omega_R T \geq 2\pi$, more valleys and peaks appear and the classical limitation is broken. For example, when $\Omega_R T = 2\pi$, there are five valleys ($x = 0, \lambda/4, \lambda/2, 3\lambda/4, \lambda$) and four peaks ($x = \lambda/6, \lambda/3, 2\lambda/3, 5\lambda/6$) within one wavelength Fig. 3.4(b). When $\Omega_R T$ becomes larger, the pattern becomes smaller Fig. 3.4(c-d). Therefore, it is in principle possible to achieve arbitrarily smaller sub-wavelength patterns by using stronger field or longer interaction time to induce more Rabi oscillations.

The physics behind the sub-wavelength pattern is the nonlinearity associated with the Rabi oscillations. For example, when $\Omega_R T = \pi$, one photon is absorbed and we are about in the linear regime. The corresponding resolution is about the same as that obtained in the classical lithography Fig. 3.4(a). When $\Omega_R t = 2\pi$, one photon is absorbed and one photon is emitted, leading to a full Rabi cycle. It is coherent two-photon process. The resulting resolution is half of the one-photon process Fig. 3.4(b). When more and more photons are involved, we can get higher and higher resolution.

In order to see clearly the advantage of the present method over any previous methods for super-resolution optical lithography, we refer to Eq. 3.6. In the case when $\phi = \pi/2$, and $kx \cos \theta \ll 1$, Eq. 3.6 reduces to

$$P_a = \frac{1 - \cos(2k_{eff}x)}{2}, \quad (3.7)$$

where $k_{eff} = \Omega_R T k \cos \theta$ and the effective period is given by

$$\lambda_{eff} = \lambda / (\Omega_R T \cos \theta). \quad (3.8)$$

A large number of Rabi oscillations in the interaction time can lead to an arbitrarily small effective wavelength. Therefore a novel feature of our scheme is that it should be possible to generate a nano-scale pattern using a microwave field. For example, if two sublevels of a system have energy difference of about 3 GHz and the coherence time is of the order of 1 s, we can use a microwave pulse with wavelength 10 cm and pulse duration 0.1 s to induce the Rabi oscillations between these two levels. If $\Omega_R = 0.1$ GHz, the resolution could be of the order 10 nm.

3.2.1.2 Gaussian pulse analysis

So far we considered the light field to be a continuous wave. However, in practical applications we usually use laser pulses instead. Our study shows that the result of the laser pulses is similar to that of the continuous wave.

Two beams of Gaussian pulses with the same frequency ν_1 , same maximal amplitude E_0 and same full width at half maximum of the intensity $t_{FWHM} = 2\sqrt{\ln 2}\sigma$ are incident on the photoresist from opposite directions with angle θ , and σ is the width of the pulse (Fig. 3.5(a)). They then form a standing electric field described

by

$$E(x, t) = 2E_0 \exp\left(-\frac{t^2}{2\sigma^2}\right) \cos(kx \cos \theta + \phi) \cos(\nu_1 t) \quad (3.9)$$

where ϕ is the phase difference between the two pulses. The electric field couples to the molecules in the photoresist. If ν_1 is resonant to the two atomic levels $|a\rangle$ and $|b\rangle$, the electric field drives Rabi oscillations between the two atomic levels. The Rabi frequency is $\Omega_R(x, t) = 2|\varphi_{ba}|E_0 \exp\left(-\frac{t^2}{2\sigma^2}\right) \cos(kx \cos \theta + \phi)/\hbar$. According to the Area theorem (Appendix A), the upper-level probability after the pulse is given by

$$\begin{aligned} P_a(x) &\simeq \frac{1 - \cos[\int_{-\infty}^{\infty} \Omega_R(x, t) dt]}{2} \\ &= \frac{1 - \cos[2\sqrt{2\pi}\sigma \frac{|\varphi_{ba}|E_0}{\hbar} \cos(kx \cos \theta + \phi)]}{2} \\ &= \frac{1 - \cos[\Omega_0 t_0 \cos(kx \cos \theta + \phi)]}{2} \end{aligned} \quad (3.10)$$

where $\Omega_0 = 2|\varphi_{ba}|E_0/\hbar$ is the maximal Rabi frequency and we define $t_0 = \sqrt{\frac{\pi}{2\ln 2}} t_{FWHM}$. From the equation, we see that the pattern generated by the Gaussian pulse is the same as that of the continuous wave, but just replace T by t_0 . For example, when $\Omega_0 t_0 = 2\pi$, one Rabi cycle is driven and the pattern has a resolution of $\lambda/4$ Fig. 3.5(b) which is the same as Fig. 3.4(b). When $\Omega_0 t_0 = 4\pi$, two Rabi cycles are driven and the resolution is $\lambda/8$ Fig. 3.5(b) which is the same as Fig. 3.4(d). Therefore, our scheme also works for pulse excitation. The duration of the pulse should be less than the population decay time.

3.2.2 Arbitrary sub-wavelength patterns in a macroscopic area

In the previous section we have shown how to achieve a simple sub-wavelength pattern via coherent Rabi oscillations. For any practical applications we need to

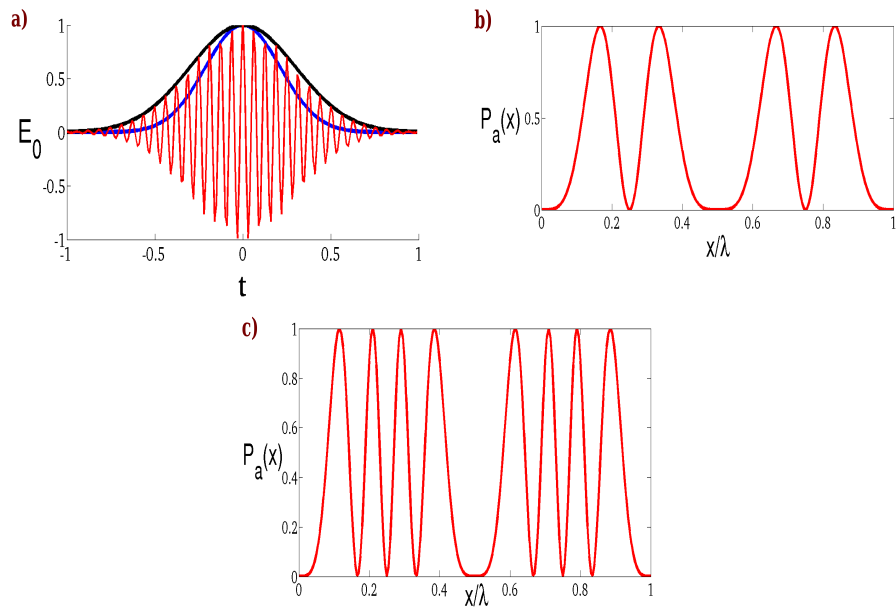


Figure 3.5: (a) The Gaussian pulse. The red dash line is the amplitude profile and the thick dark line is the intensity profile; (b) The pattern produced by the Gaussian pulse when $\sqrt{\frac{\pi}{2 \ln 2}} \Omega_0 t_{FWHM} = 2\pi$; (c) The pattern produced by the Gaussian pulse when $\sqrt{\frac{\pi}{2 \ln 2}} \Omega_0 t_{FWHM} = 4\pi$. The solid line is the result without the decoherence while the green dashed line shows the results with $t_{FWHM} = \tau/2$.

produce more complicated patterns [86, 87, 88]. In the following, we will discuss how to produce arbitrary sub-wavelength patterns in a macroscopic area [59, 60]. For one dimensional case, any functions in the range L can be expanded as a Fourier series:

$$f(x) = \frac{a_0}{2} + \sum_{n=1}^{\infty} [a_n \cos\left(\frac{2n\pi x}{L}\right) + b_n \sin\left(\frac{2n\pi x}{L}\right)] \quad (3.11)$$

For the components with periods L/n larger than optical wavelength λ , we just use the traditional way, i.e, shine two dissociative lasers with frequency large enough to dissociate the molecules directly and they form a standing wave correspond to the component and with strength related to the Fourier coefficient. For the components with $L/n < \lambda$, we need to apply our sub-wavelength scheme. We shine two phase locked pulses with amplitude E_0 from angle θ to form a standing wave and the third one with amplitude E_1 from the right angle to form a constant background. The resulting electric field is $E(x, t) = [2E_0 \cos(kx \cos \theta + \phi) + E_1] \exp(-\frac{t^2}{2\sigma^2}) \cos(\nu_1 t)$. When $n\pi - \epsilon \leq kx \cos \theta \leq n\pi + \epsilon$ (n is an integer and ϵ is a small number),

$$E(x, t) \simeq \pm[2E_0 kx \cos \theta + E_1] \exp(-\frac{t^2}{2\sigma^2}) \cos(\nu_1 t) \quad (3.12)$$

where ϕ is set to be 90 degree. Then the Rabi frequency is

$$\begin{aligned} \Omega_R(x) &= \frac{2|\varphi_{ab}|}{\hbar} [E_0 \cos(kx \cos \theta + \phi) + E_1] \\ &\approx \frac{2|\varphi_{ab}| E_0 k \cos \theta}{\hbar} x + \frac{2|\varphi_{ab}| E_1}{\hbar} \end{aligned} \quad (3.13)$$

The Rabi frequency is approximately a linear function of the position, and the gradient of the intensity is approximately a constant in the region $(n\pi - \epsilon)/k \cos \theta \leq$

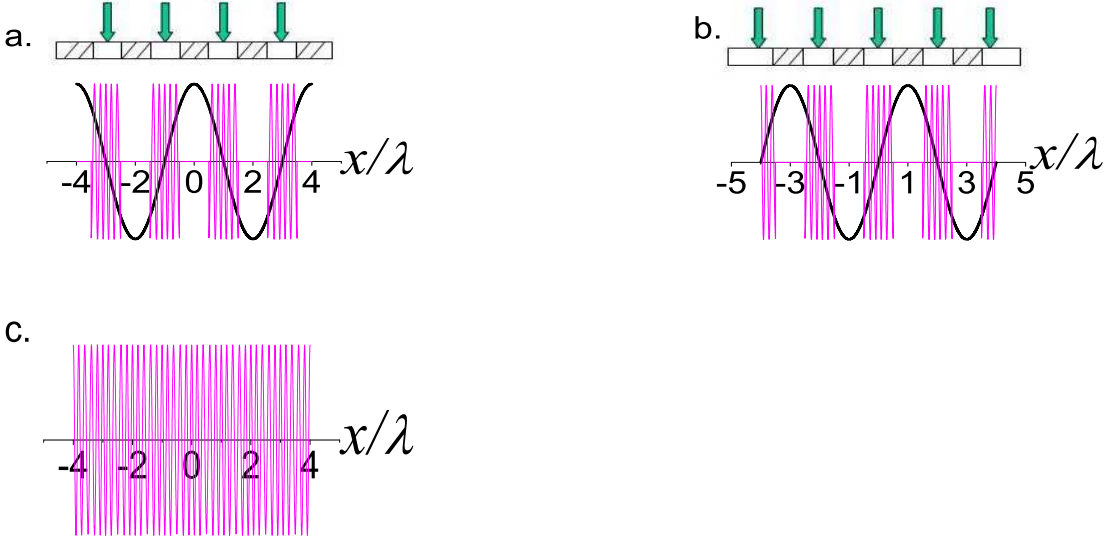


Figure 3.6: A proposed scheme to print a sine pattern in an arbitrary large region.

$x \leq (n\pi + \epsilon)/k \cos \theta$. Then the pattern produced in this linear region is

$$P_a(x, T) \simeq \frac{1 - \cos(Ax + B)}{2} \quad (3.14)$$

where $A = \sqrt{2\pi/\ln 2}\Omega_0 t_{FWHM} k \cos \theta$ and $B = \sqrt{2\pi/\ln 2}\Omega_1 t_{FWHM}$. The coefficients A and B can be controlled by the field strength and the pulse time. The effective wavelength

$$\lambda_{eff} = \lambda / (\sqrt{2\pi/\ln 2}\Omega_0 t_{FWHM} \cos \theta) \quad (3.15)$$

can be arbitrary small by using stronger field or longer pulse time. We note that ignoring the constant background 1/2, when $B = 0$, the pattern is a cosine function; when $B = \pi/2$, the pattern is a sine function.

For example, if we want to produce a sine pattern with $\lambda/5$ resolution in a large region, we can do it in two steps (Fig. 3.6): First, we etch the pattern in the linear

region as shown in Fig. 3.6(a). We then shift the standing wave by a phase $\pi/2$ such that the linear region shifts by a distance of $\lambda/2$. This allows us to write the sine pattern in the remaining region Fig. 3.6(b) thus leading to the resulting sine pattern in the entire region as shown in Fig. 3.6(c). The peak power for E_0 is about $15MW/cm^2$ ($\cos(\theta) = 1/4$, $|\phi_{ab}| = 10Debye$, $t_{FWHM} = 1ps$) (Becker et al., 1988) and the peak power for E_1 is about $0.37MW/cm^2$. For larger resolution, the peak power should increase. For example, to reach $\lambda/10$ resolution, the peak power for E_0 is about $60MW/cm^2$ and the peak power for E_1 is about $0.37MW/cm^2$. In addition, for the Fourier coefficients a_n and b_n , we can control the strength and the time duration of the dissociation pulse to control the dissociation rate or we can use different wavelengths with different absorption rates.

We can also generalize our method to two dimensional patterns. Arbitrary 2D periodic function with $f(x + \lambda, y + \lambda) = f(x, y)$ can be simulated by the truncated Fourier series:

$$\begin{aligned}
f(x, y) &= \sum_{m=0}^M \sum_{n=0}^N \left\{ a_{mn} \cos\left[\frac{2\pi(mx + ny)}{\lambda}\right] + b_{mn} \cos\left[\frac{2\pi(mx - ny)}{\lambda}\right] \right. \\
&\quad \left. + c_{mn} \sin\left[\frac{2\pi(mx + ny)}{\lambda}\right] + d_{mn} \sin\left[\frac{2\pi(mx - ny)}{\lambda}\right] \right\} \\
&\approx \sum_{m=0}^M \sum_{n=0}^N \left\{ a_{mn} \cos\left[\frac{\sqrt{m^2 + n^2}}{\cos(\theta)} \cos\left[\frac{2\pi \cos(\theta)}{\lambda} \frac{(mx + ny)}{\sqrt{m^2 + n^2}} + \frac{\pi}{2}\right]\right] \right. \\
&\quad \left. + b_{mn} \cos\left[\frac{\sqrt{m^2 + n^2}}{\cos(\theta)} \cos\left[\frac{2\pi \cos(\theta)}{\lambda} \frac{(mx - ny)}{\sqrt{m^2 + n^2}} + \frac{\pi}{2}\right]\right] \right. \\
&\quad \left. + c_{mn} \sin\left[\frac{\sqrt{m^2 + n^2}}{\cos(\theta)} \cos\left[\frac{2\pi \cos(\theta)}{\lambda} \frac{(mx + ny)}{\sqrt{m^2 + n^2}} + \frac{\pi}{2}\right]\right] \right. \\
&\quad \left. + d_{mn} \sin\left[\frac{\sqrt{m^2 + n^2}}{\cos(\theta)} \cos\left[\frac{2\pi \cos(\theta)}{\lambda} \frac{(mx - ny)}{\sqrt{m^2 + n^2}} + \frac{\pi}{2}\right]\right] \right\} \quad (3.16)
\end{aligned}$$

in which θ is near 90° . In the practical application, we should realize each Fourier component one by one. For the first and third components in Eq. 3.16 we shine the

pulses from directions $(m\hat{x} + n\hat{y})/\sqrt{m^2 + n^2}$ while for the other two components we shine the pulses from directions $(m\hat{x} - n\hat{y})/\sqrt{m^2 + n^2}$ and $\Omega_0 t_0 = \sqrt{m^2 + n^2}/\cos(\theta)$. Besides, due to the constant $1/2$ appears in Eq. 3.14, there is an additional penalty deposition Q which depends on the Fourier coefficients. For example, applying the numerical simulation we print characters "TAMU-KACST" within one wavelength (Fig. 3.7). In the simulation, we take $\theta = 80^\circ$ and $M = N = 15$. $Q \sim h$ where h is the height of the pattern. We have a total of $15 \times 15 \times 4 = 900$ components and each component needs 4 pulses (three for standing wave and one for dissociation). Therefore we need 3600 pulses in total. Each component takes about $1ms$ and the whole process takes about $1s$. In our example with the region $\lambda \times \lambda$, the required maximal power is about $200MW/cm^2$ for a pulse duration of $t_0 = 5ps$.

3.2.3 Potential realizations

The scheme shown in Fig. 3.5 is a simplified model. In the following we introduce two possible realizations of our scheme in two different systems.

The first one is in the organic molecular photochemistry. The typical state energy diagram for the chemical bound is shown in Fig. 3.8 [85]. Here S_0 and S_1 are the ground singlet state and the first excited singlet state, respectively and T_1 is the first excited triplet state. K_F is the fluorescence decay rate from S_1 to S_0 ; K_P is the phosphorescence decay rate from T_1 to S_0 ; while K_{ST} is the intersystem crossing rate from S_1 to T_1 . To induce Rabi oscillation, the system should be kept coherently. Therefore, the decoherence time is an important parameter in our scheme. The typical decoherence time τ is about $1 \sim 5ps$ at room temperature [89]. To realize our sub-wavelength scheme, the requirements for these parameters are $t_{FWHM} \leq \tau$ and $K_{ST} \gg K_F \gg K_P$. For $t_{FWHM} \leq \tau$, the system keeps coherent. For $K_{ST} \gg K_F$, intersystem crossing from S_1 to T_1 dominates, which means that most of the

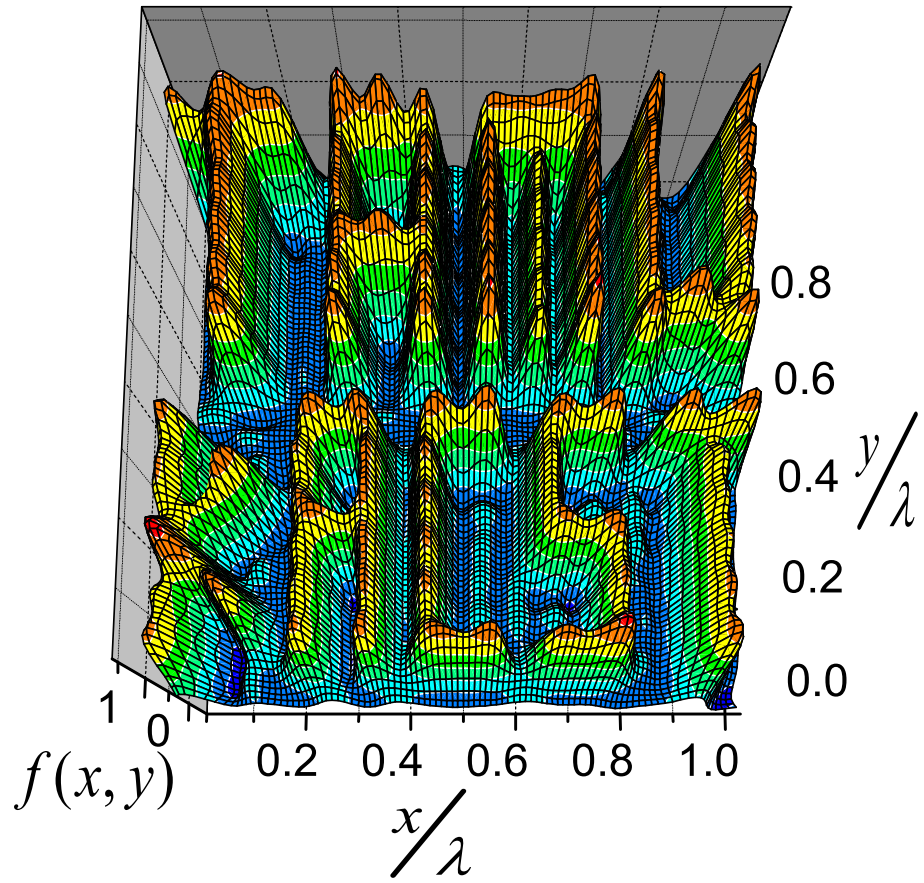


Figure 3.7: A 2D pattern "TAMU-KACST" printed within one wavelength using the present method. Parameters are $M = N = 15$, $\theta = 80^\circ$.

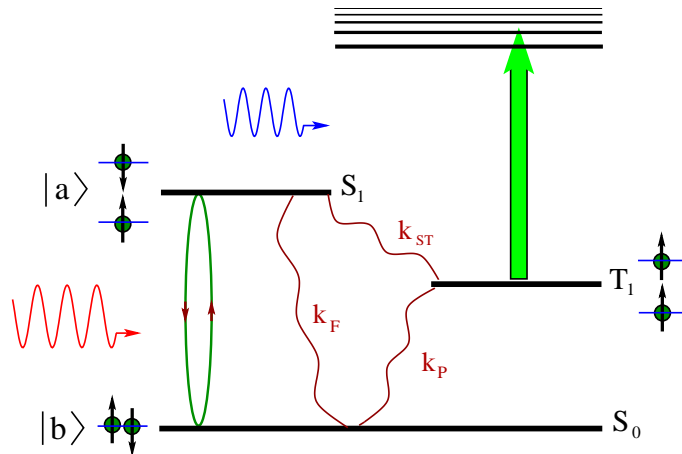
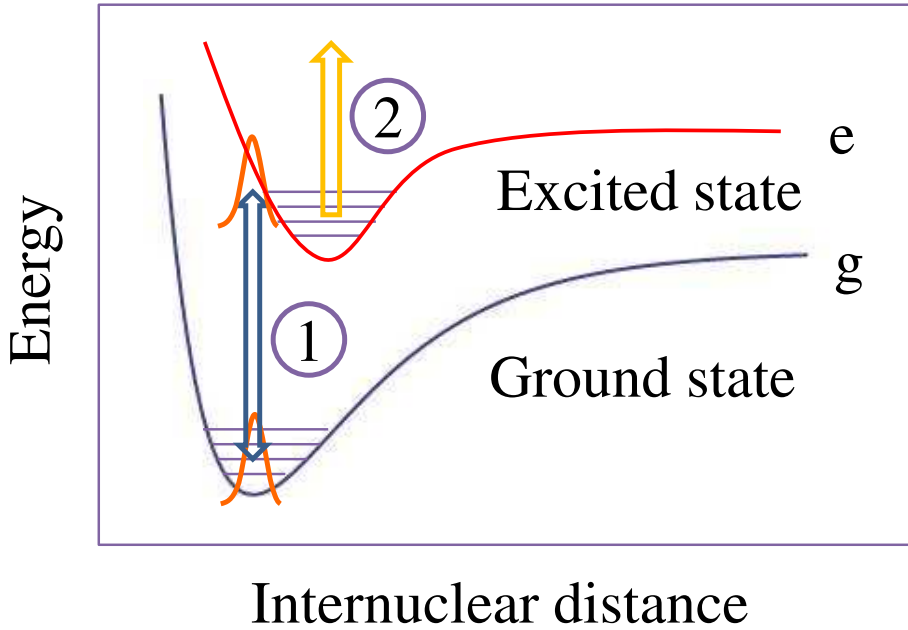


Figure 3.8: The schematics for the state energy diagram for molecular organic photochemistry.

molecules at S_1 will transfer to T_1 instead of decaying to S_0 . As the transition from T_1 to S_0 is spin forbidden, the life time (or phosphorescence time) of T_1 is long. Within the phosphorescence time, we shine the second pulse to dissociate the molecules in state T_1 . Indeed, the requirements can be satisfied in some real systems. Usually, the time scale for K_F : $10^5 \sim 10^9$ Hz; K_{ST} : $10^5 \sim 10^{11}$ Hz; K_P : $10^{-2} \sim 10^3$ Hz. The Rabi frequency can be chosen as 10^{12} to 10^{14} Hz. One example is 1-Bromonaphthalene [85] for which $K_F \sim 10^6$ Hz, $K_{ST} \sim 10^9$ Hz, $K_P \sim 30$ Hz. The life time of the intermediate state T_1 is about 30 ms which is long enough for us to shine the second pulse.

It is worthwhile to mention that the dipole-dipole interaction or exchange interaction may induce energy transfer between neighboring molecules which limits the resolution in our scheme [85]. However these effects can be ignored for the following reasons. The dipole-dipole energy transfer rate is of the order of fluorescence rate when the distance between two molecules is in the range of $1 - 5\text{nm}$. However, as we require K_{ST} to be much larger than K_F , the intersystem crossing to T_1 occurs in times shorter than that required for the dipole-dipole energy transfer to the neighboring molecules. Also when the molecules are in the triplet state the dipole-dipole energy transfer between the two molecules is forbidden. Therefore the energy transfer due to the dipole-dipole interaction can be ignored in our scheme. While the triplet-triplet energy transfer is allowed by the electron exchange interaction, it can only happen at a distance within 1nm which is about the size of the molecules. Usually we cannot reach such small patterns in the photoresist lithography.

The second possible realization is to generate a nanopattern using a microwave. For example, the solid state system such as the NV-diamond has a long decoherence time. The ground triplet state is split into two sublevels ($m_s = 0$ and $m_s = \pm 1$). The energy difference between these two sublevels are about 2.9GHz , which corresponds



Internuclear distance

Figure 3.9: Typical energy potential surface of a molecule. The first pulse is used to inducing coherent Rabi oscillations between two energy potential surfaces, while the second pulse is used to dissociate the molecules in the excited state.

to a microwave with wavelength of about $0.1m$. The decoherence time at room temperature can reach $1.8ms$ [90]. Let $t_{FWHM} = 1ms$ and $\Omega_R = 0.1GHZ$, then we can reach a resolution of about $300nm$. At the low temperature, the decoherence time can be even larger, and the pattern can be smaller.

3.3 Sub-diffraction-limit pattern generation in molecular system via coherent Rabi oscillations

3.3.1 Theoretical model

In the Born-Oppenheimer approximation, the molecular energy level can be described by the well-known Morse potential energy curve (Fig. 3.9). Here we only

consider two energy levels: the ground state potential surface ($U_g(R)$) and excited state potential surface ($U_e(R)$). We can neglect other potential surfaces if they are far away from these two potential energy curves near the equilibrium position R_0 of the ground state, i.e., the energy gap at R_0 is much larger than the bandwidth of the ultrashort pulse and the Rabi frequency. The ground state potential function around the equilibrium position can be well approximated by a harmonic potential [91]:

$$U_g(R) = \frac{1}{2}m\omega^2(R - R_0)^2 \quad (3.17)$$

where m is the reduced mass of the molecule, ω is the fundamental vibrational frequency of the ground energy. We can simplify the excited state as a linear function of R [91]:

$$U_e(R) = -\alpha(R - R_0) + \beta \quad (3.18)$$

where α is the slope of the excited potential surface and β is the energy gap between the excited state and ground state at R_0 .

The wave packet dynamics for the molecule at position x are described by the coupled-channel Schrödinger equations [91]

$$i\hbar \frac{\partial}{\partial t} \Psi_g(x, R, t) = [-\frac{\hbar^2}{2m} \frac{\partial^2}{\partial R^2} + U_g(R)] \Psi_g(x, R, t) + V(x, t) \Psi_e(x, R, t), \quad (3.19)$$

$$i\hbar \frac{\partial}{\partial t} \Psi_e(x, R, t) = [-\frac{\hbar^2}{2m} \frac{\partial^2}{\partial R^2} + U_e(R)] \Psi_e(x, R, t) + V(x, t) \Psi_g(x, R, t). \quad (3.20)$$

where $\Psi_1(x, R, t)$ and $\Psi_2(x, R, t)$ are the corresponding wave packets in the ground state and the excited state, $V(x, t) = \vec{d} \cdot \vec{E}(x, t)$ is the coupling strength at position x where \vec{d} is the transition dipole moment between the ground state and the excited state.

At room temperature or below, most of the molecules are in the lowest vibrational

state of the ground potential surface. Therefore we can write the initial ($t \rightarrow -\infty$) wave packets in the ground state and the excited state as [91]

$$\Psi_1(x, R, -\infty) = (2\pi\sigma^2)^{-1/4} \exp\left[-\frac{(R - R_0)^2}{4\sigma^2}\right] \quad (3.21)$$

$$\Psi_2(x, R, -\infty) = 0 \quad (3.22)$$

where $\sigma = \sqrt{\hbar/2m\omega}$. From the initial wave-packets and the couple-channel Schrödinger equations, we can solve the dynamics of the wave packets. Analytical solution for the dynamics in Eq. (3.21) and Eq. (3.22) is not available. Numerical method is usually applied to solve these coupled equations. Here we use the split-operator Fourier transform technique to solve these equations [92, 91, 93]. For simplicity, the scaling factors for the length and time are chosen as [91, 94]

$$R_c = \sqrt{\frac{\hbar}{\sqrt{2}m\omega}}, t_c = \frac{\sqrt{2}}{\omega}. \quad (3.23)$$

In this scaling, the constant $\hbar, \hbar^2/2m$, and $m\omega^2$ become unity. The initial wave packet size is $\sigma = 2^{-1/4}$. α and β in Eq. (3.18) are dimensionless (their scale are $\hbar/t_c R_c$ and \hbar/t_c respectively). The unit for frequency or Rabi frequency is $1/t_c$.

3.3.2 Numerical simulation

3.3.2.1 Wave packet dynamics

In this section, we numerically solve the coupled-channel Schrödinger equations for different parameter settings. For different potential slopes ($\alpha = 0, 1, 5$), we calculate the wave packet dynamics for different Rabi frequency and pulse time.

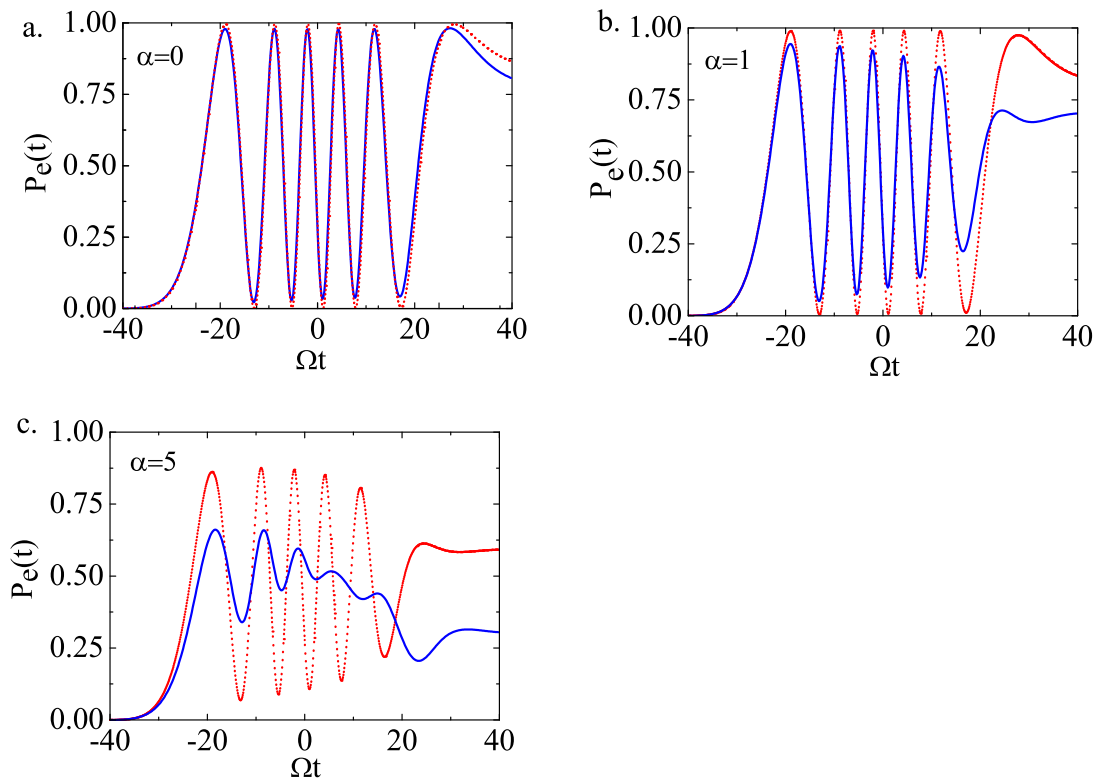


Figure 3.10: Dynamics of the population in the excited state as a function of time when the molecule is excited by a ultrashort pulse. The solid line is the result when $\Omega_0 = 20, t_p = 1$. The dotted line is the result when $\Omega_0 = 50, t_p = 0.4$. (a) $\alpha = 0$; (b) $\alpha = 1$; (c) $\alpha = 5$.

Here we consider the pulse is Gaussian and it is given by

$$\vec{E}(t) = \vec{e}\mathcal{E}_0 \exp\left(-\frac{t^2}{t_p^2}\right) \cos(\nu t) \quad (3.24)$$

where \vec{e} is the polarization direction, ν is the center frequency which is chosen to be resonant with the energy gap between the two potential surfaces at the equilibrium position. The full width half maximum of field intensity is given by $t_{FWHM} = \sqrt{2 \ln 2} t_p$. The Rabi frequency is then given by

$$\Omega_R(t) = \Omega_0 \exp\left[-\frac{t^2}{t_p^2}\right] \quad (3.25)$$

where $\Omega_0 = (\vec{d} \cdot \vec{e})\mathcal{E}_0/\hbar$ is the Rabi frequency at the peak intensity. The integrated pulse area is

$$\theta = \int_{-\infty}^{\infty} \Omega_R(t) dt = \sqrt{\pi} \Omega_0 t_p. \quad (3.26)$$

The number of oscillations is given by $\theta/2\pi$. We can see that larger Rabi frequency or longer pulse time can induce more oscillations.

Figure 3.10(a) is the result for $\alpha = 0$ which is the case that the equilibrium position of the excited potential surface is the same as that of the ground potential surface [95]. The solid line is the result for $\Omega_0 = 20$ and $t_p = 1$, while the dotted line is the result for $\Omega_0 = 50$ and $t_p = 0.4$. The pulse area for both case is $20\sqrt{\pi}$. The number of oscillations is expected to be the same and it is given by $20\sqrt{\pi}/2\pi$ which is about 5.6. The number of oscillations for the numerical result shown in Fig. 2(a) is consistent with the theoretical evaluation. The visibility of the oscillations is almost 1 and the visibility for the shorter pulse time and higher Rabi frequency is slightly higher.

Figure 3.10(b) is the result for $\alpha = 1$ which is the case that the equilibrium

position of the excited state deviates from R_0 by a small amount. We can see that the visibility decreases by some amounts as time goes for the case that $\Omega_0 = 20$ and $t_p = 1$. The reason is that the wave packet can slide down the potential hill and leave the resonant region. If we use stronger and shorter pulse ($\Omega_0 = 50$ and $t_p = 0.4$), we can see that the visibility increase significantly because the wave packet has no enough time to move away.

Figure 3.10(c) is the result for $\alpha = 5$ which is the case that equilibrium position of the excited state deviates from R_0 by a larger amount. We can see that when $\Omega_0 = 20$ and $t_p = 1$ the amplitude of the oscillations decreases significantly and curve is distorted at the end of the pulse which indicates that the wave packed is significantly dispersed. We can recover the oscillation pattern by using stronger and shorter pulse ($\Omega_0 = 50$ and $t_p = 0.4$). However the visibility is still much less than 1.

From these three examples, we can clearly see that the smaller the α , the better the oscillations. We also notice that number of oscillations is determined by the pulse area but stronger and shorter pulse can increase the visibility of the oscillations.

3.3.2.2 Subdiffraction-limited pattern generation

In this subsection we study the spatial distribution of the population at the excited state when the molecules interact coherently with a strong diffraction-limited ultrashort pulse.

Here the pulse is assumed to be Gaussian in both the time domain and the space domain:

$$\vec{E}(x, t) = \vec{E}(t) \exp\left[-\frac{x^2}{2\sigma_x^2}\right] \quad (3.27)$$

where $\vec{E}(t)$ the electric field profile in the time domain which is given by Eq. (3.24). For a diffraction-limited beam, the full width half maximum of the spatial intensity distribution is about $\lambda/2$ which corresponds to $\sigma_x = \lambda/(4 \ln 2)$. Supposing that the

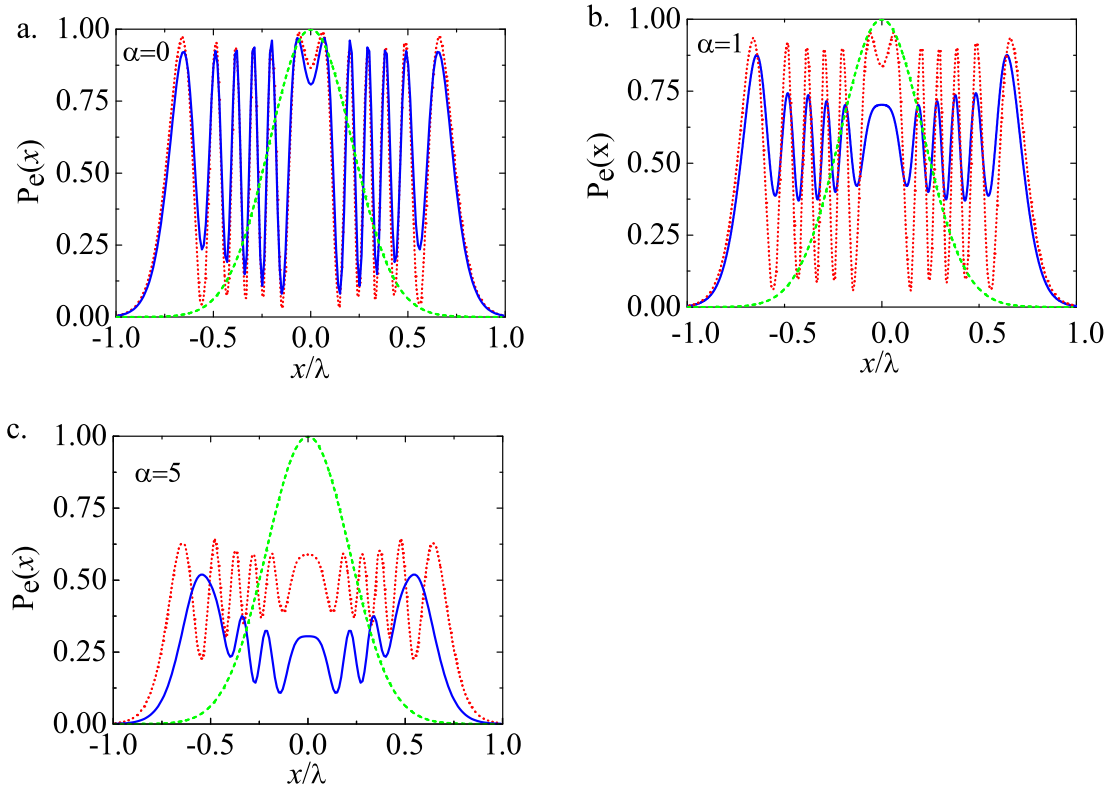


Figure 3.11: Subdiffraction-limited pattern generation when the molecule is excited by a diffraction-limited beam. The dashed line is the intensity profile of the diffraction-limited excitation beam. The solid line is the pattern generated by the pulse with $\Omega_0 = 20, t_p = 1$. The dotted line is the result when $\Omega_0 = 50, t_p = 0.4$. (a) $\alpha = 0$; (b) $\alpha = 1$; (c) $\alpha = 5$.

molecules have identical transition dipole moments, the maximum Rabi frequencies at different positions are given by

$$\Omega_R(x) = \Omega_0 \exp\left[-\frac{x^2}{2\sigma_x^2}\right]. \quad (3.28)$$

Different positions have different Rabi frequencies which leads to the spatial modulations of the excited populations.

Similar to previous subsection, we numerically calculate the spatial patterns generated by the ultrashort Gaussian pulse for three potential surfaces: $\alpha = 0, \alpha = 1$, and $\alpha = 5$. Comparing these three figures, we find the following features: a) subdiffraction-limited patterns are generated in all three potential surfaces. The minimum spacing is about $\lambda/11$ which is much less than the diffraction limit. The resolution of the pattern generated by $\alpha = 5, \Omega_0 = 20$, and $t_p = 1$ is lower than others because the wave packet has been significantly dispersed. b) For the same parameters, the smaller the α the better the visibility. This indicates that a good candidate for the photoresist should have two potential surfaces with close equilibrium positions. c) For each α , visibility is higher when using larger Rabi frequency and shorter pulse time. d) the pattern is narrower at the positions that the gradient of the electric field is larger.

3.3.3 Pulse techniques to improve visibility

In the previous section we have shown that subdiffraction-limited pattern can be generated in molecular system using ultrashort pulses. However, when potential surface has a larger slope that the wave packet can be easily dispersed the visibility is not good, e.g., when $\alpha = 5$ (Fig. 3.10(c) and Fig. 3.11(c)). In this section we discuss two possible techniques to improve the visibility. One is using multi-pulse train instead of one Gaussian pulse to reduce the effective interaction time. The

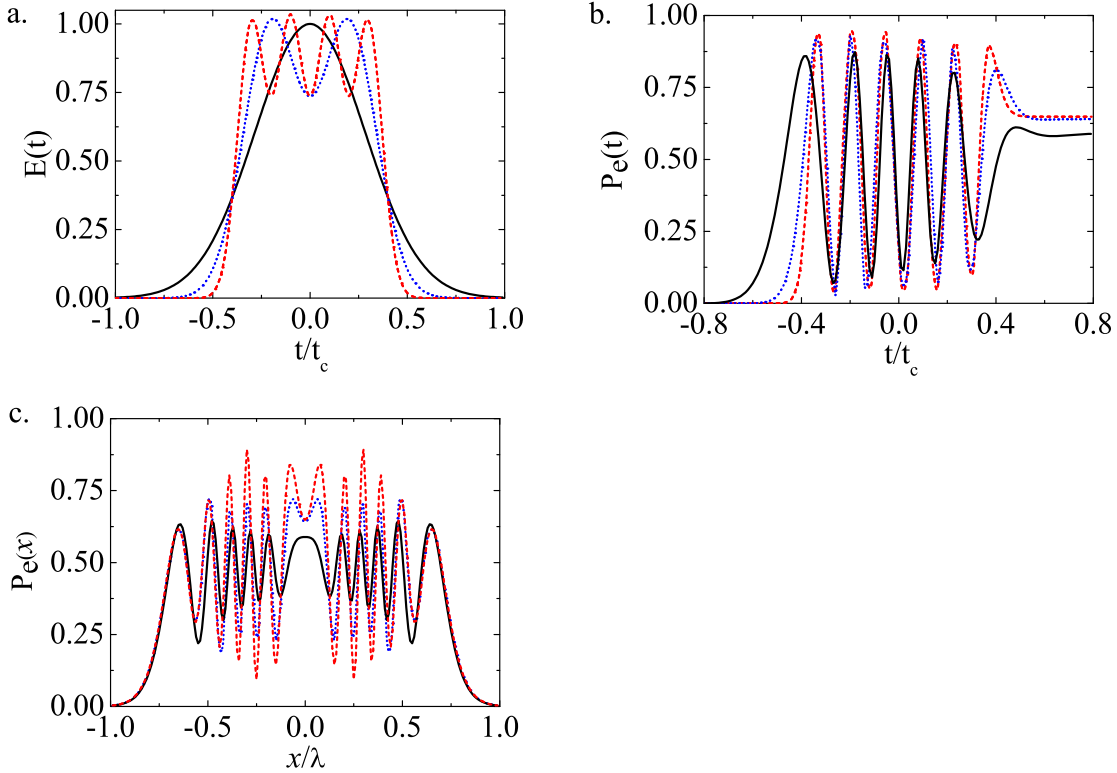


Figure 3.12: (a) Electric field envelopes for one, two, and four-pulse train. (b) Wave packet dynamics excited by one, two, and four-pulse train. (c) Subdiffraction-limited pattern generated by one, two, and four-pulse train excitation. The solid line is for one pulse case with $\Omega_0 = 50$ and $t_p = 0.4$. The dotted line is for two-pulse train with $\Omega_0 = 50$, $t'_p = 0.2$, and $\tau = 0.4$. The dashed line is for four-pulse train with $\Omega_0 = 50$, $t'_p = 0.1$, $\tau_1 = 0.2$, $\tau_2 = 0.4$, and $\tau_3 = 0.6$.

other is using chirped pulse technique to compensate the wave packet dispersion.

3.3.3.1 Multi-pulse train technique

In practice we can engineer the pulse shape to increase the visibility of the Rabi oscillations. For example, we can generate the following multi-pulse train

$$\vec{E}(t) = \vec{e}\mathcal{E}_0 \sum_{n=1}^N \exp\left[-\frac{(t - \tau_n)^2}{t'^2_p}\right] \cos(\nu t). \quad (3.29)$$

with $t'_p = t_p/N$ (N is the number of pulses) and τ_n is the positions of the pulses. We can readily verify that this pulse train has the same peak intensity and the integrated pulse area as the one Gaussian pulse shown in Eq. (3.24). Therefore they should generate patterns with similar resolution. However, the multi-pulse train is more compact in time than one pulse case (Fig. 3.12(a)). Thus the wave packet has less time to move away in the multi-pulse train case and it can in principle generate a pattern with higher visibility.

In Figure 3.12(b), we compare the wave packet dynamics for one, two and four-pulse cases when $\alpha = 5$, $\Omega_0 = 50$, and $t_p = 0.4$. We can see that they have similar oscillation pattern but the amplitude of oscillations is largest in four-pulse train excitation and is smallest in one pulse excitation. In Fig. 3.12(c) we also find that the visibility of the subdiffraction-limited pattern increases as the number of the pulse train increases, while the resolution does not change. These examples shows that multi-pulse train works better than one-pulse case.

3.3.3.2 Chirped pulse technique

The wave packet can significantly move down the slope of the potential surface when α is large. Thus the resonant frequency becomes smaller as time goes. One possible way to compensate this effect is using chirped pulse. The linearly chirped pulse is given by [96]

$$\vec{E}(t) = \vec{e}\mathcal{E}_0 \exp\left(-\frac{t^2}{t_p^2}\right) \cos(\nu t + a\frac{t^2}{t_p^2}) \quad (3.30)$$

where ν is the central frequency and a is dimensionless chirped parameter. We can see that different frequency component comes at different time. One example is shown in Fig. 3.13(a) where higher frequency comes earlier and lower frequency comes latter which may compensate the wave packet dispersion effect.

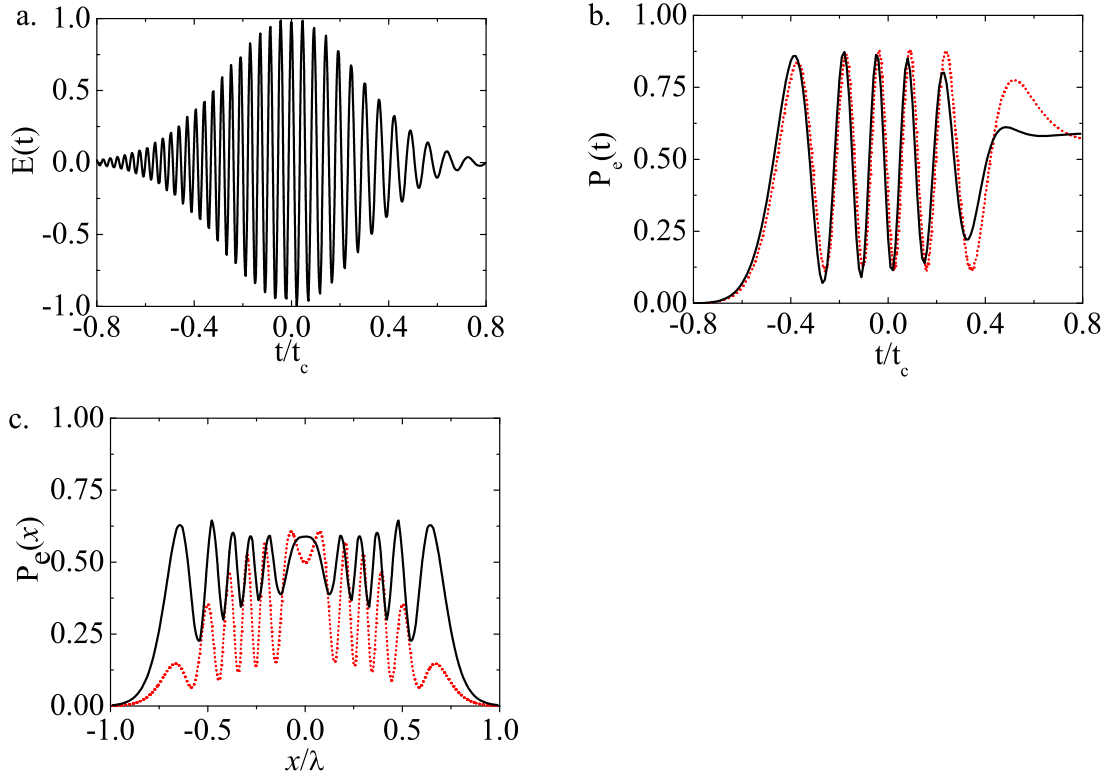


Figure 3.13: (a) Example of a linearly chirped pulse. (b) Dynamics of the population in the excited state as a function of time when the molecule is excited by an unchirped and chirped pulse. (b) Subdiffraction-limited pattern generated by an unchirped and chirped pulse. The solid line is the result for unchirped pulse while the dotted line is the result for chirped pulse. Parameters: $\alpha = 5$, $\Omega_0 = 50$, $t_p = 0.4$.

The wave packet dynamics excited by a linearly chirped pulse is shown in Fig. 5b. Here we use the example that $\alpha = 5$. The resonant frequency in the equilibrium position is assumed to be $\omega_0 = 500$. The center frequency of the chirped pulse ν is chosen to be 492 which is slightly less than ω_0 , the chirped parameter $\alpha = -1.6$, and $t_p = 0.4$. The peak Rabi frequency is chosen to be 50. From the figure we see that the amplitude of the Rabi oscillations at the end of the pulse increases comparing with the unchirped case. Figure 5c is the spatial pattern generated by the chirped and unchirped pulse. We can see that in the center region the visibility of the pattern generated by the chirped pulse is higher, while it is lower at the edge of the field. The reason is that the field strength is very small at the edge of the field and the excitation is very small. The wave packet is mainly in the equilibrium positions of the ground potential. The resonant frequency is about ω_0 within the pulse time while the excitation frequency is less than ω_0 for most of the time. Thus the chirped technique can help when the excitation is high.

4. ATOM LITHOGRAPHY BEYOND THE DIFFRACTION LIMIT VIA COHERENT RABI OSCILLATIONS*

We propose two atom lithography experiments with sub-wavelength resolution based on the method we proposed in the previous chapter. One is using Rubidium Rydberg atoms and microwave with centimeter wavelength, where we numerically showed that a line spacing of the order of micrometers is possible. The other is using Chromium atom and visible light with wavelength about 400nm, where we numerically showed that sub-10nm spacing in both one and two dimensional space is possible.

4.1 Atom lithography

Atom lithography has been proposed to write lines with sub-100 nm width because the deBroglie wavelength of the atom is very small (usually less than 0.1nm) [97, 98, 99, 100, 101]. The typical schematic setup of atom lithography is shown in Fig. 4.1(a) [102]. The atoms ejected from an aperture are collimated by the laser cooling. After passing through the beam mask the atoms interact with a standing wave. The frequency of the standing wave is slightly detuned from the atomic transition frequency. When the atoms pass through the standing wave, they feel an optical dipole potential which is given by

$$U(x) = \frac{\hbar\Delta}{2} \ln\left[1 + \frac{I(x)}{I_0} \frac{\Gamma^2}{\Gamma^2 + 4\Delta^2}\right] \quad (4.1)$$

*Reprinted with permission from Atomic Lithography with Subwavelength Resolution via Rabi Oscillations by Z. Liao and M. Al-Amri and T. Becker and W. P. Schleich and M. O. Scully and M. S. Zubairy, 2013. Phys. Rev. A, vol. 87, pp. 023405, and from Coherent Atom Lithography with Nanometer Spacing by Z. Liao and M. Al-Amri and M. S. Zubairy, 2013. Phys. Rev. A, vol. 88, pp. 053809, Copyright [2013] by the American Physical Society.

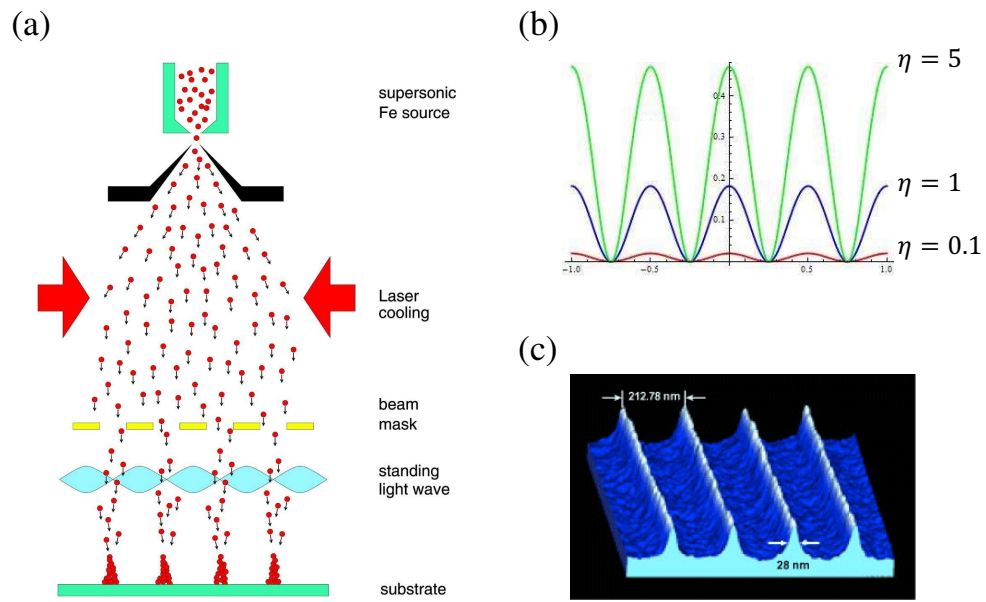


Figure 4.1: (a) Typical setup of atom lithography. (b) Optical dipole potentials for different laser intensities where $\eta = I_{max}/I_0$. (c) A pattern written by the atom lithography. Figure (a) reprinted with permission from (te Sligte et al., 2003). Copyright 2003 by Elsevier. Figure (c) reprinted with permission from (McClelland et al., 1993). Copyright 1993 by AAAS.

where Δ is the detuning, Γ is the atomic line width, $I(x)$ is the laser intensity at position x , and I_0 is the saturation intensity. Since $U(x)$ nonlinearly depends on the laser intensity $I(x)$, the atoms can be trapped into very narrow region if $I(x)$ is large compared to I_0 (Fig. 4.1(b)). If $I(x)$ increase, the dipole trap can becomes narrower. However, the period of the dipole trap is still half wavelength of the standing wave. This method does not overcome the diffraction limit in terms of line spacing [97, 98, 99, 100, 101, 103]. One experimental demonstration is shown in Fig. 4.1(c) where we can see that the width of a line is about 28nm, but the line spacing is about 213nm [98].

In the following, I will illustrate two atom lithography schemes based on our coherent Rabi oscillations method, which can achieve line spacing beyond the diffraction limit.

4.2 Atom lithography with sub-wavelength line spacing using microwave

In this section, we present a sub-wavelength atom lithography schemes to implement the method based on Rabi oscillations. Instead of shining spatially distributed light on atoms, we propose to pass atoms through a standing wave. We discuss a spatially uniform beam of Rydberg atoms moving with a constant velocity undergoing spatially dependent Rabi oscillations. In our proposed implementation of sub-wavelength lithography, we chose Rydberg atoms for three reasons [104, 105, 106]. (i) Our scheme requires the system to have a relatively long coherence time and Rydberg atoms satisfy this requirement rather well. (ii) The transition dipole moment of Rydberg atoms is extremely large which is conducive for inducing Rabi oscillations. (iii) State-selective field ionization techniques can be applied to detect the population in different states [107, 108]. One drawback of Rydberg atoms is its relatively large size which can be of the order of hundreds of nanometers. and which would

limit the resolution we can achieve in this scheme. Nevertheless it is still one of the best testbeds for this proof-of-principle experiment.

4.2.1 Basic principle

In last Chapter we have presented a simple method to achieve sub-wavelength patterns by inducing Rabi oscillations between two atomic levels. Here, we briefly recall this scheme in order to lay the foundations for the next sections. When two-level atoms interact with a laser light, or a microwave whose frequency is resonant with that of the transition, the probabilities of the atom to be in the excited and the ground states $|a\rangle$ and $|b\rangle$, respectively, are given by

$$P_b(x) = \frac{1}{2}\{1 + \cos[\theta(x)]\}, P_a(x) = \frac{1}{2}\{1 - \cos[\theta(x)]\}. \quad (4.2)$$

where $\theta(x) = \int_0^T \Omega(x, t)dt$ is the pulse area. T is the interaction time which should be less than the population decay time of the atoms and $\Omega(x, t)$ is the Rabi frequency at the position x and the time t . The Rabi frequency is given by $|\vec{\phi}| \mathcal{E}(x, t)/\hbar$, where $|\vec{\phi}|$ is the transition dipole moment between the atomic levels, $\mathcal{E}(x, t)$ is the field amplitude at the position x and the time t . Hence if the field is spatially dependent, the probability in each state is also spatially dependent.

For the first example, let's consider a simple case that the electric field is a linear function of the coordinate x and constant in time such as $\mathcal{E}(x) = \mathcal{E}_0 x/\lambda$. The position-dependent Rabi frequency reads $\Omega(x) = \Omega_0 x/\lambda$ where $\Omega_0 \equiv |\vec{\phi}| \mathcal{E}_0/\hbar$. The probability to be in the excited state is given by

$$P_e(x) = \frac{1}{2}(1 - \cos[\Omega_0 T x/\lambda]) \quad (4.3)$$

and the period λ_{eff} of the pattern is

$$\lambda_{eff} = \frac{\lambda}{\Omega_0 T / 2\pi}. \quad (4.4)$$

If $\Omega_0 T > 2\pi$, the resolution of the pattern is sub-wavelength. For a larger pulse area $\Omega_0 T$ we obtain a smaller spacing of the features and we can increase the resolution by just increasing the field strength or the interaction time.

The second example is related to this experimental setup where we consider the electric field in the cavity is TM_{210} mode. The electric field of this mode has polarization along z direction and is given by

$$E_z(x, y, z) = \mathcal{E}_0 \sin\left(\frac{2\pi x}{a}\right) \sin\left(\frac{\pi y}{b}\right) \quad (4.5)$$

where a and b are the width and length of the cavity, respectively. The Rabi frequency felt by the atoms is then given by

$$\Omega(x, t) = \Omega_0 \sin\left(\frac{2\pi x}{a}\right) \sin\left(\frac{\pi v_{||} t}{b}\right) \quad (4.6)$$

where we have used the relation $y(t) = v_{||}t$ and $v_{||}$ is the longitudinal velocity of the atoms. Around the center of the cavity the electric field is approximately linear and the integrated pulse area is given by

$$A(x) = \Omega_0 \frac{4bx}{av_{||}}. \quad (4.7)$$

From this equation one can see that $k_{eff} = 4b\Omega_0/av_{||}$ and the corresponding period is

$$\lambda_{eff} = \frac{\pi av_{||}}{2\Omega_0 b}. \quad (4.8)$$

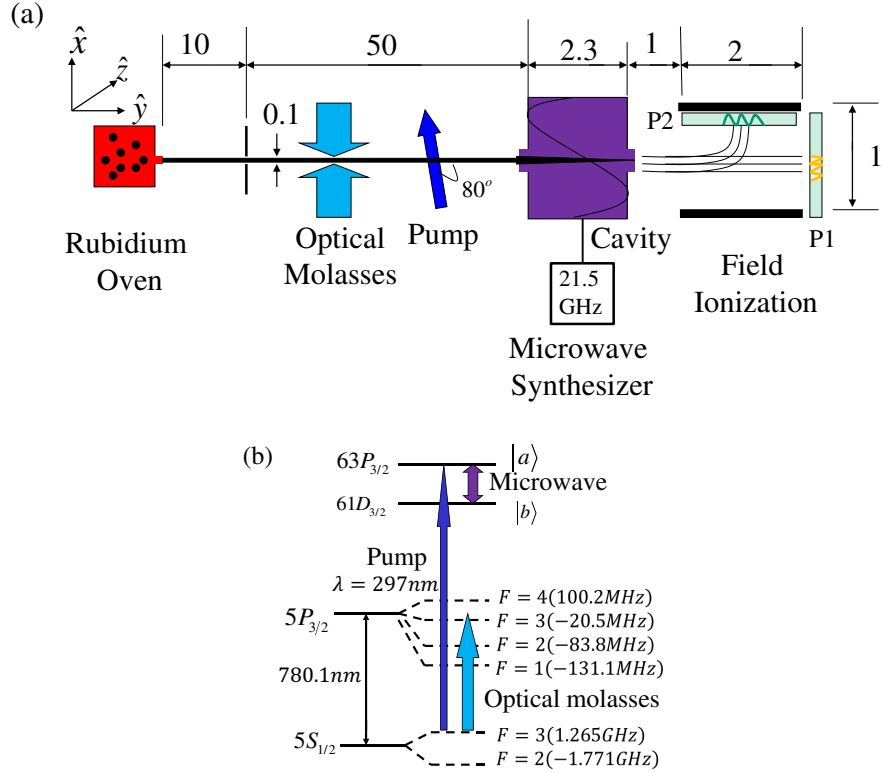


Figure 4.2: (a) Proposed experimental setup for the sub-wavelength atom lithography using position-dependent Rabi oscillations of Rydberg atoms (unit for the dimension is cm). P1 is photoresist used for neutral atom lithography while P2 is the photoresist used for ionized atom lithography. (b) Energy diagram of the Rb-85 atom.

We can see that the larger the Rabi frequency, the smaller the effective period.

4.2.2 Proposed experimental setup

The proposed experimental setup and the relevant Rb-85 atomic levels are shown in Fig. 4.2(a) and (b), respectively. Rubidium atoms are ejected from a small aperture of 1mm size on the oven. At room temperature the root-mean-square velocity is around 300m/s. Since atomic collimation is indispensable in this experiment we propose to use optical molasses which will not reduce the atomic flux significantly. The capture velocity for Rb atom is $v_c = \gamma/k \approx 4.5m/s$. Here $\gamma = 2\pi \times 6MHz$ is

the natural width of $5P_{3/2}$ state and k is the wavevector of the cooling laser with a wavelength of about 780nm [109]. The atoms are precollimated by a slit with 1mm aperture located 10cm away from the oven. The root-mean-square transverse velocity after the slit is about 3m/s which is within the range of the capture velocity. A standing wave of circularly polarized laser light where the frequency is red detuned to the $5S_{1/2}, F = 3 \rightarrow 5P_{3/2}, F = 4$ transition is used to collimate the Rb atoms. The optimal damping of the velocity occurs on a time scale $\tau_c = 2M/\hbar k^2 (\approx 42\mu\text{s}$ for Rb-85 atom, where M is the mass of the atom) [109]. Therefore, the longitudinal extension of the optical molasses should be about 2cm to effectively collimate the Rb atoms and the excited atoms can decay to the $5S_{1/2}, F = 3$ state. The Doppler limit for the transverse velocity collimation is about 0.1m/s . However, a collimation below the Doppler limit can be achieved by polarization gradients [110, 109].

The interaction time between the atoms and the microwave is required to be identical for all atoms. To achieve this goal we propose to selectively excite them from the state $5S_{1/2}, F = 3$ to the Rydberg state $63P_{3/2}$ with a small range of longitudinal velocity by Doppler effect [108]. The angle θ between the 297nm pumping laser and the atomic beam is set to be 80° . The pumping laser is a continuous laser which can be produced by frequency doubling the light from a rhodamine 6G dye laser (Coherent 899 ring laser) in a separate enhancement cavity with a beta-barium-borate crystal [108]. We can use an acoustic optical modulator to slightly shift the frequency of the pumping laser such that only the atoms with longitudinal velocity around 300m/s can be excited according to the Doppler effect. The velocities of the excited atoms have a small uncertainty $\Delta v_{\parallel} = (\Delta\nu/\nu)(c/\cos\theta)$ due to the bandwidth of the pumping laser. In the neutral atom lithography the linewidth of the pumping laser should be stabilized to be about 1MHz , then the uncertainty of the longitudinal velocity Δv_{\parallel} is about 1.48m/s . While in the ionized atom lithography, the linewidth

of the pumping laser should be stabilized to be about 10KHz to achieve sub-micron resolution. In this case the uncertainty of the longitudinal velocity is about 1.48cm/s .

The Rb atoms then fly through a microwave cavity with size $a \times b \times c$ with $a = 1.05\lambda$, $b = 1.64\lambda$, $c = 0.4\lambda$ and $\lambda = 1.4\text{cm}$. The cavity can support many modes but only the TM_{210} mode has frequency resonant with the transition frequency between $63P_{3/2}$ and $61D_{3/2}$ which is about 21.5GHz . The cavity can be driven by an external synthesizer whose frequency is 21.5GHz and it can enhance the TM_{210} mode. Only the atoms which are pumped to $63P_{3/2}$ will interact with the microwave field. The atom-field coupling constant (one photon Rabi frequency) is $\Omega = 10\text{kHz/photon}$ [104, 105]. The interaction time is $b/v_{||}$ which is about $76.5\mu\text{s}$. The decay time from $63P_{3/2}$ can be tens of milliseconds which is sufficient for this experiment. Because the microwave field strength has a linear gradient around the center of the cavity, the Rabi frequency felt by the Rb atom also has a linear gradient and the probabilities to be in one of the two Rydberg states are spatially modulated. According to the discussion in Sec. II, the spatial distribution of the atoms in the state $63P_{3/2}$ (or $61D_{3/2}$) can be sub-wavelength, which can be detected by a state-selective field ionization technique [107, 108].

Two metallic plates are separated by about 1cm and the voltage between them is $20V$. The electric field strength is just enough to ionize the atoms in the state $63P_{3/2}$ but not those in $61D_{3/2}$. The atoms which are ionized by this field feel a strong electromagnetic force and are deflected to one metallic plate and then hit a photoresist on the substrate. The atoms in the state $61D_{3/2}$ and those atoms in the ground state will not change their trajectories. They will also hit the photoresist on another substrate. We can choose a photoresist which works in the ultraviolet region such as diazonaphthoquinone (DNQ). The atoms in the state $61D_{3/2}$ will transfer their internal energy (about 4eV) to the photoresist and change its chemical property.

In contrast, the atoms in the ground state do not influence the photoresist. The substrate is then etched by some chemical substances and a sub-wavelength pattern will emerge which we can then verify in an optical microscope.

4.2.3 Numerical simulation

We now present a numerical simulation of our proposed experiment. Here, we assume that 2×10^5 Rb atoms are randomly ejected from the aperture with positions and transverse velocity in the range of $-0.5mm \leq x \leq 0.5mm$ and $-0.1m/s \leq v_\perp \leq 0.1m/s$, respectively. Moreover, the electric field strength inside the cavity is allowed to fluctuate by $\pm 1\%$. For different values of Ω_0 we calculate the counts of atoms in $|a\rangle$ state in the ionized atom lithography, while calculate the counts of atoms in $|b\rangle$ state in the neutral atom lithography. Because the size of the Rb ion is about $0.2nm$ which is much smaller than the photoresist molecules (about $5nm$), while the size of Rydberg Rb atom at $n = 61$ is about $200nm$, the pixel size for ion lithography is chosen to be $5nm$ and the pixel size for neutral atom lithography is $200nm$.

4.2.3.1 Neutral atom lithography

In the first simulation, the Rabi frequency Ω_0 is set to be $2\pi \times 500KHz$. According to Eq. (4.9), the period of the pattern should be about $96\mu m$. The numerical simulation result shown in Fig. 4.3(a) displays a period of about $100\mu m$ which matches the theoretical evaluation very well and demonstrates that we can use a microwave of $1.4cm$ to print a pattern with $100\mu m$ resolution which is about $1/140$ of the wavelength.

In the second simulation, we increase the Rabi frequency Ω_0 to be about $2\pi \times 1MHz$. The Rabi frequency here is 2 times of that of the first simulation. Hence, the period in this case should be 2 times smaller. Indeed, the simulation shown in Fig. 4.3(b) displays a period of about $50\mu m$ which is $1/2$ of the resolution of the

first case and about $1/280$ of the wavelength.

Due to the divergence of the transverse velocity ($0.1m/s$), the resolution limit in the previous parameter setting is about $20\mu m$. To generate smaller patterns, we need to collimate the atoms better. If the transverse velocity would be about $1cm/s$, the resolution can reach several micrometers. Indeed, for the simulation with $\Omega_0 = 2\pi \times 5MHz$ shown in Fig. 4.3(c), the resolution is about $10\mu m$. Figure 4.3(d) is the result for a Rabi frequency $\Omega_0 = 2\pi \times 10MHz$ where the resolution is about $5\mu m$ ($\sim \lambda/2800$). Because of the limitation of the transverse velocity collimation and the size of Rydberg atom, it is difficult to obtain a resolution better than $1\mu m$ in this scheme.

Two advantages of this scheme stand out: (i) The energy of the neutral atoms cannot ionize the resist material and the secondary electron scattering will not be a problem. (ii) The neutral atoms do not interact with each other. The disadvantage is that its resolution is limited due to the size of the Rydberg atom.

4.2.3.2 Ionized Atom Lithography

Our second method to do lithography with this experimental setup relies on the ionized Rb atom. Because in this version we need to project the x -positions of the atoms to y -positions, smaller longitudinal velocity uncertainties $\Delta v_{||}$ are required. To obtain a smaller $\Delta v_{||}$, the pumping laser should be stabilized and have a smaller bandwidth. For example, if $\Delta\nu = 10KHz$, then $\Delta v_{||} = 1.48cm/s$. For this small longitudinal uncertainty we assume that all the atoms are ionized at the same point. The acceleration of the Rb ion is $a = eE/M$. We calculate y -positions of the ions based on classical trajectories which yields

$$y = v_{||} \frac{-v_{\perp} + \sqrt{v_{\perp}^2 + a(d - 2x)}}{a} \quad (4.9)$$

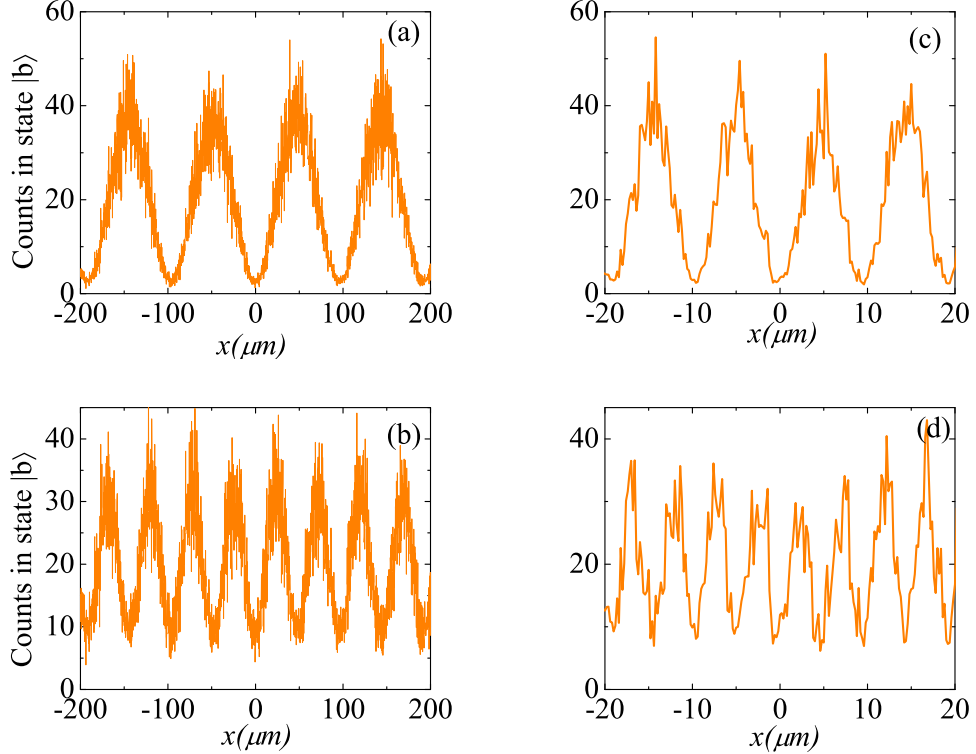


Figure 4.3: Simulation of neutral atom lithography with sub-wavelength resolution due to a position-dependent Rabi frequency represented by the spatial distribution of the $61D_{3/2}$ ($|b\rangle$) state for different Rabi frequencies Ω_0 . (a) $\Omega_0 = 2\pi \times 500KHz$; (b) $\Omega_0 = 2\pi \times 1.0MHz$; (c) $\Omega_0 = 2\pi \times 5MHz$; (d) $\Omega(x) = 2\pi \times 10MHz$. The transverse velocity uncertainty is $0.1m/s$ for (a) and (b), while is $0.01m/s$ for (c) and (d). The longitudinal uncertainty is fixed to be $1.48m/s$.

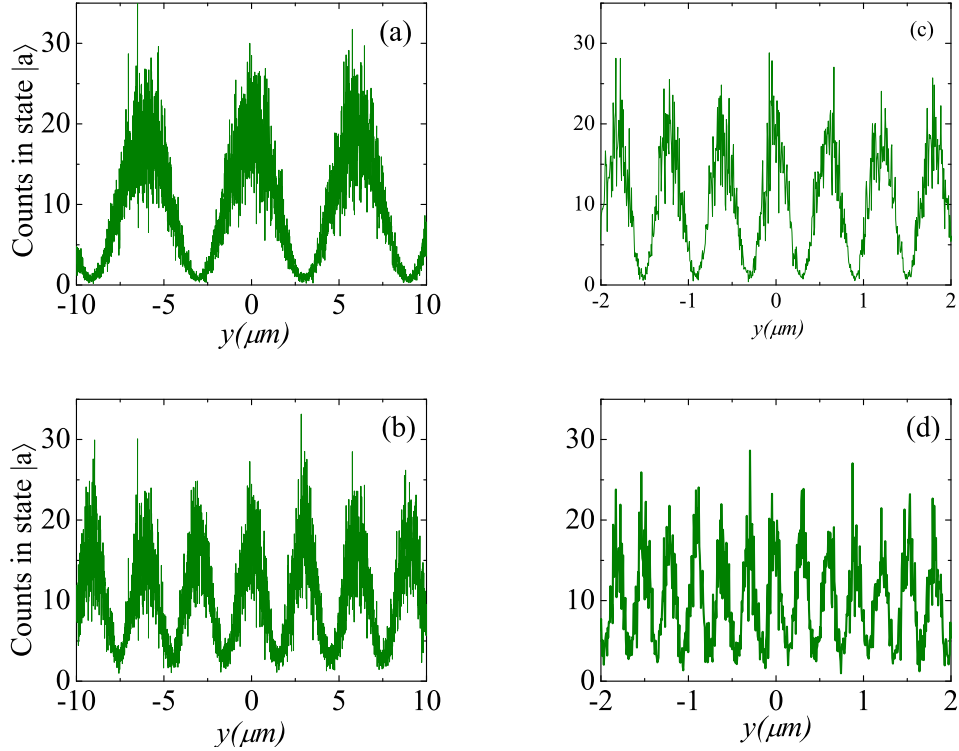


Figure 4.4: Simulation of ionized atom lithography with sub-wavelength resolution due to a position-dependent Rabi frequency represented by the spatial distribution of the $63P_{3/2}$ ($|a\rangle$) state for different Rabi frequencies Ω_0 . (a) $\Omega_0 = 2\pi \times 500KHz$; (b) $\Omega_0 = 2\pi \times 1.0MHz$; (c) $\Omega_0 = 2\pi \times 5MHz$; (d) $\Omega(x) = 2\pi \times 10MHz$. The transverse velocity uncertainty is $0.1m/s$ for (a) and (b), while is $0.01m/s$ for (c) and (d). The longitudinal uncertainty is fixed to be $1.48cm/s$.

where d ($= 1cm$) is the distance between two metallic plates. Since the acceleration is very large, we can estimate $y \sim -\frac{v_{||}}{\sqrt{ad}}x + const.$. When $E = 20V/cm$, the acceleration of the Rb ion is about $2.27 \times 10^9 m/s^2$ and we find that the x -scale is shrunk by a factor $v_{||}/\sqrt{ad}$ which is about $1/16$. Thus, for the same parameters as in neutral atom lithography, the ionized atom lithography has a resolution about 16 times higher.

We have performed four simulations for this scheme and the parameters are chosen to be identical to the ones of the neutral atom lithography except for the smaller

longitudinal velocity uncertainty needed here. The resolution in Fig. 4.4(a) is about $6\mu m$ which is about 1/16 of the resolution of Fig. 4.3(a). Similarly, the resolution in Figs. 4.4(b), 4.4(c), and 4.4(d) are $3\mu m$, $660nm$, $330nm$, respectively, which are also about 1/16 of the corresponding resolution in Figs. 4.3(b), 4.3(c), and 4.3(d).

There are some issues that need to be clarified: (i) the energy of the ionized atom may exceed the ionization energy of the resist material and secondary electrons may be ejected from the photoresist thus limiting the resolution to about $30nm$; (ii) the Coulomb force between ionized atoms may disturb the spatial distributions of the ionized atoms; and (iii) efficiency of this technique may be low because a low atomic beam intensity is required to avoid interactions between the ionized atoms.

The first issue is not a serious one for this experiment because we have not reached such a high resolution. For the second and the third one, we now perform some estimates to see whether they are serious or not. Assume that the atomic flux is about $10^{10}cm^{-2}s^{-1}$, the average distance between ions is about $0.1mm$. At this distance, the acceleration due to their coulomb force is of the order of $10^5m/s^2$. However, the acceleration due to the static electric field is of the order of $10^9m/s^2$ which is much larger. The displacement due the Coulomb force is on the order of $100nm$ in this experimental setup which is still smaller than the resolution we have generated. Therefore, all these concerns should not be problem at the proposed experiment. For sub-100 nm resolution, we just need to lower the atomic flux to about $10^8cm^{-2}s^{-1}$.

Because the Rb ions are much smaller than the Rydberg Rb atoms and the projectile motion here has also shrinking effect, this scheme can have better resolution. However, the ionization point and the trajectories of the ions should be much better controlled in this scheme. The exact dynamics of the field ionization is very complicated. Here we simply assume that all atoms have the same ionization point due

to the fact that the electric field around the middle line of the two electric plates is very uniform. Experimentally, the spatial dependence of the ionization field should be controlled with a precision on the order of $1\text{mV}/\text{cm}$.

4.3 Atom lithography with nanometer line spacing using visible light

In this section, I will show another atom lithography scheme where an optical field interacts with a beam of atoms. Different from the microwave, the recoil momentum of the photon in the optical regime can not be neglected. For our analysis, we consider a beam of chromium atoms interacting with an optical standing wave with $\lambda = 425.6\text{nm}$. We present a numerical analysis of the dynamics of the atomic wavepacket including the momentum recoil effect and show that sub- 10nm spacing is possible.

4.3.1 Proposed experimental setup

The proposed experimental setup is shown in Fig. 4.5. We propose to use chromium atom beam to do the lithography. The transition $^7S_3 \rightarrow ^7P_4$ at $\lambda = 425.6\text{nm}$ is involved for the collimation and inducing Rabi oscillations. The chromium atom beam is ejected from an oven and the mean longitudinal velocity is about 1000m/s . The transverse velocity of the atoms is first collimated to be about 5m/s by a slit with 1mm width and 20cm apart from the oven. The longitudinal velocity v_z is selected to be within the range of $1000\text{m/s} \pm 2.5\text{m/s}$ by a velocity selector. The transverse velocity of the atoms are further collimated by an optical molasses with lin \perp lin configuration [110, 111]. To generate the optical molasses, we slightly red tune the 425.6nm laser using an acoustic optical modulator. Then the width of the laser is expanded by two lenses to be about 20mm [111]. We can use a linear polarizer and a quarter wave plate to generate a lin \perp lin configuration optical molasses. This setup allows the atom beam to be cooled below the Doppler limit.

The collimated atomic beam is then passed through an optical standing wave with the frequency tuned to be exactly resonant to the $^7S_3 \rightarrow ^7P_4$ transition. In the longitudinal direction, we assume that the electric field is Gaussian and the field strength is given by

$$\vec{E}(x, z, t) = \vec{e}\mathcal{E}_0 e^{-z^2/w_0^2} \sin kx \cos \nu t. \quad (4.10)$$

where w_0 is the beam waist and \mathcal{E}_0 is the electric field amplitude at the center position. The laser intensity drops to about 1% of the peak intensity at $\pm 3w_0/2$ from the Gaussian beam center. Therefore, we can define the interaction region to be in the range of $-3w_0/2$ to $3w_0/2$. In the interaction region, the atoms undergo Rabi oscillations. The Rabi frequency can then be expressed as

$$\Omega_R(x, t) = \Omega_0 \exp\left[-\frac{(v_z t)^2}{w_0^2}\right] \sin kx \quad (4.11)$$

where we use the relation between z position and time which is given by $z = v_z t$ and $\Omega_0 = \mu \mathcal{E}_0 / \hbar$ is the peak Rabi frequency (μ is the transition dipole moment). Because the Rabi oscillation frequency is spatially modulated, the population in the excited state is also spatially modulated. After the standing wave, atoms impinge on the photoresist. The atoms in the excited state can transfer their internal energy to the photoresist molecules and change the chemical property of the photoresist. The atoms in the ground state do not change the photoresist. In this way the pattern generated in the photoresist depends on the spatial distribution of the atoms in the excited state.

This analysis is valid only if there is no recoil. This is a good approximation in the microwave region discussed in [61]. However, in the optical region, the atoms interacting with the standing wave can experience significant transverse recoil effect,

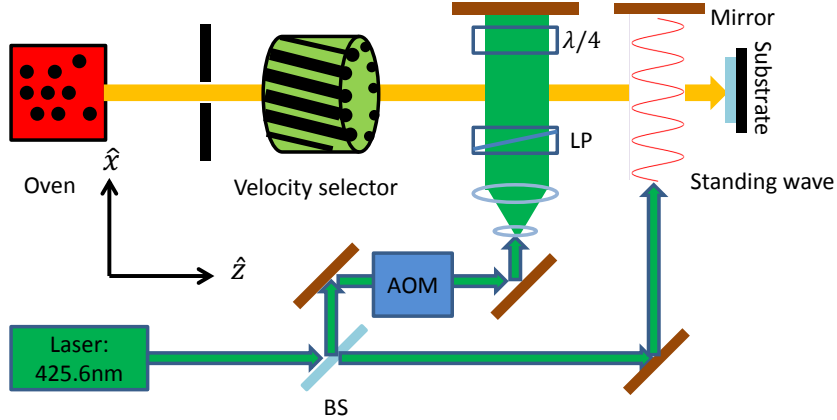


Figure 4.5: Proposed experimental setup for the sub-wavelength atom lithography using position-dependent Rabi oscillations. BS: beam splitter; AOM: acoustic optical modulator; LP: linear polarizer; $\lambda/4$: quarter wave plate.

thus adversely affecting the spatial distribution of the atoms on the photoresist.

In the following section, we calculate the spatial distribution of the atoms in the excited state after including the transverse degree of freedom in our equation of motion. Our goal is to see, under what conditions, nano-patterns can be written on the photoresist.

4.3.2 Theory and numerical method

In this section, we consider the interaction of the beam of atoms propagating in the z-direction with a standing field in the x-direction. The Hamiltonian of this system in the rotating wave approximation is given by [112]

$$H(x, t) = \frac{P_x^2}{2M} + \frac{1}{2}\hbar\Omega(x, t)(\hat{\sigma}_+ + \hat{\sigma}_-) \quad (4.12)$$

where $P_x = -i\hbar\frac{\partial}{\partial x}$ is the transverse momentum of the atom, \hbar is Plank constant, M is the atomic mass, $\hat{\sigma}_z$ is the z component of the Pauli operator and $\hat{\sigma}_+(\hat{\sigma}_-)$ is the

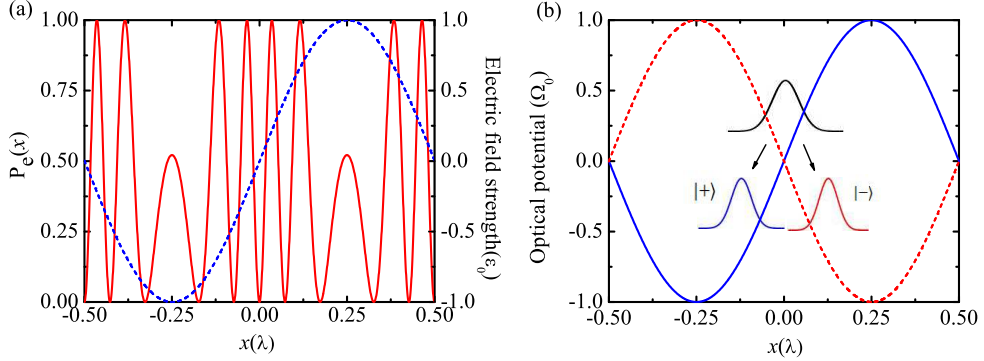


Figure 4.6: a) Sub-wavelength structure in the Raman-Nath approximation. Dashed line is the normalized electric field strength of the standing wave, and the solid curve is the probability of the atom in the excited state. b) Optical Stern-Gerlach effect. The $|+\rangle$ state and $|-\rangle$ state see different optical potentials and an incoming atomic wavepacket splits into two wavepackets.

raising (lowering) operator. The Rabi frequency $\Omega(x, t)$ is given by Eq. (4.12).

The longitudinal velocity v_z is much larger than the recoil velocity of the photon. It is almost unchanged in the whole process and therefore we can treat the motion in the z direction classically. While the transverse velocity is collimated to be on the order of recoil velocity, we treat the atom in transverse direction quantum mechanically, i.e., the atomic wave function in this direction is written as a wave packet. Therefore, the atomic state can be expressed as

$$\Psi(x, t) = \begin{pmatrix} \psi_e(x, t) \\ \psi_g(x, t) \end{pmatrix} \quad (4.13)$$

where $\psi_g(x, t)$ and $\psi_e(x, t)$ are the center-of-mass wavefunction when the atom is in the ground and excited state, respectively. At room temperature, the population in the excited state is negligible and we can assume that all the atoms are in the ground state initially.

The dynamics of the atomic beam can be described by the coupled Schrödinger equations

$$i\dot{\psi}_g(x, t) = -\frac{\hbar}{2M}\psi_g''(x, t) + \frac{\Omega(x, t)}{2}\psi_e(x, t) \quad (4.14)$$

$$i\dot{\psi}_e(x, t) = -\frac{\hbar}{2M}\psi_e''(x, t) + \frac{\Omega(x, t)}{2}\psi_g(x, t) \quad (4.15)$$

For general case, the exact solution of these equations is difficult to obtain. We should either do some approximation or use numerical method to solve them.

4.3.2.1 Raman-Nath regime

If the transverse velocity of the atom is small and the kinetic energy acquired by the atom during the interaction time is small, the Raman-Nath approximation is valid where we can drop the kinetic energy term in the Hamiltonian [113]. For zero-detuning, the simplified Hamiltonian becomes

$$H(x, t) = \frac{\hbar\Omega(x, t)}{2}(\hat{\sigma}_+ + \hat{\sigma}_-) \quad (4.16)$$

Assuming that the atomic beam is spatially uniform and perfectly collimated, the center-of-mass wave function can be written as a plane wave $\psi_g(x, 0) \sim \exp(ik_0x)$, where $\hbar k_0$ is the initial transverse momentum of the atom. For simplicity, we assume $k_0 = 0$ and the mirrors for the standing wave have perfect reflectivity. We can calculate the spatial distribution of the atoms in the excited state by the pulse area theorem and it is given by

$$\begin{aligned} P_e(x, t) &= \frac{1 - \cos[\int_{-\infty}^{\infty} \Omega(x, t) dt]}{2} \\ &= \frac{1 - \cos[\sqrt{\pi}\Omega_0 \cdot (\frac{w_0}{v_z}) \cdot \sin kx]}{2} \end{aligned} \quad (4.17)$$

Around the nodes of the standing wave, we have $P_e(x) \sim \cos[\sqrt{\pi}\Omega_0(w_0/v_z)kx]$. We can see that the effective wavelength is given by

$$\lambda_{eff} = \frac{\lambda}{\sqrt{\pi}\Omega_0 w_0/v_z} \quad (4.18)$$

which can be much smaller than the diffraction limit when we increase the Rabi frequency or the interaction time. This is the basic principle of our sub-wavelength atom lithography scheme. One example is shown in Fig. 4.6(a) where $\Omega_0 = 0.4GHz$, $w_0 = 20\mu m$, and $v_z = 1000m/s$. The spacing around the node is about $\lambda/14$. If we increase the Rabi frequency to be about $2GHz$, the spacing around the node would be about $\lambda/70$.

4.3.2.2 Optical Stern-Gerlach effect

For the resonant case, the optical dipole force is zero. However, because the wave nature of the atom may still see an optical potential which can be described by optical Stern-Gerlach effect [114, 115]. To see this effect , let's write the dynamic equation in the dressed state picture, i.e.,

$$\phi_{\pm}(x, t) = \frac{1}{\sqrt{2}}[\psi_g(x, t) \pm \psi_e(x, t)]. \quad (4.19)$$

For resonant case, the equations of motion for the dressed state are given by

$$i\dot{\phi}_+(x, t) = -\frac{\hbar}{2M}\phi''_+(x, t) + \Omega(x, t)\phi_+(x, t) \quad (4.20)$$

$$i\dot{\phi}_-(x, t) = -\frac{\hbar}{2M}\phi''_-(x, t) - \Omega(x, t)\phi_-(x, t) \quad (4.21)$$

where $\Omega(x, t)$ is given by Eq. (4.12). We can see that ϕ_+ and ϕ_- see opposite optical potentials. An atomic wave packet in the nodes will split into two wave packets. The

atom in $|+\rangle$ state is pulled to the field amplitude minimum while the atom in $|-\rangle$ state is pulled to the field amplitude maximum (see Fig. 4.6(b)).

The force felt by the atomic wave packet can be obtained from the derivative of the optical potential and is given by

$$F(x, t) = \hbar k \Omega_0 \exp\left[-\frac{(v_z t)^2}{w_0^2}\right] \cos(kx) \quad (4.22)$$

The acceleration $a(t)$ is then given by $F(x, t)/M$. Around the node, the velocity acquired by the optical Stern-Gerlach effect is given by

$$v_{OSG} \approx \sqrt{\pi} \Omega_0 \cdot \left(\frac{w_0}{v_z}\right) \cdot v_r \quad (4.23)$$

where $v_r = \frac{\hbar k}{M}$ is the recoil velocity. The distance that separates the two wave packets is about

$$d_{OSG} \approx 2\sqrt{\pi} \Omega_0 \left(\frac{w_0}{v_z}\right) v_r \left(\frac{t_{in}}{4} + t_{ff}\right) \quad (4.24)$$

where $t_{in} = 3w_0/v_z$ is the interaction time and t_{ff} is the free flying time after the standing wave. For an incoming atomic beam, the optical Stern-Gerlach effect can be neglected if $d_{OSG} \ll \lambda$. However, if d_{OSG} approaches λ , the optical Stern-Gerlach effect is significant where the atoms tend to accumulate around the electric field minimum and maximum.

In our lithography scheme the optical Stern-Gerlach effect may destroy the sub-wavelength features and needs to be suppressed. Therefore, the parameters need to be chosen such that d_{OSG} is much less than λ . From Eq. (4.19) and Eq. (4.25) we can determine the smallest resolution without significant optical Stern-Gerlach effect and it is given by

$$\lambda_{eff} \gg 2v_r \left(\frac{t_{in}}{4} + t_{ff}\right). \quad (4.25)$$

For the parameters in our proposed experimental setup, λ_{eff} is much larger than $5nm$ without significant optical Stern-Gerlach effect. If we put the potoresit close to the edge of the standing wave such that t_{ff} approaches zero, the resolution can be less than $5nm$ without significant optical Stern-Gerlach effect.

4.3.2.3 Beyond the Raman-Nath regime: Numerical method

If the atoms are not perfectly collimated or the optical potential is deep, we can not simply neglect the kinetic energy term, i.e., we need to consider the regime beyond the Raman-Nath approximation. The analytical solution beyond the Raman-Nath regime is difficult and usually the numerical method is used to calculate the dynamics.

Let us assume that the transverse momentum distribution is Gaussian, and it is given by

$$\psi_g(p) = \frac{1}{\pi^{1/4}(\delta p)^{1/2}} \exp\left[-\frac{p^2}{(\delta p)^2}\right]. \quad (4.26)$$

where the full width at half maximum of the momentum is $\Delta p = 2\sqrt{\ln 2}\delta p$. On taking the Fourier transformation of $\psi_g(p)$, we can obtain the corresponding wavepacket in the coordinate space which is given by

$$\psi_g(x) = \frac{1}{\pi^{1/4}(\delta x)^{1/2}} \exp\left[-\frac{x^2}{(\delta x)^2}\right] \quad (4.27)$$

where $\delta x = \hbar/\delta p$. The full width at half maximum in the coordinate space is $\Delta x = 2\sqrt{\ln 2}\delta x$. For example, if the atom is cooled to the recoil limit such that $\Delta p = \hbar k$, the width of the wavepacket is $\Delta x = 0.44\lambda$.

The Hamiltonian in Eq. (4.13) can be decomposed into kinetic energy part $T = P_x^2/2M$ and the potential energy part $V(x, t) = \hbar\delta S^Z + \hbar\Omega(x, t)(S^+ + S^-)$. We can numerically solve this equation using the split-operator method [93]. For small time

interval dt , we have

$$\Psi(x, t + dt) \cong e^{-\frac{iVdt}{2\hbar}} e^{-\frac{iTdt}{\hbar}} e^{-\frac{iVdt}{2\hbar}} \Psi(x, t) \quad (4.28)$$

The error of this approximation is on the order of dt^3 and this method is norm preserving. For the potential term we can calculate the exponent by diagonalizing the potential matrix. For the kinetic energy term we can transform the atomic wave function in the coordinate space into the momentum space using fast Fourier transformation algorithm. In the momentum space, the kinetic energy operator is a number $p_x^2/2M$. After calculating the kinetic energy term we apply an inverse Fourier transformation to convert the wave function in the momentum space into the coordinate space. Repeating this procedure we can evolve the wave packet in time.

4.3.3 Numerical results

In the numerical simulation we assume that multiple atomic wavepackets which are uniformly distributed in the space fly through the standing wave and they impinge on the photoresist independently. The beam waist of the standing wave in the z direction is $w_0 = 20\mu m$ and the photoresist is placed about $60\mu m$ away from the center of the standing wave. The interaction time is $3w_0/v_z$ which is about $60ns$ while the free fly time is about $30ns$. The life time of the excited state is about $200ns$ [116]. Therefore it is safe to neglect the decay of the atom in the simulation. We first consider one dimensional case followed by the two dimensional case.

4.3.3.1 One dimensional pattern

If the standing wave is in x direction and the beam waist in the y direction is much larger than one wavelength, we can simply treat this situation as one dimensional

problem. We calculate the population distribution and the atom in the excited state distribution along the x direction. We compare three different collimation: $\Delta v_{\perp} = 100v_r$, $\Delta v_{\perp} = 10v_r$, and $\Delta v_{\perp} = v_r$.

Figures 4.7(a-c) are the results when the peak Rabi frequency is $0.4GHz$. We can see that the spatial distribution of the atom along the x direction is quite uniform for all three cases (dotted lines). The optical Stern-Gerlach effect is not obvious because $\lambda_{eff} = 30nm$ for this Rabi frequency is much larger than $4nm$. However, we can clearly see the sub-wavelength structures in the spatial distribution of the atoms in the excited state when $\Delta v_{\perp} = 10v_r$ and $\Delta v_{\perp} = v_r$. The spacing between peaks near the node for $\Delta v_{\perp} = v_r$ is about $31nm$ (Fig. 4.7(c)) which is consistent with the result ($30nm$) calculated by the Raman-Nath approximation. The smallest spacing for $\Delta v_{\perp} = 10v_r$ is about $32nm$ (Fig. 4.7b) which is also close but slightly larger than $30nm$ in the Raman-Nath approximation. In these two cases, the Raman-Nath approximation is still very good. However, for the bad collimation $\Delta v_{\perp} = 100v_r$, the sub-wavelength structure for the spatial distribution of the atom in the excited state is completely erased(Fig. 4.7a). Therefore, the collimation of the atoms is very important for observing the sub-wavelength structures in our proposed experiment.

Figure 4.7(d-e) are the results when the peak Rabi frequency is $2GHz$. As $\lambda_{eff} = 6nm$ is close to the limit resolution $4nm$, new structures appear in the spatial distribution of the atoms where we can see that there are two peaks within one wavelength due to the optical Stern-Gerlach effect (dotted lines). The positions of the peak are the minimum and the maximum of the electric field strength. The period of these structures is still limited by half-wavelength. On the other hand, let us look at the spatial distributions of the atoms in the excited state which are shown as solid line. We can see that regular sub-half-wavelength structures survives only when $\Delta v_{\perp} = v_r$ (Fig. 4.7(f)). These structures are also affected by the optical

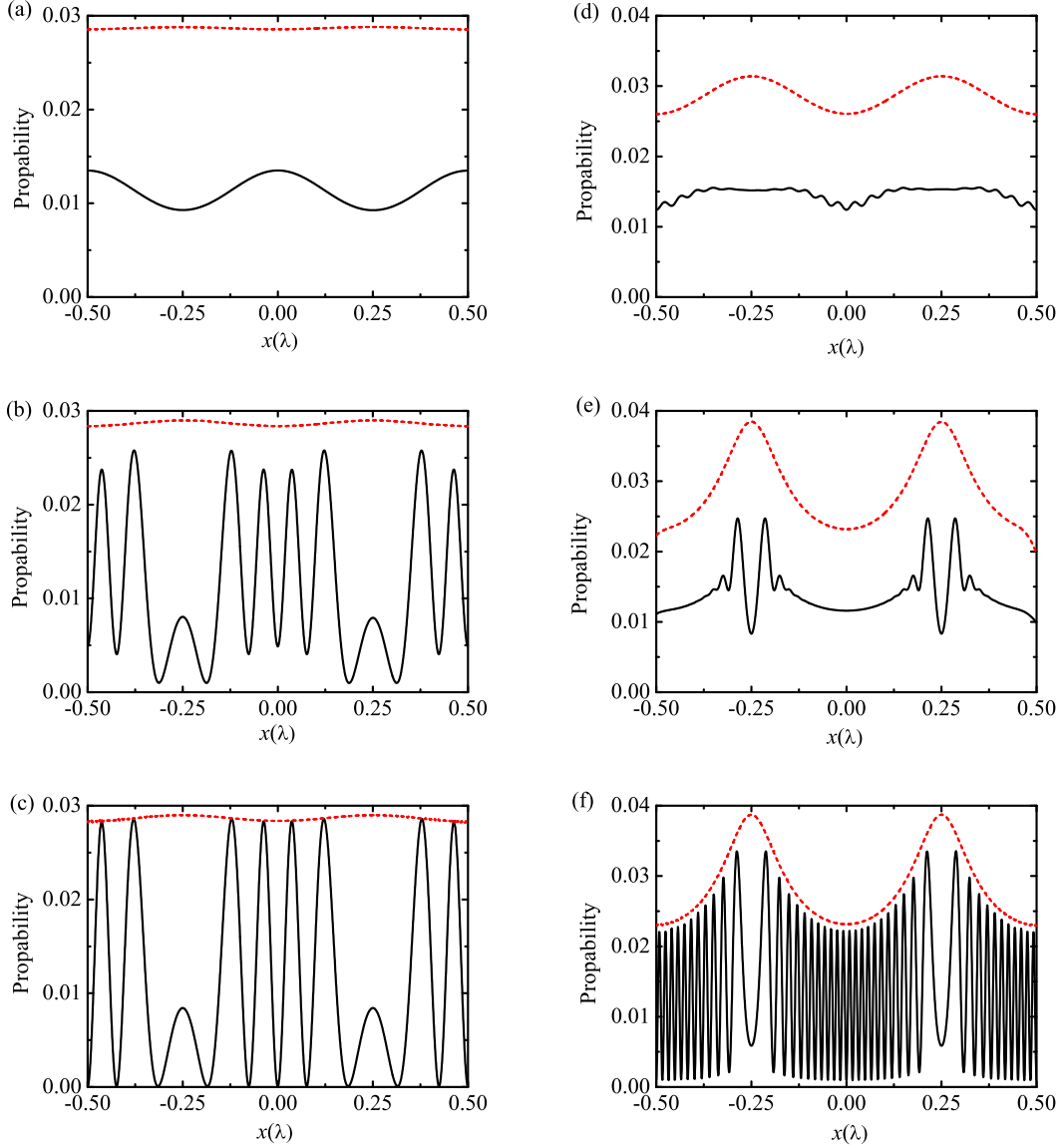


Figure 4.7: Spatial distribution of the atom (dotted line) and the atom in the excited state (solid line) after the standing wave for different peak rabi frequencies and different transverse velocity collimation. Peak Rabi frequencies: (a-c) $\Omega_0 = 0.4\text{GHz}$ while $\Omega_0 = 2\text{GHz}$ for (d-f). Transverse velocity collimation: (a,d) $\Delta v_\perp = 100v_r$; (b,e) $\Delta v_\perp = 10v_r$; (c,f) $\Delta v_\perp = v_r$.

Stern-Gerlach effect. The smallest spacing in Fig. 4.7(f) is about 6.8nm which is close to the result (6nm) calculated by the Raman-Nath approximation. For the other two cases the regular sub-half-wavelength structures disappear due to the bad collimation (Fig. 4.7(d,e)).

4.3.3.2 Two dimensional pattern

In the previous section we discussed the one dimensional case when the variation of the field in y direction within one wavelength is negligible. Here we discuss the two dimensional case when both the fields in the x and y directions may significantly change within one wavelength.

In the two dimensional case, we need to do the following change: $P_x^2 \rightarrow P_x^2 + P_y^2$, $\Omega(x, t) \rightarrow \Omega(x, y, t)$, and $\Psi(x, t) \rightarrow \Psi(x, y, t)$. In the simulation, we should do 2D FFT instead of 1D FFT. The initial wavepacket is given by

$$\psi_g(x, y, t) = \frac{1}{(\pi\delta x\delta y)^{1/2}} \exp\left[-\frac{x^2}{(\delta x)^2}\right] \exp\left[-\frac{y^2}{(\delta y)^2}\right] \quad (4.29)$$

where $\delta y = \hbar/\delta p_y$ and δp_y is the uncertainty of the momentum in y direction. Here we assume that the collimation in x and y directions are the same, and thus $\delta x = \delta y$. The initial wavepackets are uniformly distributed in the xy plane. For the following simulations, we assume the collimation in both direction is of the order of recoil limit.

In the first example, the standing wave is in the x direction while the electric fields in the y and z direction are Gaussian distribution with beam waists $w_y = w_z = 20\mu\text{m}$. As w_y is much larger than λ , the electric field within one wavelength around the center is about constant and the result would be similar to the one dimensional case. Indeed, the numerical results shown in Fig. 4.8(a) and Fig. 4.8(b) give similar features as the one dimensional case (Fig. 4.7(f)). We see that the atom population around the amplitude maximum and minimum is higher than other positions which is the

evidence of the optical Stern-Gerlach effect. The spacing of the atom distribution peak is $\lambda/2$ which is still diffraction-limited. However, we can clearly see that the excited atom population distribution has much finer feature than the diffraction limit. The closest line spacing is about 7nm .

In the second example, we add another standing wave in y direction in addition to the standing wave in x direction. We assume both standing waves have the same wavevector and amplitude. The peak Rabi frequency is $\Omega_0 = 2\text{GHz}$. The atom population distribution is shown in Fig. 4.8(c) where we can see that there are four peaks in $\lambda \times \lambda$ region due to the optical Stern-Gerlach effect. However, the spacing between the peaks is still diffraction-limited. The peaks at the extreme points in the anti-diagonal direction are higher than the peaks at the saddle points in the diagonal direction. The excited atom population distribution is shown in Fig. 4.8(d) where we can see nanometer ring fringe.

In practice, There are several parameters of the lasers that we can control to generate more complicated patterns. The nodes of the standing wave can be changed by tuning the phase of the standing wave. The period of the pattern can be controlled by the power or the longitudinal width of the laser. We can also shine more than two lasers from different directions to generate more complicated spatial distribution of the electric field which can print more complicated patterns.

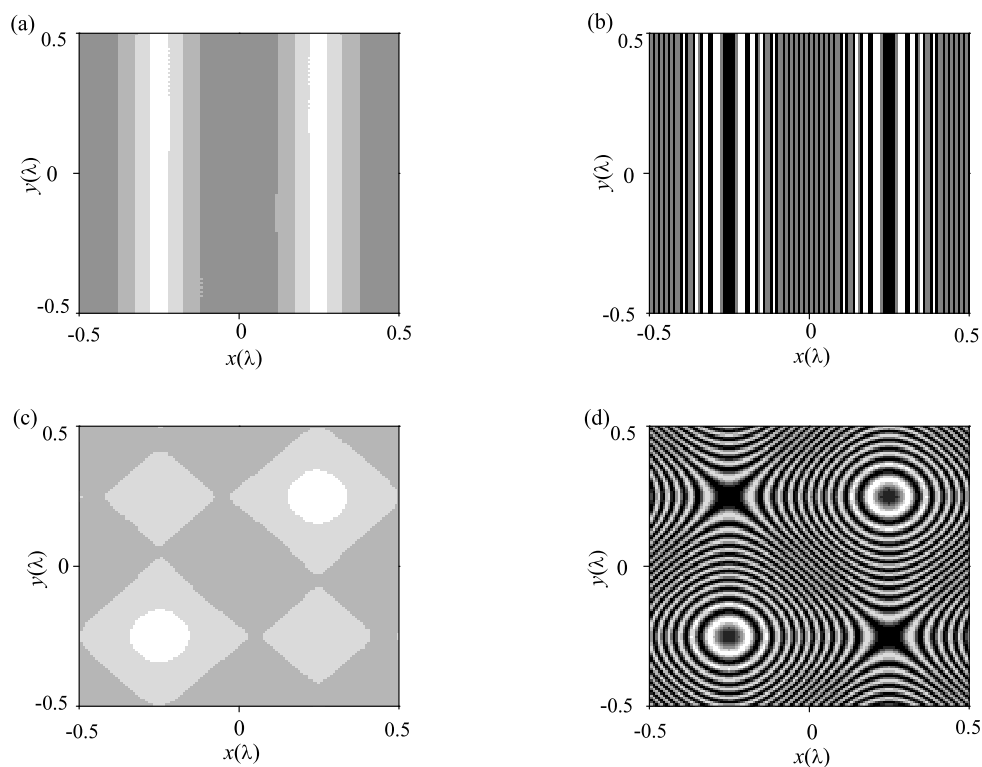


Figure 4.8: Spatial distribution of the atom (a,c) and the atom in the exited state (b,d). The brighter the higher probability. Peak Rabi frequencies: $\Omega_0 = 2GHz$.

5. RESONANCE FLUORESCENCE LOCALIZATION MICROSCOPY BEYOND THE DIFFRACTION LIMIT*

Resonance fluorescence has been shown to be able to localize the position of a single atom with resolution beyond the diffraction limit. It has also been shown that the separation between two atoms, which is smaller than the diffraction limit, can also be extracted from the resonance fluorescence spectrum. In this chapter, we evaluate the resonance fluorescence spectrum of N two-level atoms driven by a laser with gradient field strength and show that we can determine the positions of the atoms from the spectrum even if there multiple atoms within one diffraction-limited spot and the dipole-dipole interaction is significant. This far-field resonance fluorescence localization microscopy method does not require point-by-point scanning and it may be more time-efficient. We also give a possible scheme to extract the position information in an extended region without requiring more peak power of the laser. Finally we briefly discuss how to extend our scheme to do a 2D imaging.

5.1 Resonance fluorescence

Resonance fluorescence is the radiation reemitted by a two-level atom which is resonantly driven by a monochromatic laser light. If the intensity of the driving field is low, the reemitted light has the same frequency as that of the driving field. However, if the intensity of the driving field becomes comparable to, or larger than, the atomic linewidth, the atoms can undergo several Rabi oscillations and the emission spectrum has sidebands which is also called the dynamic Stark splitting.

*Reprinted with permission from Resonance Fluorescence Localization Microscopy with Sub-wavelength Resolution by Z. Liao and M. Al-Amri and M. S. Zubairy, 2012. Phys. Rev. A, vol. 85, pp. 023810, Copyright [2012] by the American Physical Society.

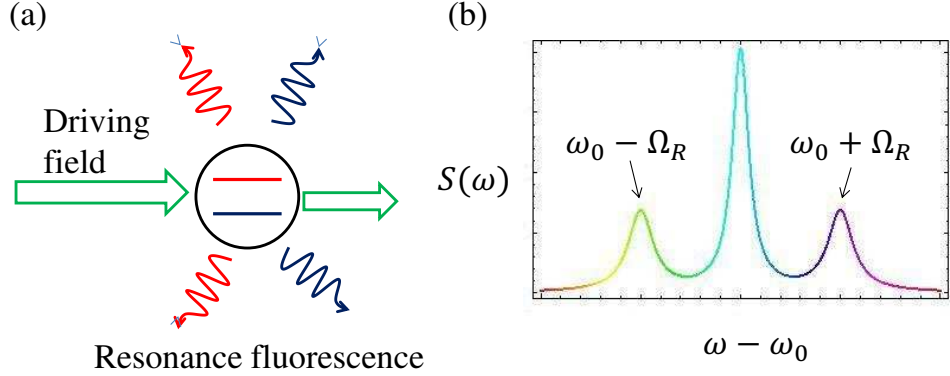


Figure 5.1: (a) Pictorial presentation of resonant light scattering. (b) Mollow triplet shown in resonance fluorescence spectrum.

5.1.1 Mollow triplet

According to the Wiener-Khintchine theorem, the power spectrum of the resonance fluorescence in the steady state is given by [82]

$$S(\vec{r}, \omega) = \frac{1}{\pi} \text{Re} \left[\lim_{t \rightarrow \infty} \int_0^\infty d\tau e^{i\omega\tau} \langle E^-(\vec{r}, t) E^+(\vec{r}, t + \tau) \rangle \right] \quad (5.1)$$

The two-time field correlation function depends only on the time difference τ and it is related to the atomic transition by

$$\langle E^-(\vec{r}, t) E^+(\vec{r}, t + \tau) \rangle = I_0(\vec{r}) \langle \sigma^+(t) \sigma^-(t + \tau) \rangle \quad (5.2)$$

where

$$I_0(\vec{r}) = \left(\frac{\omega^2 \mu \sin \eta}{4\pi\epsilon_0 c^2 |\vec{r} - \vec{r}_0|} \right)^2, \quad (5.3)$$

$\sigma^+(\sigma^-)$ is the atomic raising (lowering) operator, ω is the atomic transition frequency, and η is the angle between the transition dipole moment and the observation direction.

tion.

The two-time atomic correlation function $\langle \sigma^+(t)\sigma^-(t+\tau) \rangle$ can be calculated from the one-time correlation function $\langle \sigma^-(t) \rangle$ by using the quantum regression theorem (Appendix B). The quantum regression theorem says that: if operator \hat{O} satisfies

$$\langle \hat{O}(t+\tau) \rangle = \sum_j a_j(\tau) \langle \hat{O}_j(t) \rangle, \quad (5.4)$$

then we have the two-time correlation function given by

$$\langle \hat{O}_i(t) \hat{O}(t+\tau) \hat{O}_k(t) \rangle = \sum_j a_j(\tau) \langle \hat{O}_i(t) \hat{O}_j(t) \hat{O}_k(t) \rangle. \quad (5.5)$$

Since $\langle \sigma^-(t) \rangle = Tr(\sigma^-(t)\rho) = \rho_{ab}(t)$, the one-time correlation function $\langle \sigma^-(t) \rangle$ satisfies the same equation as $\rho_{ab}(t)$ which can be directly calculated from the master equation. The master equation for a single atom is given by

$$\dot{\rho} = -\frac{i}{\hbar}[V, \rho] - \frac{\Gamma}{2}(\sigma^+ \sigma^- \rho + \rho \sigma^+ \sigma^- - 2\sigma^- \rho \sigma^+) \quad (5.6)$$

where the interaction Hamiltonian $V = \frac{\hbar\Omega_R}{2}(\sigma^+ + \sigma^-)$ and Γ is the spontaneous emission rate. From Eq. (5.6), ρ_{eg} is given by [82]

$$\rho_{ab}(t+\tau) = a_1(\tau) + a_2(\tau) \langle \sigma^-(t) \rangle + a_3(\tau) \langle \sigma^+(t) \rangle + a_4(\tau) (\langle \sigma^z(t) \rangle + 1)/2 \quad (5.7)$$

where

$$a_1(\tau) = \frac{-i\Omega_R\Gamma}{2\Omega_R^2 + \Gamma^2} \left\{ 1 - e^{-3\Gamma\tau/4} [\cos(\lambda\tau) - (\frac{4\Omega_R^2 - \Gamma^2}{4\lambda\Gamma}) \sin(\lambda\tau)] \right\}, \quad (5.8)$$

$$a_2(\tau) = \frac{1}{2}e^{-\Gamma\tau/2} + \frac{e^{-3\Gamma\tau/4}}{8\lambda} [\Gamma \sin(\lambda\tau) + 4\lambda \cos(\lambda\tau)], \quad (5.9)$$

$$a_3(\tau) = \frac{1}{2}e^{-\Gamma\tau/2} - \frac{e^{-3\Gamma\tau/4}}{8\lambda} [\Gamma \sin(\lambda\tau) + 4\lambda \cos(\lambda\tau)], \quad (5.10)$$

$$a_4(\tau) = \frac{i\Omega_R}{\lambda} e^{-3\Gamma\tau/4} \sin(\lambda\tau), \quad (5.11)$$

and $\lambda = \sqrt{\Omega_R^2 - (\Gamma/4)^2}$.

Thus, the equation for the two-time correlation function is given by

$$\begin{aligned} \langle \sigma^+(t)\sigma^-(t+\tau) \rangle &= a_1(\tau)\langle \sigma^+(t) \rangle + a_2(\tau)\langle \sigma^+(t)\sigma^-(t) \rangle + a_3(\tau)\langle \sigma^+(t)\sigma^+(t) \rangle \\ &\quad + a_4(\tau)\langle \sigma^+(t)[\sigma^z(t) + 1]/2 \rangle \\ &= a_1(\tau)\langle \sigma^+ \rangle + a_2(\tau)\langle \sigma^+(t)\sigma^-(t) \rangle \end{aligned} \quad (5.12)$$

where we have used the relations $\sigma^+(t)\sigma^+(t) = 0$ and $\sigma^+(t)[\sigma^z(t) + 1] = 0$. In the steady state, we have

$$\lim_{t \rightarrow \infty} \langle \sigma^+ \rangle = \frac{-i\Omega_R\Gamma}{2\Omega_R^2 + \Gamma^2}, \quad (5.13)$$

$$\lim_{t \rightarrow \infty} \langle \sigma^+(t)\sigma^-(t) \rangle = \frac{\Omega_R^2}{2\Omega_R^2 + \Gamma^2} \quad (5.14)$$

In the strong field limit, i.e., $\Omega_R \gg \Gamma/4$, we have

$$\langle \sigma^+(t)\sigma^-(t+\tau) \rangle = \frac{1}{4}e^{-\Gamma\tau/2} + \frac{1}{8}e^{-3\Gamma\tau/4}(e^{-i\Omega_R\tau} + e^{i\Omega_R\tau}) \quad (5.15)$$

From Eq. (5.1), (5.2) and (5.15), we obtain

$$S(\vec{r}, \omega) = \frac{I_0(\vec{r})}{8\pi} \left[\frac{\Gamma}{(\omega - \omega_0)^2 + (\Gamma/2)^2} + \frac{3\Gamma/4}{(\omega - \omega_0 - \Omega_R)^2 + (3\Gamma/4)^2} + \frac{3\Gamma/4}{(\omega - \omega_0 + \Omega_R)^2 + (3\Gamma/4)^2} \right] \quad (5.16)$$

There are three peaks centered at $\omega_0, \omega_0 \pm \Omega_R$ in the spectrum which is well known as the Mollow triplet. The width of the center peak is $\Gamma/2$ while the width of the sidebands is $3\Gamma/4$. The separation between the sideband and the central peak is the Rabi frequency (Fig. 5.1(b)). Therefore, we can determine the Rabi frequency felt by the atom from the resonance fluorescence spectrum. If the Rabi frequency is spatial dependent, we can extract the position of the atom from the resonance fluorescence spectrum.

However, if there are multiple atoms within one diffraction-limited spot, dipole-dipole interaction between the atoms may be significant which may significantly shift the spectrum. In the following, we would theoretically and numerically calculate the resonance fluorescence spectrum of a multi-atom system and show how to extract the spatial information of the atoms even if they are interacting with each other.

5.2 General feature of the N-atom resonance fluorescence

For simplicity, we first consider that some identical atoms are located in the 1D space along the x axis. Our setup is shown in Fig. 5.2. We shine two strong linear polarized laser fields with wavelength λ on these atoms from opposite directions and they form a standing wave. Assume that the polarization orientation is in \hat{y} direction and the frequency is resonant with the two-level atoms. We also assume that the atoms do not move and they locates within one wavelength. This assumption is valid for the following situations: atoms are trapped by optical lattice, quantum dots, NV-centers in diamond and so on. We can stretch the standing wave where the

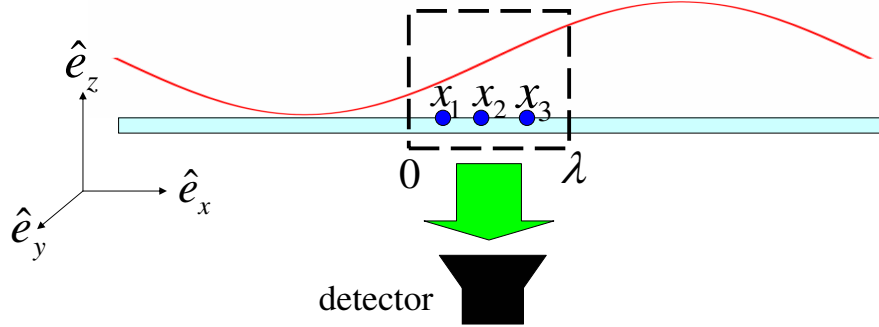


Figure 5.2: Scheme for resonance fluorescence microscopy. x_i is the position of the i th atom.

sample is located within approximately linear region between node and anti-node [59, 31]. In this region, we can write $E(x) = E_0x/\lambda$. We monitor the resonance fluorescence photons emitted by the system with a detector in \hat{z} direction. The resonance fluorescence spectrum encodes the spatial information of the systems from which we can determine the positions of each atom.

The Hamiltonian of the system and the field is [35, 117]

$$H = H_A + H_F + H_{AF} + H_{dd}, \quad (5.17)$$

where $H_A = \hbar\omega_0 \sum_{i=1}^N S_i^z$ is the energy of the atoms, with ω_0 being the level separation and S_i^z is the z component of the spin operator. $H_F = \hbar\omega_0 a^\dagger a$ is the total energy of the photons, where $a(a^\dagger)$ is annihilation (creation) operator of the photon; $H_{AF} = (\hbar/2) \sum_{i=1}^N g_i(S_i^+ a + S_i^- a^\dagger)$ is the interaction between the atoms and the field, with $S_i^+(S_i^-)$ being the raising (lowering) operator on the i th atom, and coupling constant $g_i = gx_i/\lambda$ and $g = \mu(2\omega_0/\hbar\varepsilon_0 V)^{1/2}$ (μ is the transition dipole moment between ground state and excited state); $H_{dd} = \hbar \sum_{i \neq j} \Omega_{ij}(S_i^+ S_j^- + S_i^- S_j^+)$

is the dipole-dipole interaction energy. All transition dipole moments are polarized in y direction and the dipole-dipole interaction energy Ω_{ij} is given by [35, 117, 38]

$$\Omega_{ij} = \frac{3\Gamma}{4} \left\{ -(1 - \cos^2 \phi) \frac{\cos(kx_{ij})}{kx_{ij}} + (1 - 3\cos^2 \phi) \left[\frac{\sin(kx_{ij})}{(kx_{ij})^2} + \frac{\cos(kx_{ij})}{(kx_{ij})^3} \right] \right\}, \quad (5.18)$$

with $2\Gamma = 4\omega_0^3 d_0^2 / (3\hbar c^3)$ being the single-atom spontaneous decay rate, ϕ is the angle of the dipole with respect to atomic chain direction, $k = \omega_0/c$ (c is speed of light) and x_{ij} is the distance between atoms [117, 118]. The Rabi frequency for the i th atom is given by $\Omega_i = g_i \sqrt{n}$ (or $\mu E_0 x_i / \hbar \lambda$) where n is the photon number.

The spectrum of resonance fluorescence can be evaluated by [119, 120]

$$S(\omega) \propto \text{Re} \left[\int_0^\infty d\tau e^{i\omega\tau} \lim_{t \rightarrow \infty} \langle D^+(t) D^-(t + \tau) \rangle \right], \quad (5.19)$$

where D^+ and D^- are the raising and lowering parts of the total atomic dipole operator. The lowering part can be written as $D^- = \sum_{\alpha\beta n} d_{\alpha\beta}^- |\beta, n-1\rangle \langle \alpha, n| = \sum_{\alpha\beta} D_{\alpha\beta}^-$, where $d_{\alpha\beta}^-$ is the dipole matrix element of the transition from $|\alpha, n\rangle$ to $|\beta, n-1\rangle$ and it is defined by $d_{\alpha\beta}^- = \langle \beta, n-1 | \sum_{i=1}^N S_i^- | \alpha, n \rangle$ and $D_{\alpha\beta}^- = \sum_n d_{\alpha\beta}^- |\beta, n-1\rangle \langle \alpha, n|$.

We can write the two-time correlation function in Eq. (5.19) as

$$\langle D^+(t) D^-(t + \tau) \rangle = \sum_{\alpha \neq \beta} \langle D^+(t) D_{\alpha\beta}^-(t + \tau) \rangle + \sum_{\alpha} \langle D^+(t) D_{\alpha\alpha}^-(t + \tau) \rangle \quad (5.20)$$

where the first term corresponds to the sideband spectrum while the second term corresponds to the central peak. According to the quantum regression theorem [82], the two-time correlation function $\langle D^+(t) D_{\alpha\beta}^-(t + \tau) \rangle$ satisfies the same equation of motion as the single time average $\langle D_{\alpha\beta}^-(t) \rangle$. The dynamics of $\langle D_{\alpha\beta}^-(t) \rangle$ can be

calculated from the master equation:

$$\frac{d\langle D_{\alpha\beta}^-(t) \rangle}{dt} = d_{\alpha\beta}^- \frac{d\rho_{\alpha\beta}^-}{dt} = d_{\alpha\beta}^- \left\{ \frac{-i}{\hbar} [H, \rho]_{\alpha\beta} - (L\rho)_{\alpha\beta} \right\} \quad (5.21)$$

where $\rho_{\alpha\beta}^- = \langle \alpha, n | \rho | \beta, n-1 \rangle$, $L = \sum_{i,j=1}^N \Gamma_{ij} (S_i^+ S_j^- \rho + \rho S_i^+ S_j^- - 2 S_j^- \rho S_i^+)$ is the relaxation operator with Γ_{ii} being the decay rate of atom i and Γ_{ij} being the cross damping rate. For the sidebands, we can expand $(L\rho)_{\alpha\beta} = \Gamma_{\alpha\beta} \rho_{\alpha\beta} + \dots$ and, from Eq. (5.21), we have

$$\frac{d}{dt} \langle D_{\alpha\beta}^-(t) \rangle \simeq (i\omega_{\alpha\beta} - \Gamma_{\alpha\beta}) \langle D_{\alpha\beta}^-(t) \rangle, \quad (5.22)$$

where we have neglected the non-resonance terms on the right hand side in the secular approximation. For the central peak, as all $|\alpha, n\rangle \rightarrow |\alpha, n-1\rangle$, $\alpha = 1, \dots, 2^N$ have the same transition frequency, they couple to each other and we can expand $(L\rho)_{\alpha\alpha} = \sum_{\beta} \Gamma'_{\alpha\beta} \rho_{\beta\beta} + \dots$. From Eq. (5.21) we get

$$\frac{d}{dt} \langle D_{\alpha\alpha}^-(t) \rangle = i\omega_0 \langle D_{\alpha\alpha}^-(t) \rangle - d_{\alpha\alpha}^- \sum_{\beta} \Gamma'_{\alpha\beta} \frac{\langle D_{\beta\beta}^-(t) \rangle}{d_{\beta\beta}^-}. \quad (5.23)$$

According to the quantum regression theorem and Eq. (5.19), the spectrum is given by

$$\begin{aligned} S(\vec{R}, \omega) &= S^0(\omega) + S^{\pm}(\omega) \\ &\propto Re \left[\int_0^{\infty} d\tau e^{i(\omega-\omega_0)\tau} \sum_{\alpha,\beta} d_{\alpha\alpha}^- (e^{-\Gamma'\tau})_{\alpha\beta} d_{\beta\beta}^+ \right] + \sum_{\alpha \neq \beta} \frac{|d_{\alpha\beta}^-|^2 \Gamma_{\alpha\beta}}{(\omega - \omega_{\alpha\beta})^2 + \Gamma_{\alpha\beta}^2} \end{aligned} \quad (5.24)$$

where the first term yields the central peak spectrum and the second term gives the sideband spectrum.

In the general cases, the spectrum is very complicated. In the following, we

would like to consider a special case that the dipole-dipole interaction is not too strong where we can find the general feature of the spectrum.

5.2.0.1 $\Omega_i \gg \Omega_{ij}$

If the dipole-dipole interaction energy is not very strong, we can apply a strong laser field such that $\Omega_i \gg \Omega_{ij}$. In this case, we can analytically evaluate the collective resonance fluorescence spectrum of multi-atom system based on a dressed state picture [119, 120]. Let $H_0 = H_A + H_F + H_{AF}$ and treat H_{dd} as a perturbation term. The eigenvalues and eigenfunctions of H_0 are given by [39]

$$E_{\alpha,n}^0 = (n - \frac{N}{2})\hbar\omega_0 + \frac{\hbar}{2} \sum_{i=1}^N \chi_i^\alpha \Omega_i, \quad (5.25)$$

$$\begin{aligned} |\alpha, n\rangle &= \frac{1}{\sqrt{2^N}} (|b^N, n\rangle + \sum_{i=1}^N \chi_i^\alpha |a_i b^{N-1}, n-1\rangle + \sum_{i \neq j} \chi_i^\alpha \chi_j^\alpha |a_i a_j b^{N-2}, n-2\rangle + \dots \\ &\quad + \prod_{i=1}^N \chi_i^\alpha |a^N, n-N\rangle), \end{aligned} \quad (5.26)$$

where N is the number of atoms, $\alpha = 1, 2, \dots, 2^N$, $|a_i b^{N-1}\rangle$ means that i th atom is in the excited state $|a\rangle$ while other $N-1$ atoms are in the ground state $|b\rangle$, and χ_i^α is a constant which can be either $+1$ or -1 . Counting the dipole-dipole interaction term as a perturbation, the eigenenergy is shifted by

$$\Delta_{\alpha,n} = \frac{\hbar}{2} \sum_{i \neq j} \chi_i^\alpha \chi_j^\alpha \Omega_{ij} \quad (5.27)$$

and the correction to zeroth order eigenfunction is of the order of Ω_{ij}/Ω_i which can be neglected. The sublevel energy $E_{\alpha,n} = E_{\alpha,n}^0 + \Delta_{\alpha,n}$. The pictorial energy level for the dressed state picture is shown in Fig. 5.4. Coupling of the dressed states to

the vacuum results in the system's cascade down the ladder from the α state of one multiplet to the β state of the adjacent multiplet [119]. The corresponding transition frequency is $\omega_{\alpha\beta} = (E_{\alpha,n} - E_{\beta,n-1})/\hbar$, where $\alpha, \beta = 1, 2, \dots, 2^N$.

For the zeroth order wavefunction (Eq. (5.26)), the transition dipole moment is given by

$$d_{\alpha\beta}^- = \frac{1}{2^N} \sum_{i=1}^N \left\{ \chi_i^\beta \prod_{k \neq i} [1 + \chi_k^\alpha \cdot \chi_k^\beta] \right\}. \quad (5.28)$$

We have three cases:

1. $\beta = \alpha$, $d_{\alpha\beta}^- = \sum_{i=1}^N \chi_i^\alpha / 2$ which contributes to the central peak $\omega = \omega_0$;
2. $\beta = \alpha^p$ (α^p is a state such that E_α^0 and $E_{\alpha^p}^0$ have different sign only in p th term), $d_{\alpha\beta}^- = \chi_p^\alpha / 2$ which contributes to the sidebands

$$\omega_{\alpha\alpha^p} = \omega_0 + \chi_p^\alpha \Omega_p + \sum_{k \neq p} \chi_p^\alpha \chi_k^\alpha \Omega_{pk}; \quad (5.29)$$

From this equation, we see that the positive sideband peaks can be divided into N groups: $\Omega_p + \sum_{k \neq p} \pm \Omega_{pk}$, $p = 1, \dots, N$. Averaging over the frequencies of each group we can get the Rabi frequencies Ω_p from which we can determine the positions of the atoms. The error is on the order of $\Omega_{ij}^2 / \Omega_i^2 \ll 1$. This is our method for optical microscopy (Fig. 5.3). In the experiment, we may not know which peak belongs to which group. However, if we change the gradient of the laser field by an amount, the relative Rabi frequencies for different atoms change which will change the separations of the spectrum belongs to different groups. Because the dipole-dipole interactions do not change, the splitting between peaks belong to the same group will not change. From this phenomena we can identify peaks belong to different groups.

3. $\alpha \neq \beta$ and more than one term of E_α^0 and E_β^0 have different signs, $d_{\alpha\beta}^- = 0$

Atom localization

The positive sideband spectrum:

$$\omega = \omega_0 + \Omega_p + \sum_{k \neq p} \chi_k^\alpha \Omega_{pk}, \text{ with } p = 1, 2, \dots, N, \chi_k^\alpha = \pm 1.$$

The average sideband frequency belongs to each p :

$$\bar{\omega} = \omega_0 + \Omega_p$$

Rabi frequency at the position of atom p :

$$\Omega_p = \bar{\omega} - \omega_0$$

From Ω_p , we can determine the position x_p of the atom p .

Figure 5.3: Principle of atom localization from resonance fluorescence spectrum.

which corresponds to the forbidden transition.

The method described above is valid under the conditions: $\Omega_i \gg \Omega_{ij}$ and $|\Omega_i - \Omega_j| - 2\Omega_{ij} \gg \Gamma$. Assuming that $\Gamma \sim 10^8 Hz$ and the maximum Rabi frequency is $10^{13} Hz$, then the smallest distance we can resolve in this method is about $\lambda/50$.

5.3 Three-atoms example

In the following, we study the resonance fluorescence spectrum of a three-atom system to demonstrate how our localization microscopy works. The dressed state

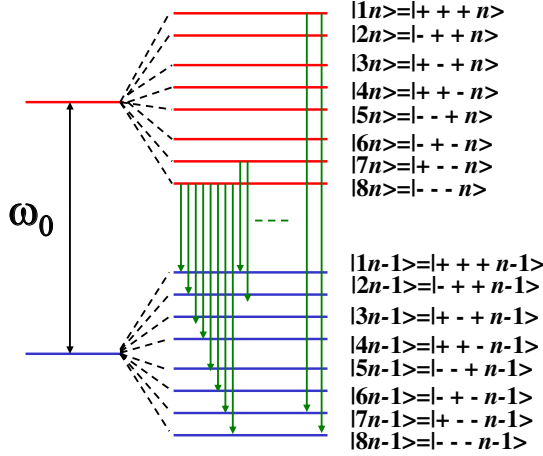


Figure 5.4: Dressed state picture for three interacting atoms. $|\pm\pm\pm n\rangle = (|bn_1\rangle \pm |an_1 - 1\rangle) \otimes (|bn_2\rangle \pm |an_2 - 1\rangle) \otimes (|bn_3\rangle \pm |an_3 - 1\rangle)$ where $n_1 + n_2 + n_3 = n$.

picture is shown in Fig. 5.4. From Eq. (5.25), the eigenvalues of the system are

$$\begin{aligned}
E_{1n} &= (n - \frac{3}{2})\hbar\omega_0 + \frac{\hbar}{2}(\Omega_1 + \Omega_2 + \Omega_3 + \Omega_{12} + \Omega_{13} + \Omega_{23}) \\
E_{2n} &= (n - \frac{3}{2})\hbar\omega_0 + \frac{\hbar}{2}(-\Omega_1 + \Omega_2 + \Omega_3 - \Omega_{12} - \Omega_{13} + \Omega_{23}) \\
E_{3n} &= (n - \frac{3}{2})\hbar\omega_0 + \frac{\hbar}{2}(\Omega_1 - \Omega_2 + \Omega_3 - \Omega_{12} + \Omega_{13} - \Omega_{23}) \\
E_{4n} &= (n - \frac{3}{2})\hbar\omega_0 + \frac{\hbar}{2}(\Omega_1 + \Omega_2 - \Omega_3 + \Omega_{12} - \Omega_{13} - \Omega_{23}) \\
E_{5n} &= (n - \frac{3}{2})\hbar\omega_0 + \frac{\hbar}{2}(-\Omega_1 - \Omega_2 + \Omega_3 + \Omega_{12} - \Omega_{13} - \Omega_{23}) \\
E_{6n} &= (n - \frac{3}{2})\hbar\omega_0 + \frac{\hbar}{2}(-\Omega_1 + \Omega_2 - \Omega_3 - \Omega_{12} + \Omega_{13} - \Omega_{23}) \\
E_{7n} &= (n - \frac{3}{2})\hbar\omega_0 + \frac{\hbar}{2}(\Omega_1 - \Omega_2 - \Omega_3 - \Omega_{12} - \Omega_{13} + \Omega_{23}) \\
E_{8n} &= (n - \frac{3}{2})\hbar\omega_0 + \frac{\hbar}{2}(-\Omega_1 - \Omega_2 - \Omega_3 + \Omega_{12} + \Omega_{13} + \Omega_{23})
\end{aligned} \tag{5.30}$$

For weak dipole-dipole interactions, according to Eq. (5.28) the nonzero transi-

tion dipole moments are

(1) Central peak: $d_{11}^\pm = 3/2, d_{22}^\pm = d_{33}^\pm = d_{44}^\pm = 1/2, d_{55}^\pm = d_{66}^\pm = d_{77}^\pm = -1/2, d_{88}^\pm = -3/2$.

(2) Sideband peaks: $d_{12}^- = d_{13}^- = d_{14}^- = d_{25}^- = d_{26}^- = d_{35}^- = d_{37}^- = d_{47}^- = d_{58}^- = d_{68}^- = d_{78}^- = 1/2; d_{21}^- = d_{31}^- = d_{41}^- = d_{52}^- = d_{62}^- = d_{53}^- = d_{73}^- = d_{74}^- = d_{85}^- = d_{86}^- = d_{87}^- = -1/2$.

For central peak, we can also calculate $(L\rho)_{\alpha\alpha} = (3\Gamma/2)\rho_{\alpha\alpha} - (\Gamma/2)\sum_{\alpha'} \rho_{\alpha'\alpha'}$ where $\alpha \rightarrow \alpha'$ is allowed sideband transition. For example, if $\alpha = 1$, then $\alpha' = 2, 3, 4$.

Thus, we have

$$\Gamma' = \frac{\Gamma}{2} \begin{pmatrix} 3 & -1 & -1 & -1 & 0 & 0 & 0 & 0 \\ -1 & 3 & 0 & 0 & -1 & -1 & 0 & 0 \\ -1 & 0 & 3 & 0 & -1 & 0 & -1 & 0 \\ -1 & 0 & 0 & 3 & 0 & -1 & -1 & 0 \\ 0 & -1 & -1 & 0 & 3 & 0 & 0 & -1 \\ 0 & -1 & 0 & -1 & 0 & 3 & 0 & -1 \\ 0 & 0 & -1 & -1 & 0 & 0 & 3 & -1 \\ 0 & 0 & 0 & 0 & -1 & -1 & -1 & 3 \end{pmatrix}$$

From Eq. (5.24), we get the central peak spectrum

$$S^0(\vec{R}, \omega) \propto \frac{3\Gamma}{2} \left[\frac{1}{(\omega - \omega_0)^2 + \Gamma^2} + \frac{18}{(\omega - \omega_0)^2 + 4\Gamma^2} + \frac{9}{(\omega - \omega_0)^2 + 9\Gamma^2} \right]. \quad (5.31)$$

The sideband spectrum is given by

$$S^\pm(\omega) \propto \frac{1}{4} \sum_{\alpha \neq \beta} \frac{\Gamma_{\alpha\beta}}{(\omega - \omega_{\alpha\beta})^2 + \Gamma_{\alpha\beta}^2} \quad (5.32)$$

where $\Gamma_{\alpha\beta}$ is the transition linewidth. When the atoms are not too close such that the

The positive sideband peaks for three-atom example

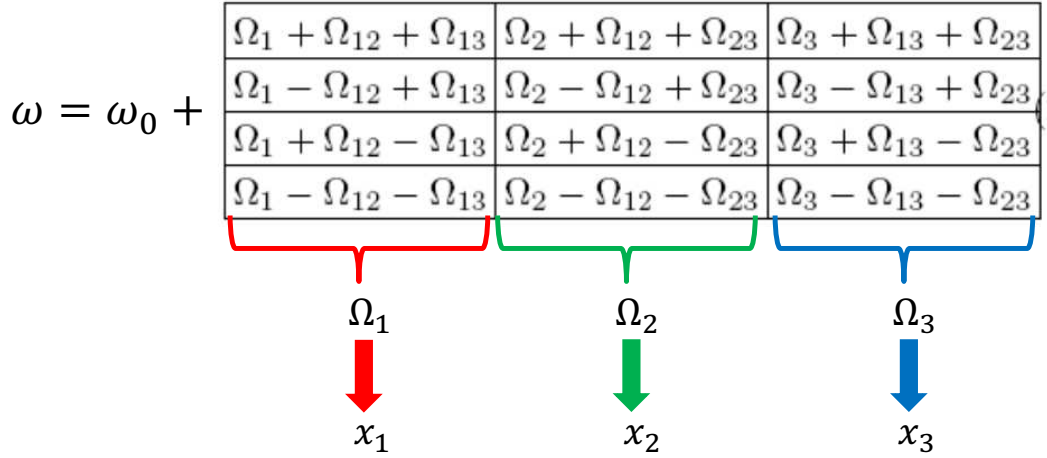


Figure 5.5: Example for three-atom resonance fluorescence microscopy.

dipole-dipole interaction energy is smaller than the single atom transition linewidth, they can be treated as independent atoms. For independent atoms the linewidth of the sideband spectrum is $3\gamma/2$ [120, 82], i.e., $\Gamma_{\alpha\beta} = 3\gamma/2$ in Eq. (5.32). Second, when all the atoms are very close to each others such that all dipole-dipole interaction energies are larger than the single atom transition linewidth, $\Gamma_{\alpha\beta} \approx (N/2 + 1)\gamma$ [39]. The spectrum width is about $(N/2 + 1)\gamma$ which is similar to superradiance [121]. For general cases we need to resort to numerical calculations.

Having the spectrum, we can determine the positions of the atoms (Fig. 5.5). For three-atom system, there are three groups of positive sideband spectrum. Averaging each group of spectrum, we can determine the Rabi frequency felt by each atom. We can then determine the position of the three atoms.

5.4 Numerical calculation of the N-atom resonance fluorescence

For multiple-atom system, we can numerically solve the resonance fluorescence spectrum using the master equation approach. The dynamics of the system is given by

$$\frac{\partial \rho}{\partial t} = -\frac{i}{\hbar}[H, \rho] - \mathcal{L}(\rho) \quad (5.33)$$

where H is the Hamiltonian of the system which is given by Eq. (5.17) and $\mathcal{L}(\rho)$ describes the relaxation of the system which is given by

$$\mathcal{L}(\rho) = \frac{1}{2} \sum_{i,j=1}^N \Gamma_{ij} (\rho S_i^+ S_j^- + S_i^+ S_j^- \rho - 2S_j^+ \rho S_i^-) \quad (5.34)$$

where Γ_{ij} is the correlated decay rate which is

$$\Gamma_{ij} = \frac{3\Gamma}{2} \left\{ [1 - \cos^2 \phi] \frac{\sin(kx_{ij})}{kx_{ij}} + [1 - 3\cos^2 \phi] \left[\frac{\cos(kx_{ij})}{(kx_{ij})^2} - \frac{\sin(kx_{ij})}{(kx_{ij})^3} \right] \right\}. \quad (5.35)$$

For N atoms, the resonance fluorescence spectrum can be calculated by

$$S(\vec{r}, \omega) = I_0(\vec{r}) \text{Re} \left[\int_0^\infty d\tau \langle S^+(t) S^-(t + \tau) \rangle \right] \quad (5.36)$$

where $I_0(\vec{r})$ is given by Eq. (5.3) and $S^\pm = \sum_{i=1}^N S_i^\pm$. The two time correlation function can be calculated by using the quantum regression theorem. We can expand S^- as $S^- = \sum_{i,j} \alpha_{ij} X_{ij}$ where $X_{ij} = |i\rangle\langle j|$ and $|i\rangle(|j\rangle)$ is the basis of the bare atomic system. Then the two-time correlation function can be written as

$$\langle S^+(t) S^-(t + \tau) \rangle = \sum_{i,j} \alpha_{ij} C_{i,j}(t, \tau) \quad (5.37)$$

where $C_{i,j}(t, \tau) = \langle S^+(t) X_{i,j}(t + \tau) \rangle$.

Since $\langle X_{ij} \rangle = \rho_{ji}$, the one-time averages can be calculated from the master equations. Assuming that

$$\frac{d\langle X_{ij}(t) \rangle}{dt} = \sum_{kl} \mathcal{L}_{ijkl} \langle X_{kl}(t) \rangle, \quad (5.38)$$

we have from quantum regression theorem

$$\frac{\partial C_{ij}(t, \tau)}{\partial \tau} = \sum_{kl} \mathcal{L}_{ijkl} \langle C_{kl}(t, \tau) \rangle \quad (5.39)$$

where the coefficients \mathcal{L}_{ijkl} include the effects of the system Hamiltonian as well as the relaxation process. After calculating $C_{ij}(t, \tau)$, we can then calculate the resonance fluorescence from Eq. (5.36) and Eq. (5.37).

The numerical examples for three-atom example are shown in Fig. 5.6. In the first example, the separation between the atoms is about $\lambda/5$ which is not very small but still less than the diffraction limit. We apply a laser light with gradient field strength such that $\Omega(x) = 100\Gamma x/\lambda$. The resonance fluorescence is shown in Fig. 5.6(a) where we can see that three sidebands on each side of the center peak appear. From these three sidebands, we can read out the Rabi frequencies felt by the three atoms which are given by $\Omega_1 = 29.91 \pm 1.75(\Gamma)$, $\Omega_2 = 50.05 \pm 1.80(\Gamma)$, and $\Omega_3 = 69.80 \pm 1.73(\Gamma)$. Plugging these values into the expression of Rabi frequency, we can determine that the positions of the three atoms are $x_1 = 0.299 \pm 0.002(\lambda)$, $x_2 = 0.501 \pm 0.002(\lambda)$, and $x_3 = 0.698 \pm 0.002(\lambda)$ which match the real positions of the three atoms very well.

If the distance between the atoms are smaller, for example, $x_1 = 0.45\lambda$, $x_2 = 0.5\lambda$, and $x_3 = 0.6\lambda$ where the distance between the first two atoms is $\lambda/20$ which is much smaller than the diffraction limit. If we apply the same laser gradient as the first

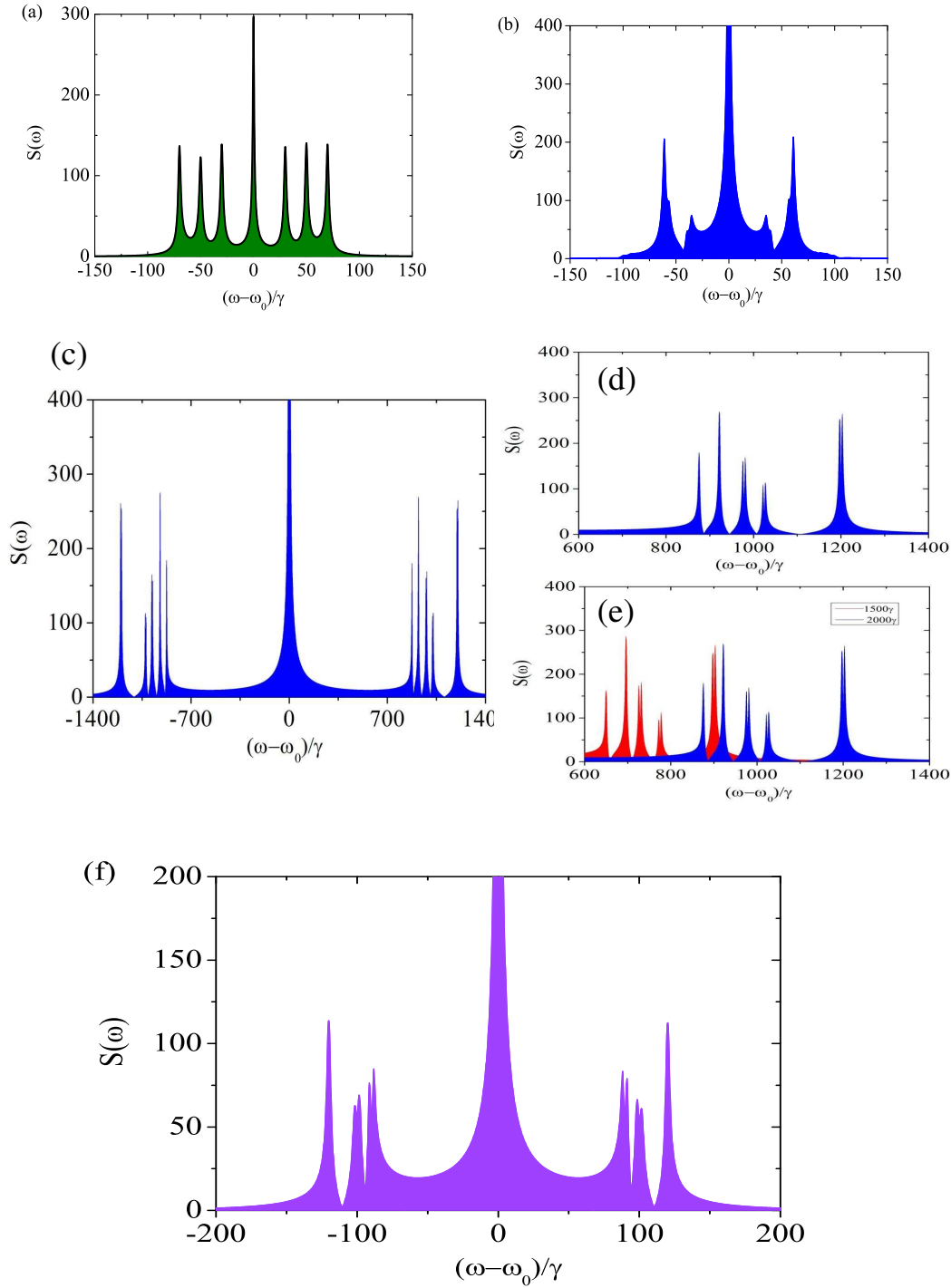


Figure 5.6: Numerical examples of three-atom resonance fluorescence spectrum. (a) $x_1 = 0.3\lambda, x_2 = 0.5\lambda, x_3 = 0.7\lambda, \Omega(x) = 100\Gamma x/\lambda$. (b) $x_1 = 0.45\lambda, x_2 = 0.5\lambda, x_3 = 0.6\lambda, \Omega(x) = 100\Gamma x/\lambda$. (c-d) Same as (b) but $\Omega(x) = 2000\Gamma x/\lambda$. (e) Spectrum shifts when Rabi frequency changes (Red: $\Omega(x) = 1500\Gamma x/\lambda$; Blue: $\Omega(x) = 2000\Gamma x/\lambda$). (f) The result when $\theta = \cos^{-1}(1/\sqrt{3})$ and $\Omega(x) = 200\Gamma x/\lambda$.

example, the resonance fluorescence spectrum is shown in Fig. 5.6(b). This spectrum is complicated where the peaks merger and shift. It is very difficult to extract the position information of the first and the second atoms. The reason is that the dipole-dipole interaction between the first two atoms is larger than the atomic transition linewidth. It significantly change the eigen-spectrum of the Hamiltonian and thus change the resonance fluorescence spectrum.

According to our previous theoretical prediction, the resonance fluorescence spectrum can become more regular if we increase the Rabi gradient. For example, we increase the Rabi gradient such that $\Omega(x) = 2000\Gamma x/\lambda$ and the resonance fluorescence spectrum is shown in Fig. 5.6(c,d). We can see that the spectrum appears to be more regular where the spectrum belongs to each atom splits. However, we do not know which peaks belong to which atom. One way to solve this problem is that we change the Rabi gradient by an amount such that $\Omega(x) = 1500\Gamma x/\lambda$ and the spectrum is shown as red curve in Fig. 5.6(e). From the figure we see that the spectrum shifts to the left. According to our analytical calculation, the spectrum belongs to each atom moves as a whole group while the separation between the spectrum belongs to different groups changes. Comparing the spectrum for two different Rabi frequency, we can determine that there are three groups of spectrum and the peaks for each group are given by (from blue curves): (1) 875.3Γ , 921.3Γ ; (2) 976.0Γ , 980.8Γ , 1022.0Γ , 1026.8Γ ; (3) 1197.5Γ , 1203.2Γ . The average Rabi frequency for each group reads: $\Omega_1 = 898.3\Gamma$, $\Omega_2 = 1001.4\Gamma$, and $\Omega_3 = 1200.3\Gamma$. From these Rabi frequencies, we can determine the positions of the atoms to be $x_1 = 0.449\lambda$, $x_2 = 0.501\lambda$, and $x_3 = 0.560\lambda$ which match the real positions very well.

It is also possible to reduce the power needed for RFM if we can control the direction of the transition dipole moment. Since the direction of the transition dipole moment depends on the polarization of the excitation beam, we can control the

dipole-dipole interaction energy according to Eq. (5.18). For example, if the direction of the transition dipole moment is tuned such that $\theta = \cos^{-1}(1/\sqrt{3})$, the $1/r^2$ and $1/r^3$ terms can be eliminated leaving only the long-range interaction term. The dipole-dipole interaction energy can be largely suppressed in the near field. In this way we can significantly reduce the power needed for our scheme. For the same atomic system used in Fig. rfm-example(c), the new spectrum is shown in Fig. rfm-example(f) where $\theta = \cos^{-1}(1/\sqrt{3})$ and $\Omega(x) = 200\Gamma x/\lambda$. We can see that there are three groups of spectrum: (1) $88.20\Gamma, 91.27\Gamma$; (2) $98.56\Gamma, 101.63\Gamma$; (3) 120.23Γ . Averaging over each group, we get $\Omega_1 = 89.7\Gamma$, $\Omega_2 = 100.1\Gamma$, and $\Omega_3 = 120.2\Gamma$, from which we can determine the positions of the atoms to be $x_1 = 0.449\lambda$, $x_2 = 0.501\lambda$, and $x_3 = 0.601\lambda$ which also match the real positions very well.

5.5 Extension to larger area and higher dimensions

In the previous section, we discuss how to resolve the atoms located within one wavelength. For a region larger than one wavelength, one simple way is to stretch the standing wave with larger periods to cover the whole region. This method is easy to operate but one disadvantage is that the field intensity increases as the working region increases. If the region is too large, the filed will be incredible large. Therefore, for a working region beyond several wavelengths extension, a new way may be needed. Here we propose a possible way trying to extend this limitation via divide-and-conquer method. The scheme is shown in Fig. 5.7(a). The sample is first shined by a standing wave denoted by a solid and red curve. The red-marked regions on the object plane locate in a approximately linear field region while the blue-marked regions do not. The resonance fluorescences are collected by a lens. The fluorescence emitted by the red-marked regions are focused to the red-marked detector pixels on the imaging plane, while the fluorescence emitted by the blue-marked regions are

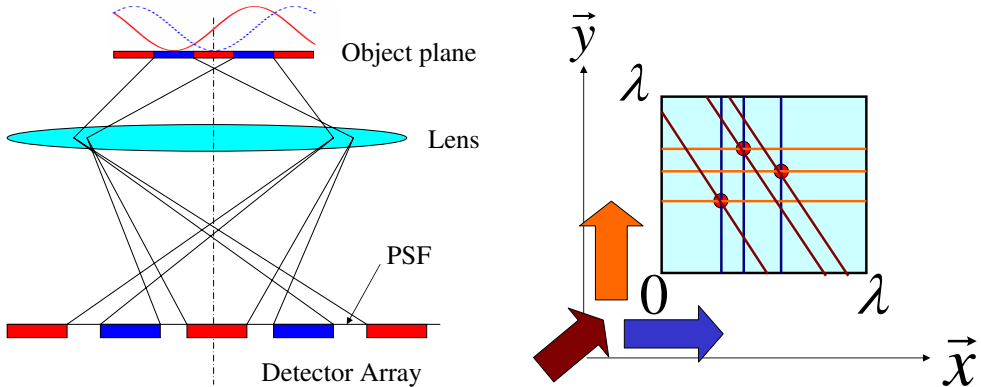


Figure 5.7: (a) Schematic setup for imaging atoms in an extended region based on our resonance fluorescence localization microscopy. (b) 2D resonance fluorescence localization microscopy.

focused to the blue-marked detector pixels. At this step only the spectrum of the fluorescence collected by the red-marked detector pixels are analyzed and we can determine the positions of the atoms in the red-marked regions on the object plane based on the method we illustrate in the previous sections. Then we shift our standing wave by a phase $\pi/2$. At this time the blue-marked regions locate in a approximately linear field while the red-marked regions do not. Applying similar process we can determine the positions of the atoms in the blue-marked regions. Because the image of a point in the object plane is not a point but a small disk which usually describes by point spread function of the lens, there is a gap between neighboring detector pixels to make sure that the fluorescence from the red-marked regions do not shine on the blue-marked detector pixels and vise versa. If we have an optical detecting array for each working on a region on the order of several wavelengths this method would be possible.

We can also apply our method to 2D image. The scheme is shown in Fig. 5.7(b).

Three steps are needed to obtain the two dimensional spatial information. In the first two steps, we shine a gradient laser field along $x(y)$ direction, from the resonance fluorescence spectrum we can obtain a discrete set of $x(y)$ position information of the atoms. After that, we still can not determine the positions of the atoms because all combinations of x values and y values are possible. We should shine a third gradient field from a direction which avoids any two pairs of (x, y) . From the third resonance fluorescence spectrum we can pin down the positions of the atoms.

6. SUMMARY AND OUTLOOK

Optical imaging and optical lithography have very important applications in many areas such as biological imaging, medical imaging, and semiconductor industry. The optical photon provides non-ionizing and safe radiation for biomedical applications. It has big advantages over the near-field contacted techniques such as STM or AFM. However, diffraction limit becomes a critical bottle neck for the super-resolution imaging and lithography when it comes to the nanometer regime. If we can somehow overcome the diffraction limit in the optical imaging and optical lithography, they can become major tools for the nano science and technology due to their unbeatable properties.

In this thesis work, I have proposed a novel method to overcome the diffraction limit in the optical lithography via coherent Rabi gradient. This method relies on the nonlinearity of the atom-field interaction but does not require multiphoton absorption and/or photon entanglement. The extension to higher order resolution is straightforward where we just need to increase the laser intensity or pulse duration. We also proposed two atom lithography schemes based on coherent Rabi gradient. The first scheme using the Rubidium Rydberg atom and the microwave. Rydberg atom has a long coherence time and large transition dipole moment which are good for our scheme. Our numerical simulations show that sub-micrometer resolution is possible even the wavelength of the microwave is of the order of centimeter. The second scheme uses the Chromium atom and the visible light. Our numerical simulations show that sub-10nm resolution is possible even if the optical Stern-Gerlach effect is included.

In addition to optical lithography, we also proposed a method to achieve super-

resolution in optical imaging. We calculated the resonance fluorescence spectrum of multiple atom system and showed that the spatial information of the atoms can be extracted from the spectrum even if the dipole-dipole interaction is present. The resolution can be about $1/50$ of the wavelength. This methods is entirely based on far-field technique and it does not require point-by-point scanning, which indicates that our method may be more time-efficient.

Although our methods have a lot of advantages over other methods, there are still a lot of space that need to be improved. For example, in the optical lithography the method we proposed to write an arbitrary 2D pattern has a relatively large background which is not perfect for the practical applications. In the future, we need to study how to write an arbitrary pattern which can eliminate the background. One possible way to do this is engineering the spatial distribution and frequency components of the pulse which can print the pattern in a few cycles. Second, although the atom lithography provide a good testbed for our scheme, it is not a very good candidate for the practical lithography due to its relatively low throughput. We need to look for a suitable medium for our original scheme. We may mix some kinds of nanoparticles, which have a relatively longer coherence time and larger transition dipole moment, inside the photoresist. Coherent Rabi oscillations can be induced inside the nanoparticles and then the internal energy of the nanoparticles can be transferred to the photoresist through Föster energy transfer (FRET) for example. Last but not the least, a suitable photoresist for this scheme need to be studied.

In the optical imaging part, there are several questions need to be studied in the future. First, if the distance between the atoms is too small (e. g., less than $\lambda/50$), the dipole-dipole interaction energy is very large. In this case our method does not work well. We need to study how to solve this problem in the future. Second, to observe the sidebands in the resonance fluorescence spectrum, Rabi frequency need

to be larger than the transition linewidth. If the transition linewidth is large, the power required should also be very large. How can we improve our method and decrease the power needed? Third, there are vibrational and rotational sidebands for molecules. Could we apply our method in the molecular system? And so on.

REFERENCES

- [1] E. Abbe. Beitrge zur theorie des mikroskops und der mikroskopischen. *Arch. Mikr. Anat.*, 9:413, 1873.
- [2] L. Rayleigh. Investigations in optics, with special reference to the spectroscope. *Philos. Mag.*, 8:261, 1879.
- [3] H. G. Rudenberg and P. G. Rudenberg. Origin and background of the invention of the electron microscope: Commentary and expanded notes on memoir of reinhold rdenberg. *Advances in Imaging and Electron Physics*, 160:207, 2010.
- [4] E. Spille and R. Feder. X-ray lithography. *Top. Appl. Phys.*, 22:35, 1977.
- [5] C. Vieu, F. Carcenac, A. Ppin, Y. Chen, M. Mejias, A. Lebib, L. Manin-Ferlazzo, L. Couraud, and H. Launois. Electron beam lithography: Resolution limits and applications. *Appl. Surf. Sci.*, 164:111, 2000.
- [6] A. Diaspro (ed). *Nanoscopy and Multidimensional Optical Fluorescence Microscopy*. CRC Press, Boca Raton, USA.
- [7] M. M. Alkaisi, R. J. Blaikie, and S. J. McNab. Nanolithography in the evanescent near field. *Adv. Matter*, 13:877, 2001.
- [8] E. Betzig and J. K. Trautman. Near-field optics: microscopy, spectroscopy, and surface modification beyond the diffraction limit. *Science*, 257:189, 1992.
- [9] G. Binnig and C. F. Quate. Atomic force microscope. *Phys. Rev. Lett.*, 56:930, 1986.
- [10] V. F. Dryakhlyshin, A. Y. Klimov, V. V. Rogov, and N. V. Vostokov. Near-field optical lithography method for fabrication of the nanodimensional objects. *Appl. Surf. Sci.*, 248:200, 2005.
- [11] T. Ono and M. Esashi. Subwavelength pattern transfer by near-field pho-

- tolithography. *Jpn. J. Appl. Phys.*, 37:6745, 1998.
- [12] W. Denk, J. H. Strickler, and W. W. Webb. Two-photon laser scanning fluorescence microscopy. *Science*, 248:73, 1990.
- [13] W. Denk and K. Svoboda. Photon upmanship: Why multiphoton imaging is more than a gimmick. *Science*, 248:73, 1990.
- [14] J. Wichmann S. W. Hell. Breaking the diffraction resolution limit by stimulated emission: stimulated-emission-depletion fluorescence microscopy. *Opt. Lett.*, 19:780, 1994.
- [15] F. Helmchen and W. Denk. Deep tissue two-photon microscopy. *Nature Methods*, 2:932, 2005.
- [16] J. H. Strickler and W. W. Webb. Two-photon excitation in laser scanning fluorescence microscopy. *Proceedings of the SPIE*, 1398:107, 1991.
- [17] S. W. Hell. Far-field optical nanoscopy. *Science*, 316:1153, 2007.
- [18] S. W. Hell and M. Kroug. Ground-state-depletion fluorescence microscopy: a concept for breaking the diffraction resolution limit. *Appl. Phys. B*, 60:495, 1995.
- [19] G. Donnert, J. Keller, R. Medda, M. Alexandra Andrei, S. O. Rizzoli, R. Lührmann, R. Jahn, C. Eggeling, and S. W. Hell. Macromolecular-scale resolution in biological fluorescence microscopy. *PNAS*, 103:11440, 2006.
- [20] T. A. Klar and S. W. Hell. Subdiffraction resolution in far-field fluorescence microscopy. *Opt. Lett.*, 24:954, 1999.
- [21] T. A. Klar, S. Jakobs, M. Dyba, A. Egner, and S. W. Hell. Fluorescence microscopy with diffraction resolution barrier broken by stimulated emission. *PNAS*, 97:8206, 2000.
- [22] E. Rittweger, K. Y. Han, S. E. Irvine, C. Eggeling, and S. W. Hell. Sted microscopy reveals crystal colour centres with nanometric resolution. *Nature*

Photonics, 3:144, 2009.

- [23] M. G. L. Gustafsson. Surpassing the lateral resolution limit by a factor of two using structured illumination microscopy. *Journal of Microscopy*, 198:82, 2000.
- [24] M. G. L. Gustafsson. Nonlinear structured-illumination microscopy: Wide-field fluorescence imaging with theoretically unlimited resolution. *PNAS*, 102:13081, 2005.
- [25] E. Betzig, G. H. Patterson, R. Sougrat, O. W. Lindwasser, S. Scott Olenych, J. S. Bonifacino, M. W. Davidson, J. Lippincott-Schwartz, and H. F. Hess. Imaging intracellular fluorescent proteins at nanometer resolution. *Science*, 313:1642, 2006.
- [26] X. Zhuang. Nano-imaging with storm. *Nature Photonics*, 3:365, 2009.
- [27] V. G. Veselago. The electrodynamics of substances with simultaneously negative values of ϵ and μ . *Sov. Phys. Uspekhi-USSR*, 10:509C514, 1968.
- [28] X. Zhang and Z. Liu. Superlenses to overcome the diffraction limit. *Nature Materials*, 7:435, 2008.
- [29] D. Lu and Z. Liu. Hyperlenses and metalenses for far-field super-resolution imaging. *Nat. Commun.*, 3:1205, 2012.
- [30] G. S. Agarwal, R. W. Boyd, E. M. Nagasako, and S. J. Bentley. Comment on “quantum interferometric optical lithography: Exploiting entanglement to beat the diffraction limit”. *Phys. Rev. Lett.*, 86:1389, 2001.
- [31] A. V. Gorshkov, L. Jiang, M. Greiner, P. Zoller, and M. D. Lukin. Coherent quantum optical control with subwavelength resolution. *Phys. Rev. Lett.*, 100:093005, 2008.
- [32] M. Kiffner, J. Evers, and M. S. Zubairy. Resonant interferometric lithography beyond the diffraction limit. *Phys. Rev. Lett.*, 100:073602, 2008.
- [33] D. D. Yavuz and N. A. Proite. Nanoscale resolution fluorescence microscopy

- using electromagnetically induced transparency. *Phys. Rev. A*, 76:041802, 2007.
- [34] S. Qamarand S.-Y. Zhu and M. S. Zubairy. Atom localization via resonance fluorescence. *Phys. Rev. A*, 61:063806, 2000.
- [35] J. Chang, J. Evers, M. O. Scully, and M. S. Zubairy. Measurement of the separation between atoms beyond diffraction limit. *Phys. Rev. A*, 73:031803(R), 2006.
- [36] M. Macovei, J. Evers, C. H. Keitel, and M. S. Zubairy. Localization of atomic ensembles via superfluorescenc. *Phys. Rev. A*, 75:033801, 2007.
- [37] J. Mompart, V. Ahufinger, and G. Birkl. Coherent patterning of matter waves with subwavelength localization. *Phys. Rev. A*, 79:053638, 2009.
- [38] Q. Sun, M. Al-Amri, M. O. Scully, and M. S. Zubairy. Subwavelength optical microscopy in the far field. *Phys. Rev. A*, 83:063818, 2011.
- [39] Z. Liao, M. Al-Amri, and M. S. Zubairy. Resonance fluorescence localization microscopy with subwavelength resolution. *Phys. Rev. A*, 85:023810, 2012.
- [40] A. K-K. Wong. *Resolution Enhancement Techniques in Optical lithography*. SPIE Press, Washington, USA.
- [41] J. L. Harry. *Principles of Lithography*. SPIE Press, Washington, USA.
- [42] C. Lu and R. H. Lipson. Interference lithography: A powerful tool for fabricating periodic structures. *Laser & Photonics Reviews*, 4:568, 2010.
- [43] C. Mack. *Fundamental Optical Principles of Lithography: The Science of Microfabrication*. John Wiley & Sons Ltd., West Sussex, England.
- [44] R. P. Seisyan. Nanolithography in microelectronics: A review. *tech phys. Tech. Phys.*, 56:1061, 2011.
- [45] S. R. J. Brueck, S. H. Zaidi, X. Chen, and Z. Zhang. Interferometric lithography from periodic arrays to arbitrary patterns. *Microelectron. Eng.*, 41/42:145, 1998.

- [46] M. Rothschild. A roadmap for optical lithography. *OPN*, 21:27, 2010.
- [47] G. L.-T. Chiu and J. M. Shaw. Optical lithography: Introduction. *IBM J. Res. Develop.*, 41:3, 1997.
- [48] M. C. Marconi and P. W. Wachulak. Extreme ultraviolet lithography with table top lasers. *Prog Quant Electron*, 34:173, 2010.
- [49] J. S. Taylor, G. E. Sommargren, D. W. Sweeney, and R. M. Hudyma. Fabrication and testing of optics for euv projection lithography. *Proceedings of the SPIE*, 333:580, 1998.
- [50] M. G. Ivan and J. C. Scaiano. *Photoimaging and lithographic processes in polymers*. John Wiley & Sons, New Jersey, USA.
- [51] S. K. Lee and H-W Lee. The role of entanglement in quantum lithography. *J. Phys. Soc. Jpn*, 77:124001, 2008.
- [52] C. Williams, P. Kok, H. Lee, and J. P. Dowling. Quantum lithography: A non-computing application of quantum information. *Informatik Forsch. Entw.*, 21:73, 2006.
- [53] E. S. Wu, J. H. Strickler, W. R. Harrell, and W. W. Webb. Optical/laser microlithography v. *Proceedings of the SPIE*, 1674:776, 1992.
- [54] E. Yablonovitch and R. B. Vrijen. Optical projection lithography at half the rayleigh resolution limit by two-photon exposure. *Opt. Eng.*, 38:334, 1999.
- [55] A. Boto, P. Kok, D. Abrams, S. Braunstein, C. P. Williams, and J. P. Dowling. Quantum interferometric optical lithography: Exploiting entanglement to beat the diffraction limit. *Phys. Rev. Lett.*, 85:2733, 2000.
- [56] S. J. Bentley and R. W. Boyd. Nonlinear optical lithography with ultra-high sub-rayleigh resolution. *Opt. Express*, 12:5735, 2004.
- [57] P. R. Hemmer, A. Muthukrishnan, M. O. Scully, and M. S. Zubairy. Quantum lithography with classical light. *Phys. Rev. Lett.*, 96:163603, 2006.

- [58] A. Peér, B. Dayan, M. Vucelja, Y. Silberberg, and A. A. Friesem. Quantum lithography by coherent control of classical light pulses. *Optics Express*, 12:6600, 2004.
- [59] Z. Liao, M. Al-amri, and M. S. Zubairy. Quantum lithography beyond the diffraction limit via rabi oscillations. *Phys. Rev. Lett.*, 105:183601, 2010.
- [60] M. Al-Amri, Z. Liao, and M. S. Zubairy. Beyond the diffraction limit in optical lithograph. *Advances in Atomic, Molecular, and Optical Physics*, 61:409–466, 2012.
- [61] Z. Liao, M. Al-Amri, T. Becker, W. P. Schleich, M. O. Scully, and M. S. Zubairy. Atomic lithography with subwavelength resolution via rabi oscillations. *Phys. Rev. A*, 87:023405, 2013.
- [62] Z. Liao, M. Al-Amri, and M. S. Zubairy. Coherent atom lithography with nanometer spacing. *Phys. Rev. A*, 88:053809, 2013.
- [63] Wikipedia. Microscope — wikipedia, the free encyclopedia, 2014. [Online; accessed 9-April-2014].
- [64] B. Huang, M. Bates, and X. Zhuang. Super resolution fluorescence microscopy. *Annu. Rev. Biochem.*, 78:993–1016, 2009.
- [65] *Optical and Interferometric Lithography - Nanotechnology Enablers*, volume 93, 2005.
- [66] J. R. Sheats and B. W. Smith (Eds). *Microlithography Science and Technology*. Marcel Dekker Inc, New York, 1998.
- [67] P. R. Hemmer and T. Zapata. The universal scaling laws that determine the achievable resolution in diffraction schemes for super-resolution imaging. *J. Opt.*, 14:083002, 2012.
- [68] M. M. Alkaisi, R. J. Blaikie, S. J. McNab, R. Cheung, and D. R. S. Cumming. Sub-diffraction-limited patterning using evanescent near-field optical lithogra-

- phy. *Appl. Phys. Lett.*, 75:3560, 1999.
- [69] A. Neice. Methods and limitations of subwavelength imaging. *Advances in Imaging and Electron Physics*, 163:117, 2010.
- [70] J. B. Pendry. Negative refraction makes a perfect lens. *Phys. Rev. Lett.*, 85:3966, 2000.
- [71] P. J. Shaw and D. J. Rawlins. The point-spread function of a confocal microscope: its measurement and use in deconvolution of 3-d data. *Journal of Microscopy*, 163:151–165, 1991.
- [72] M. Goeppert-Mayer. Ueber elementarakte mit zwei quantenspruengen. *Ann. Phys.*, 9:273, 1931.
- [73] I. D. Abella. Optical double-photon absorption in cesium vapor. *Phys. Rev. Lett.*, 9:453, 1962.
- [74] J. H. Strickler and W. W. Webb. Three-dimensional optical data storage in refractive media by two-photon point excitation. *Optics Lett.*, 16:1780, 1991.
- [75] W. M. McClain. Two-photon molecular spectroscopy. *Acc. Chem Res.*, 7:129, 1974.
- [76] J. B. Pendry. Perfect cylindrical lenses. *Optics express*, 11:755, 2003.
- [77] Z. Liu, H. Lee, Y. Xiong, C. Sun, and X. Zhang. Far-field optical hyperlens magnifying sub-diffraction-limited objects. *Science*, 315:1686, 2007.
- [78] S. Kawata, H.-B. Sun, T. Tanaka, and K. Takada. Finer features for functional microdevices. *Nature*, 412:697, 2001.
- [79] M. Tsang. Relationship between resolution enhancement and multiphoton absorption rate in quantum lithography. *Phys. Rev. A*, 75:043813, 2007.
- [80] B. R. Mollow. Two-photon absorption and field correlation functions. *Phys. Rev.*, 175:1555, 1968.
- [81] E. Arimondo. Coherent population trapping in laser spectroscopy. *Prog. Opt.*,

35:259, 1996.

- [82] M. O. Scully and M. S. Zubairy. *Quantum Optics*. Cambridge University Press, Cambrige, England.
- [83] M. S. Zubairy, A. B. Matsko, and M. O. Scully. Resonant enhancement of high-order optical nonlinearities based on atomic coherence. *Phys. Rev. A*, 65:043804, 2002.
- [84] C. E. Wayne and R. P. Wayne. *Photochemistry*. Oxford University Press, New York, USA.
- [85] N. J. Turro, V. Ramamurthy, and J. C. Scaiano. *Principles of Molecular Photochemistry: An Introduction*. University Science Books, Sausalito, CA.
- [86] P. Kok, A. N. Boto, D. S. Abrams, C. P. Williams, S. L. Braunstein, and J. P. Dowling. Quantum-interferometric optical lithography: Towards arbitrary two-dimensional patterns. *Phys. Rev. A*, 63:063407, 2001.
- [87] S. Pau, G. P. Watson, and O. Nalamasu. Writing an arbitrary pattern using interference lithography. *J. Mod. Opt.*, 48:1211, 2001.
- [88] Q. Sun, P. R. Hemmer, and M. S. Zubairy. Quantum lithography with classical light: Generation of arbitrary patterns. *Phys. Rev. A*, 75:065803, 2007.
- [89] S. F. Fischer and A. Laubereau. Dephasing processes of molecular vibrations in liquids. *Chem. Phys. Lett.*, 35:6, 1975.
- [90] G. Balasubramanian, P. Neumann, D. Twitchen, M. Markham, R. Kolesov, N. Mizuochi, J. Isoya, J. Achard, J. Beck, J. Tissler, V. Jacques, P. R. Hemmer, F. Jelezko, and J. Wrachtrup. Ultralong spin coherence time in isotopically engineered diamond. *Nature Material*, 8:383, 2009.
- [91] K. A. Suominen, B. M. Garraway, and S. Stenholm. Wave-packet model for excitation by ultrashort pulses. *Phys. Rev. A*, 45:3060, 1992.
- [92] B. M. Garraway and K-A. Suominen. Wave-packet dynamics: new physics and

- chemistry in femto-time. *Rep. Prog. Phys.*, 58:365, 1995.
- [93] R. Kosloff. Time-dependent quantum-mechanical methods for molecular dynamics. *J. Phys. Chem.*, 92:2087, 1988.
- [94] A. Paloviita and K. A. Suominen. Molecular excitation by large-area ultrashort pulses. *Phys. Rev. A*, 55:3007, 1997.
- [95] Z. Liao, M. Al-amri, and M. S. Zubairy. Subdiffraction-limit pattern generation in molecular system via coherent rabi oscillations. *In preparation*.
- [96] R. Szipőcs and A. Kőházi-kis. Theory and design of chirped dielectric laser mirrors. *Appl. Phys. B*, 65:115, 1997.
- [97] G. Timp, R. E. Behringer, D. M. Tennant, J. E. Cunningham, M. Prentiss, and K. K. Berggren. Using light as a lens for submicron, neutral-atom lithography. *Phys. Rev. Lett.*, 69:1636, 2001.
- [98] J. J. McClelland, R. E. Scholten, E. C. Palm, and R. J. Celotta. Laser-focused atomic deposition. *Science*, 262:877, 1993.
- [99] K. S. Johnson, J. H. Thywissen, N. H. Dekker, K. K. Berggren, A. P. Chu, R. Younkin, and M. Prentiss. Localization of metastable atom beams with optical standing waves: Nanolithography at the heisenberg limit. *Science*, 280:1583, 1998.
- [100] V. Natarajan, R. E. Behringer, D. M. Tennant, and G. Timp. Focusing and defocusing of neutral atomic beams using resonance radiation pressure. *J. Vac. Sci. Technol. B*, 13:2823, 1995.
- [101] M. Mütsel, S. Tandler, D. Haubrich, D. Meschede, K. Peithmann, M. Flaspöhler, and K. Buse. Atom lithography with a holographic light mask. *Phys. Rev. Lett.*, 88:083601, 2002.
- [102] E. te Sligte, B. Smeets, R.C.M. Bosch, K.M.R. van der Stam, L.P. Maguire, R.E. Scholten, H.C.W. Beijerinck, and K.A.H. van Leeuwen. Progress towards

- atom lithography on iron. *Micr. Eng.*, 67-68:664, 2003.
- [103] C. S. Allred, J. Reeves, C. Corder, and H. Metcalf. Atom lithography with metastable helium. *J. Appl. Phys.*, 107:033116, 2010.
- [104] G. Rempe, H. Walther, and N. Klein. Observation of quantum collapse and revival in a one-atom maser. *Phys. Rev. Lett.*, 58:353, 1987.
- [105] G. Rempe, F. Schmidt-Kaler, and H. Walther. Observation of sub-poissonian photon statistics in a micromaser. *Phys. Rev. Lett.*, 64:2783, 1990.
- [106] M. Brune, F. Schmidt-Kaler, A. Maali, J. Dreyer, E. Hagley, J. M. Raimond, and S. Haroche. Quantum rabi oscillation: A direct test of field quantization in a cavity. *Phys. Rev. Lett.*, 76:1800, 1996.
- [107] G. M. Lankhuijzen and L. D. Noordam. Rydberg ionization: From field to photon. *Adv. At., Mol., Opt. Phys.*, 38:121, 1998.
- [108] P. Thoumany, T. W. Hänsch, G. Stania, L. Urbonas, and Th. Becker. Optical spectroscopy of rubidium rydberg atoms with a 297nm frequency-doubled dye laser. *Opt. Lett.*, 34:1621, 2009.
- [109] B. Sheehy, S.-Q. Shang, P. van der Straten, and H. Metcalf. Collimation of a rubidium beam below the doppler limit. *Chem. Phys.*, 145:317, 1990.
- [110] J. Dalibard and C. Cohen-Tannoudji. Laser cooling below the doppler limit by polarization gradients: simple theoretical models. *J. Opt. Soc. Am. B*, 6:2023, 1989.
- [111] R. E. Scholten, R. Gupta, J. J. McClelland, R. J. Celotta, M. S. Levenson, and M. G. Vangel. Laser collimation of a chromium beam. *Phys. Rev. A*, 55:1331, 1997.
- [112] D. F. Walls and G. J. Milburn. *Quantum Optics*. Springer, Berlin, Germany.
- [113] J. E. Schumacher, M. Wilkens, P. Meystre, and S. Glasgow. Spontaneous emission in the near-resonant kapitza-dirac effect. *Appl. Phys. B*, 54:451, 1992.

- [114] R. J. Cook. Optical stern-gerlach effect. *Phys. Rev. A*, 35:3844, 1987.
- [115] T. Sleator, T. Pfau, V. Balykin, O. Carnal, and J. Mlynek. Experimental demonstration of the optical stern-gerlach effect. *Phys. Rev. Lett.*, 68:1996, 1992.
- [116] C. J. Lee. Quantum-mechanical analysis of atom lithography. *Phys. Rev. A*, 61:063604, 2000.
- [117] T. G. Rudolph, Z. Ficek, and B. J. Dalton. Two-atom resonance fluorescence in running- and standing-wave laser fields. *Phys. Rev. A*, 52:636, 1995.
- [118] Z. Ficek and S. Swain. *Quantum Interference and Quantum Coherence: Theory and Experiment*. Springer, New York, USA.
- [119] C. Cohen-Tannoudji and S. Reynaud. Dressed-atom description of resonance fluorescence and absorption spectra of a multi-level atom in an intense laser beam. *J. Phys. B: Atom. Molec. Phys.*, 10:345, 1977.
- [120] H. S. Freedhoff. Collective atomic effects in resonance fluorescence: Dipole-dipole interaction. *Phys. Rev. A*, 19:1132, 1979.
- [121] R. H. Dicke. Coherence in spontaneous radiation processes. *Phys. Rev.*, 93:99, 1954.
- [122] Y. V. Rostovtsev, H. Eleuch, A. Svidzinsky, H. Li, V. Sautenkov, and M. O. Scully. Excitation of atomic coherence using off-resonant strong laser pulses. *Phys. Rev. A*, 79:063833, 2009.

APPENDIX A

PULSE AREA THEOREM

In the rotating wave approximation, the Hamiltonian of the light-interacting two-level system is given by [122]

$$H = \hbar \begin{bmatrix} 0 & \Omega_R(t)e^{i\Delta t} \\ \Omega_R(t)e^{-i\Delta t} & 0 \end{bmatrix}. \quad (\text{A.1})$$

The dynamics equations for the amplitudes are

$$i\dot{C}_a(t) = \Omega t e^{i\Delta t} C_b(t), \quad (\text{A.2})$$

$$i\dot{C}_b(t) = \Omega t e^{-i\Delta t} C_a(t). \quad (\text{A.3})$$

Let $f(t) = C_a(t)/C_b(t)$, we have

$$\dot{f}(t) = i\Omega(t)e^{-i\Delta t} f^2 - i\Omega(t)e^{i\Delta t}. \quad (\text{A.4})$$

In general cases, no analytical solution has been found yet. However, for resonant excitation such that $\Delta = 0$, there is analytical solution. Assuming $C_b(t) = 1$, the solution is

$$f(t) = -i \tan \theta(t) \quad (\text{A.5})$$

where $\theta(t)$ is the pulse area which is given by

$$\theta(t) = \int_{-\infty}^t \Omega(t') dt'. \quad (\text{A.6})$$

From normalization condition $|C_a|^2 + |C_b|^2 = 1$ and Eq. (A.5), we have $|C_a|^2 = \frac{|f|^2}{1+|f|^2}$. Thus, the excitation probability is given by

$$|C_a(t)|^2 = \frac{1}{2}[1 - \cos \theta(t)]. \quad (\text{A.7})$$

APPENDIX B

QUANTUM REGRESSION THEOREM

The quantum regression theorem says that if the single time correlation function is governed by

$$\langle \hat{O}(t + \tau) \rangle = \sum_j a_j \langle \hat{O}_j(t) \rangle, \quad (\text{B.1})$$

then we have two-time correlation function given by

$$\langle \hat{O}_i(t) \hat{O}(t + \tau) \hat{O}_k(t) \rangle = \sum_j a_j \langle \hat{O}_i(t) \hat{O}_j(t) \hat{O}_k(t) \rangle. \quad (\text{B.2})$$

Assume that the interaction between the system and the reservoir is “switched” on at time t , the initial state of the whole system can be written as

$$\rho_{SR}(t) = \rho_S(t) \otimes \rho_R(t). \quad (\text{B.3})$$

Let $U(\tau)$ be a unitary evolution of the system and reservoir, we have

$$\begin{aligned} \langle \hat{O}(t + \tau) \rangle &= Tr_{SR}[O(t + \tau)\rho_{SR}(t)] \\ &= Tr_{SR}[U^+(\tau)O(t)U(\tau)\rho_{SR}(t)] \\ &= Tr_{SR}[O(t)U(\tau)\rho_{SR}(t)U^+(\tau)] \\ &= Tr_{SR}[O(t)U(\tau)\rho_S(t) \otimes \rho_R(t)U^+(\tau)]. \end{aligned} \quad (\text{B.4})$$

and

$$\begin{aligned}
\langle \hat{O}_i(t) \hat{O}(t + \tau) \hat{O}_k(t) \rangle &= Tr_{SR}[\hat{O}_i(t) O(t + \tau) \hat{O}_k(t) \rho_{SR}(t)] \\
&= Tr_{SR}[\hat{O}_i(t) U^+(\tau) O(t) U(\tau) \hat{O}_k(t) \rho_{SR}(t)] \\
&= Tr_{SR}[O(t) U(\tau) \hat{O}_k(t) \rho_S(t) \otimes \rho_R(t) \hat{O}_i(t) U^+(\tau)] \\
&= Tr_{SR}[O(t) U(\tau) \hat{O}_k(t) \rho_S(t) \hat{O}_i(t) \otimes \rho_R(t) U^+(\tau)]. \quad (\text{B.5})
\end{aligned}$$

Comparing Eq. (B.4) with (B.5), we see that the difference between the two-time average and the one-time average is that $\rho_S(t)$ is replaced by $O_k(t) \rho_S(t) \hat{O}_i(t)$.

If we have

$$\langle \hat{O}(t + \tau) \rangle = \sum_j a_j \langle \hat{O}_j(t) \rangle = \sum_j a_j Tr_{SR}[\hat{O}_j(t) \rho_S(t) \otimes \rho_R(t)], \quad (\text{B.6})$$

then we have

$$\begin{aligned}
\langle \hat{O}_i(t) \hat{O}(t + \tau) \hat{O}_k(t) \rangle &= \sum_j a_j Tr_{SR}[\hat{O}_j(t) O_k(t) \rho_S(t) \hat{O}_i(t) \otimes \rho_R(t)] \\
&= \sum_j a_j Tr_{SR}[\hat{O}_i(t) \hat{O}_j(t) O_k(t) \rho_S(t) \otimes \rho_R(t)] \\
&= \sum_j a_j \langle \hat{O}_i(t) \hat{O}_j(t) O_k(t) \rangle \quad (\text{B.7})
\end{aligned}$$

which is the quantum regression theorem.